

NASA Contractor Report 4023

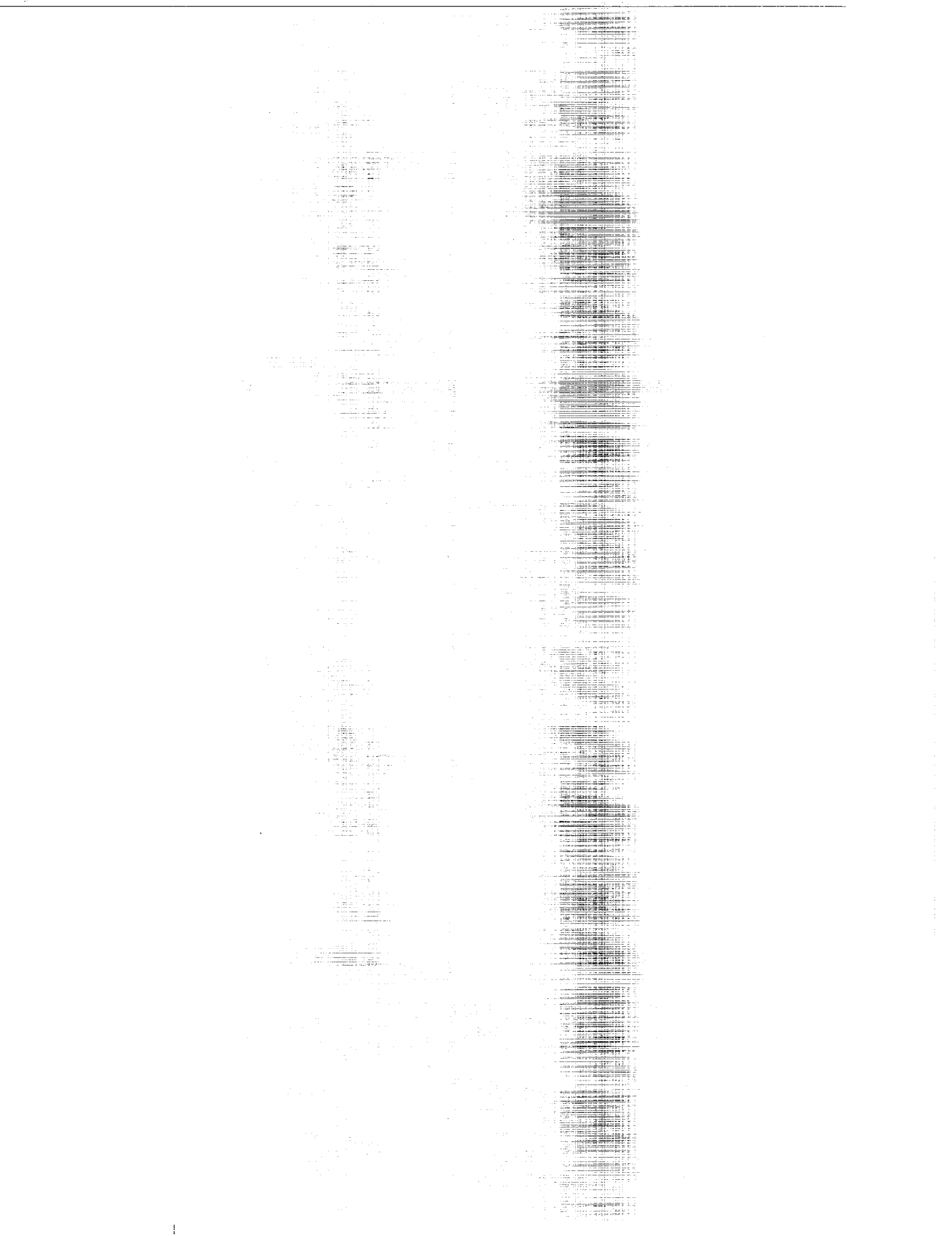
Program VSAERO Theory Document

*A Computer Program for Calculating
Nonlinear Aerodynamic Characteristics
of Arbitrary Configurations*

Brian Maskew

CONTRACT NAS2-11945
SEPTEMBER 1987

NASA



NASA Contractor Report 4023

Program VSAERO Theory Document

*A Computer Program for Calculating
Nonlinear Aerodynamic Characteristics
of Arbitrary Configurations*

Brian Maskew
Analytical Methods, Inc.
Redmond, Washington

Prepared for
Ames Research Center
under Contract NAS2-11945



National Aeronautics
and Space Administration

**Scientific and Technical
Information Office**

1987

TABLE OF CONTENTS

<u>Section</u>	<u>Page No.</u>
LIST OF FIGURES	iii
LIST OF SYMBOLS	vi
1.0 INTRODUCTION	
1.1 General	1
1.2 Objectives	1
1.3 Strategy	1
2.0 FORMULATION	
2.1 Flow Equation	3
2.2 Boundary Conditions	6
2.3 Choice of Singularity Model	8
3.0 NUMERICAL PROCEDURE	16
3.1 Geometrical Description	16
3.1.1 Patch	16
3.1.2 Panel Geometry	21
3.1.3 Panel Neighbors	25
3.1.4 Wakes	26
3.2 Matrix of Influence Coefficients	31
3.2.1 Velocity Potential Influence Coefficient	
3.2.1.1 Doublet Contribution	33
3.2.1.2 Source Contribution	40
3.2.2 Velocity Vector Influence Coefficients	
3.2.2.1 Doublet Contribution	41
3.2.2.2 Source Contribution	44
3.2.3 Matrix Assembly	46
3.3 Matrix Solver	48
3.4 On-Body Analysis	48
3.5 Wake-Shape Calculation	57
3.6 Boundary Layer Analysis	58
3.7 Off-Body Analysis	59
3.7.1 Velocity Survey	59
3.7.2 Off-Body Streamline Procedure	60

TABLE OF CONTENTS (CONCLUDED)

<u>Section</u>	<u>Page No.</u>
4.0 DISCUSSION OF RESULTS	62
4.1 Swept Wing	62
4.2 Wing with Strake	62
4.3 Nacelles	64
4.4 Wing-Flap Cases	68
4.5 Body Alone	74
4.6 Wing-Body Cases	74
5.0 CONCLUSIONS	84
6.0 REFERENCES	85
APPENDICES:	
A: SUBROUTINE FLOW CHART	88
B: BIQUADRATIC INTERPOLATION	96

LIST OF FIGURES

<u>Fig. No.</u>	<u>Title</u>	<u>Page No.</u>
1	Section through the Idealized Flow Model . . .	4
2	Three of the Possible Internal Flows	9
3	Outline of the Steps in the VSAERO Program .	17
4	General Arrangement of the Configuration . .	18
5	Configuration Hierarchy	19
6	Patch Conventions	20
7	Sections Defining Patch Surface	22
8	Panel Geometry	23
9	Panel Neighbor Information	27
10	Panel Neighbors across Patch Edges	28
11	Wake-Grid-Plane Scheme	29
12	Wake Arrangement	30
13	Model used in the Evaluation of the Surface Integrals	35
14	Evaluation of the Surface Integrals for One Side of a Panel	36
15	Treatment of Symmetry and Ground-Plane Problems	39
16	Evaluation of the Line Integral	43
17	Evaluation of Perturbation Velocity on Panel K (All Neighbors Available and on Same Patch as Panel K)	49
18	Evaluation of Perturbation Velocity on Panel K when a Neighbor is not Available	52
19	Force Contribution from Panel K	53
20	Global and Wind Axis Systems	55
21	Streamline Calculation	61

LIST OF FIGURES (CONTINUED)

<u>Fig. No.</u>	<u>Title</u>	<u>Page No.</u>
22	Comparison of Calculated Chordwise Pressure Distribution on a Thin Swept Wing	63
23	Comparison of Calculated y -Component of Velocity at Two Stations on a Wing with Strake; NACA 0002 Section	65
24	Comparison of Internal Pressure Calculated using a Range of Methods Showing Leakage of Low-Order First Generation Model	66
25	Comparison of Calculated Pressure Distributions on a Nacelle with Exit Diameter/Chord.3; NACA 0005 Section	67
26	Comparison of VSAERO Calculation with Exact Solution for Williams (26) Two-Element Case B	
	(a) Main Element	69
	(b) Flap	70
	(c) Paneling	71
27	Comparison of Pressure Distributions on an Aspect Ratio 6 Wing with Part-Span Fowler Flap $\alpha = 16^\circ$	
	(a) Section at $\eta = .33$	72
	(b) Section at $\eta = .6$	73
28	Comparison of Calculated and Exact Pressure Distributions on a 4:1 Spheroid at $\alpha = 5^\circ$. .	75
29	Pressure Distributions on a Wing-Body Configuration at $\alpha = 4^\circ$, $M_\infty = .6^\circ$	
	(a) Above Wing-Body Junction Pressures	76
	(b) Spanwise Cut through Present Calculations . .	77
30	Swearingen Metroliner Wind Tunnel Model . . .	78
31	Comparison of Calculated and Experimental Pressure Distributions on the Swearingen Metroliner Wind Tunnel Model at $\alpha = 0.0$, $M_\infty = 2.0$	
	(a) Buttline Cut, $Y = 9.0$	79
	(b) Buttline Cut, $Y = 18.0$	79

LIST OF FIGURES (CONCLUDED)

<u>Fig. No.</u>	<u>Title</u>	<u>Page No.</u>
32	Comparison of Calculated and Experimental Pressure Distributions on the Swearingen Metroliner Wind Tunnel Model at $\alpha = 12^\circ$, $M_\infty = 2.0$	
(a)	Buttline Cut, $Y = 9.0$	80
(b)	Buttline Cut, $Y = 18.0$	80
33	Comparison of Calculated and Experimental Pressure Distributions on the Swearingen Metroliner Wind Tunnel Model at $\alpha = 16^\circ$, $M_\infty = 2.0$	
(a)	Buttline Cut, $Y = 9.0$	81
(b)	Buttline Cut, $Y = 18.0$	81
34	Calculated Streamlines and Separation Zone on the Swearingen Metroliner Wind Tunnel Model at $\alpha = 16^\circ$	83
 APPENDIX A		
A-1	Flow Chart of Main Program (Deck MVP); the Viscous/Potential Iteration Loop	89
A-2	Flow Chart of Subroutine VSAERO in Potential Flow	90
A-3	Flow chart for Major Subroutines in the Boundary Layer Analysis (Subroutine BLCTRL)	95
 APPENDIX B		
B-1	Biquadratic Interpolation	100

LIST OF SYMBOLS

AREA	Panel area
B_{JK}, C_{JK}	Perturbation velocity potential influence coefficient at the control point of panel J for a uniform distribution of unit source and unit doublet, respectively, on panel K
D	Diagonal vector in a panel
D_{JK}, E_{JK}	Influence coefficient for the normal component of velocity induced at the control point of panel J by a uniform distribution of unit source or doublet, respectively, on panel k
E	Position vector of a panel corner in the panel local coordinate system with origin at panel center
i, j, k	Orthogonal unit vector system along the x,y,z axes, respectively, of the global coordinate system
K	Factor for the local contribution to ϕ (Eq. (13))
$\left. \begin{array}{l} KWPU, \\ KWPL \end{array} \right\}$	Program subscripts of upper and lower surface panels shedding a wake column (Figure 11)
l, m, n	Orthogonal unit vector system in a local region; n is normal to the surface and l, m tangential
N	Number of panels
$NABOR_i$	Program subscript of neighboring panel on side i
$NABSID_i$	Program subscript of adjacent side of the neighboring panel in side i (Figure 9)
R	Position vector of a panel corner point in the G.C.S.
r	Position vector of a point relative to an element, ds, of the surface
r	Modulus of r
S	Surface (solid) of the configuration
s	Distance along the surface
SMP, SMQ	Panel half-median lengths (Figure 8)
V	Velocity vector

LIST OF SYMBOLS (CONTINUED)

V	Modulus of \mathbf{V}
\mathbf{v}	Perturbation velocity
W	Wake surface
x, y, z	Cartesian coordinates in the Global Coordinate System (G.C.S.)--body-fixed frame of reference
α	Incidence of G.C.S. x-axis degrees
γ	Vorticity vector density
δ^*	Boundary layer displacement thickness
ξ, η	Local coordinates in the ℓ and m directions, respectively, of the panel local coordinate system
μ	Doublet singularity density
Φ	Total velocity potential
ϕ	Velocity potential contribution, or perturbation component
ρ	Density
σ	Source singularity density
∇	Laplacian operator, $\mathbf{i} \frac{\partial}{\partial x} + \mathbf{j} \frac{\partial}{\partial y} + \mathbf{k} \frac{\partial}{\partial z}$
\cdot	Dot product of vectors
\times	Cross product of vectors

LIST OF SYMBOLS (CONCLUDED)

Subscripts

c	Center
e	Edge of the boundary layer
i	Inner region
J,K	Pertaining to panel J,K
L	Lower surface
N	Normal component
P	Pertaining to the point, P; also used as a subscript
S	Pertaining to the surface
U	Upper surface
W	Pertaining to the wake outer edge of the boundary layer
∞	Reference onset condition

1.0 INTRODUCTION

1.1 General

VSAERO is a computer program for calculating the subsonic **AERO**dynamic characteristics of arbitrary configurations having **Vortex Separation** and strong **Vortex/Surface** interaction. This document describes the theory and numerical procedures used for the method. An earlier report (1) describes the input and use of the computer program.

1.2 Objectives

The initial objectives of the new program were to analyze general wing configurations with multiple part-span, high-lift devices and to give special attention to edge-vortex separations and to close vortex/surface interactions. Later objectives brought in the modeling of fuselage and canard surfaces leading to the present capability for arbitrary configurations including complete aircraft.

1.3 Strategy

At the beginning of the program development there was only one clear cut choice for approaching the solution to the above nonlinear problem. This was an iterative viscous/potential flow calculation using a potential flow panel method coupled with integral boundary layer methods, with wake-shape iteration calculations included in the potential flow analysis. No other approach appeared to offer the feasibility of achieving the above objectives. Finite difference field methods, for example, treating more general flow equations, could not be developed within a reasonable time scale for application to the complex geometry of multiple part-span, high-lift devices. In the meantime, the surface integral approach of the panel method offered a powerful and practical engineering tool which had the capability to represent the complex geometries involved in the objectives. Furthermore, the low computing time of the panel method was an attractive feature in view of the complex iterative loops made necessary by the nonlinear effects of viscosity and wake location.

In the chosen strategy for the development of the VSAERO program the capabilities of two earlier programs were combined: (i) VIP3D (2) offered a viscous/potential flow iterative method for transport wings with full-span, high-lift devices; and (ii) QVORT, a quadrilateral-vortex panel method (3) and (4), offered an iterative wake relaxation procedure. Neither method had a completely satisfactory singularity model or geometry package for the new objectives. Accordingly, in the development of VSAERO these features were given prime consideration.

Various singularity models were investigated for the new program including symmetrical singularities (5), high-order formulations and numerical integration. Finally, a low-order formulation based on internal Dirichlet boundary conditions was chosen. This formulation is described in Section 2. The numerical procedure for the method, which employs quadrilateral panels of constant doublet and source distributions, is described in Section 3. The description includes details of the extended geometry package for the VSAERO program. Correlation studies are examined in Section 4; these include a number of basic test cases involving exact, nominally exact and also experimental data.

2.0 FORMULATION

2.1 Flow Equation

In order to obtain a solution to the flow problem the surface of the configuration is assumed to be at rest in a moving airstream. Regions of the flow field that are dominated by viscous and rotational effects are assumed to be confined to thin surface boundary layers and wakes. The rest of the flow field is assumed to be inviscid, irrotational and also incompressible.

Figure 1 shows a streamwise section taken through a wing and its wake. The section indicates the surface, S , of the wing, the surface (upper and lower) of the wake, W , and an outer surface, S_∞ , which encloses the complete flow problem at infinity. The total surface, $S + W$, divides space into two regions: the external region which contains the flow field of interest and the inner region which contains a fictitious flow. Velocity potential fields, ϕ and ϕ_i , are assumed to exist satisfying Laplace's equation in the flow field and in the inner region, respectively; i.e.,

$$\nabla^2 \phi = 0 \quad \text{in the flow field}$$

and

$$\nabla^2 \phi_i = 0 \quad \text{in the inner region.}$$

Next, apply Green's Theorem to the inner and outer regions and combine the resulting expression (see Lamb (6)). This yields the following expression for the velocity potential, ϕ_P , anywhere in the two regions, expressed in terms of surface integrals of the velocity potential and its normal derivative over the boundary surface:

$$\begin{aligned} \phi_P = & \frac{1}{4\pi} \iint_{S+W+S_\infty} (\phi - \phi_i) \mathbf{n} \cdot \nabla \left(\frac{1}{r} \right) dS \\ & - \frac{1}{4\pi} \iint_{S+W+S_\infty} \frac{1}{r} \mathbf{n} \cdot (\nabla \phi - \nabla \phi_i) dS \end{aligned} \quad (1)$$

where r is the distance from the point, P , to the element, dS , on the surface and \mathbf{n} is the unit normal vector to the surface pointing into the fluid.

The first integral in Eq. (1) represents the disturbance potential from a surface distribution of doublets with density $(\phi - \phi_i)$ per unit area and the second integral represents the contribution from a surface distribution of sources with density $-\mathbf{n} \cdot (\nabla \phi - \nabla \phi_i)$ per unit area. The singularities, therefore, represent the jump in conditions across the boundary; the doublet

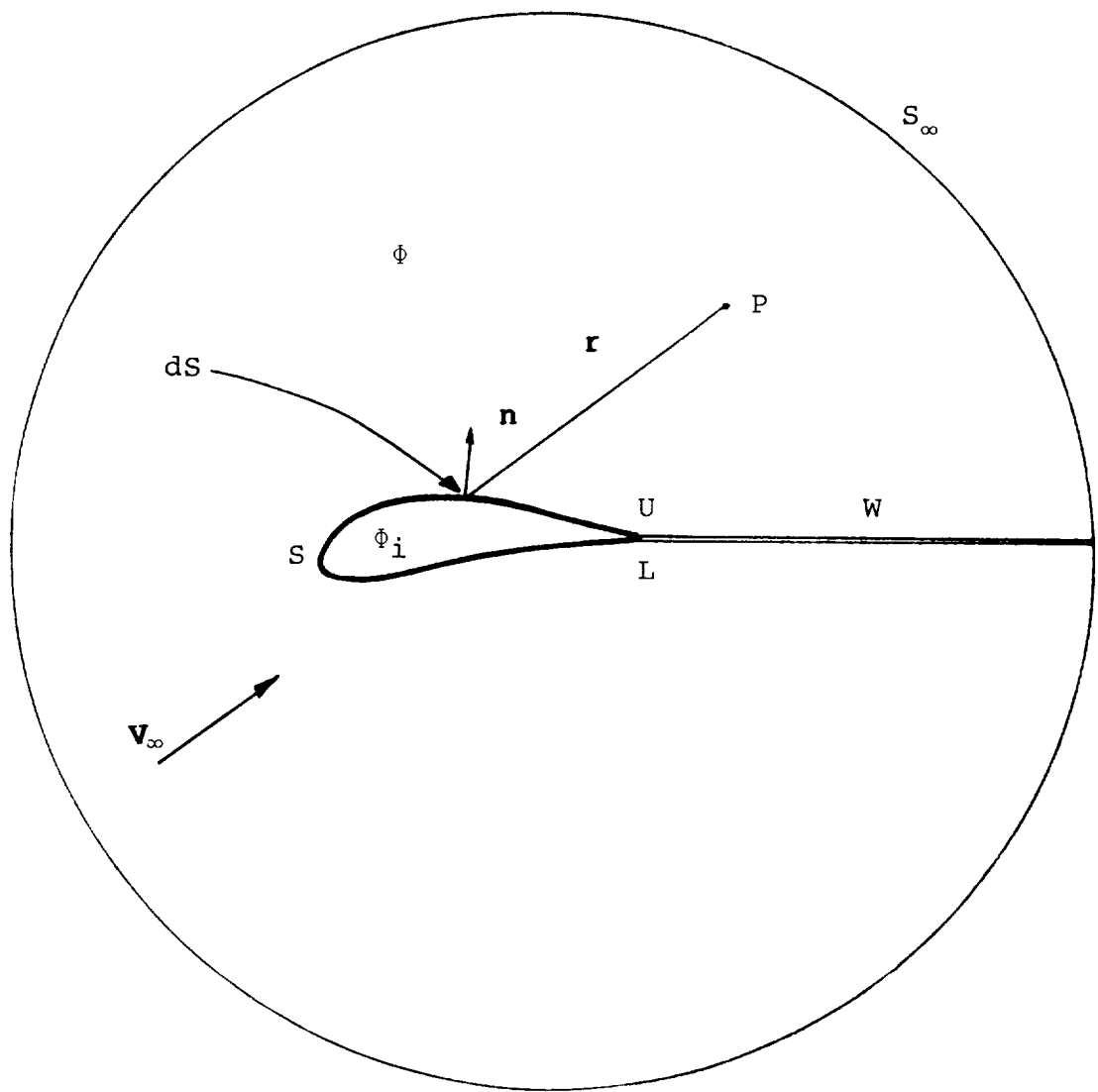


Figure 1. Section through the Idealized Flow Model.

density represents the local jump in potential and the source density represents the local jump in the normal component of velocity.

Examine Eq. (1) separately over the three surfaces, S, W, S_∞ , as indicated in Figure 1.

The surface at infinity, S_∞ , can be regarded as a large sphere centered on P. The local conditions at that boundary consist only of the uniform onset velocity, V_∞ , the disturbance at that distance due to the configuration having essentially disappeared. The surface integrals in Eq. (1) taken over S_∞ then reduce to $\phi_{\infty P}$; i.e., the velocity potential at point, P, due to the onset flow.

The upper and lower wake surfaces, W, are assumed to be infinitesimally close to each other for the present problem; i.e., thin wakes. (A simplified thick wake representation is described in References 7 and 8.) In this case the corresponding upper and lower elements can be combined and the ϕ_i term for this part of the integral disappears. Furthermore, if we neglect entrainment into the wake surface, then the jump in normal velocity component, $\mathbf{n} \cdot (\nabla\phi_U - \nabla\phi_L)$, is zero and so the source term in Eq. (1) disappears for the wake contribution. (Note that entrainment modeling could be included given a distribution of the entrainment normal velocity.)

With the above conditions, Eq. (1) becomes:

$$\begin{aligned} \phi_P = & \frac{1}{4\pi} \iint_S (\phi - \phi_i) \mathbf{n} \cdot \nabla \left(\frac{1}{r}\right) dS \\ & - \frac{1}{4\pi} \iint_S \frac{1}{r} \mathbf{n} \cdot (\nabla\phi - \nabla\phi_i) dS \\ & + \frac{1}{4\pi} \iint_W (\phi_U - \phi_L) \mathbf{n} \cdot \nabla \left(\frac{1}{r}\right) dW + \phi_{\infty P} \end{aligned} \quad (2)$$

The normal, \mathbf{n} , on surface, W, points upwards in this case.

If the point, P, lies on the surface, S, then the integral becomes singular on S. To evaluate the local contribution the point, P, is excluded from the integral by a local spherical deformation of the surface centered on P. For a smooth surface the local deformation is a hemisphere and the local contribution obtained in the limit as the sphere radius goes to zero is

$\frac{1}{2}(\phi - \phi_i)_P$, which is half the local jump in potential across the surface at P. Note that the first potential in the expression is on the side of the surface on which P lies, or, more conveniently, the sign can be changed for the point on the other side. For example, if P is on the inside surface of S, then Eq. (2) becomes:

$$\begin{aligned} \phi_P = & \frac{1}{4\pi} \iint_{S-P} (\phi - \phi_i) \mathbf{n} \cdot \nabla\left(\frac{1}{r}\right) dS - \frac{1}{2}(\phi - \phi_i)_P \\ & - \frac{1}{4\pi} \iint_S \frac{1}{r} \mathbf{n} \cdot (\nabla\phi - \nabla\phi_i) dS \\ & + \frac{1}{4\pi} \iint_W (\phi_U - \phi_L) \mathbf{n} \cdot \nabla\left(\frac{1}{r}\right) dW + \phi_{\infty_P} \end{aligned} \quad (3)$$

2.2 Boundary Conditions

A solution to Eq. (3) must satisfy a number of known boundary conditions which can be imposed--or in the case of the wake--implied at the outset. On the surface, S, the external Neumann boundary condition must be satisfied.

$$\mathbf{n} \cdot \nabla\phi = -V_N - \mathbf{n} \cdot \mathbf{V}_S \text{ on } S \quad (4)$$

where V_N is the resultant normal component of velocity relative to the surface. V_N is zero for the case of a solid boundary with no transpiration; non-zero values are used to model boundary layer displacement effect, entrainment and also inflow/outflow for engine inlet/exhaust modeling. \mathbf{V}_S is the local velocity of the surface; this may be composed of several parts due to body rotation (e.g., pitch oscillation (9), or helicopter blade rotation (10)), arbitrary motion (11), body growth (12), etc. For the present problem the surface of the configuration is assumed steady in a body-fixed coordinate system and so \mathbf{V}_S is zero.

Hence,

$$\mathbf{n} \cdot \nabla\phi = -V_N \text{ on } S \quad (5)$$

The wake surface, W, cannot support a load and so the doublet distribution, $\phi_U - \phi_L$, on W must satisfy a zero-force condition.

Consider an element, dW , of the wake surface with local unit normal, \mathbf{n} . The local vorticity vector associated with the doublet distribution, $\phi_U - \phi_L$, has the density

$$\boldsymbol{\gamma} = -\mathbf{n} \times \nabla(\phi_U - \phi_L) \quad (6)$$

The elementary force exerted on the element, dW , in the presence of the local mean velocity, \mathbf{V} , is (from the Kutta-Joukowski Law):

$$\delta \mathbf{F} = \rho \mathbf{V} \times \boldsymbol{\gamma} dW$$

where ρ is the local density. And since the force must be zero, it follows that

$$\mathbf{V} \times \boldsymbol{\gamma} = 0.$$

Substitute for $\boldsymbol{\gamma}$ from Eq. (6):

$$\mathbf{V} \times \{\mathbf{n} \times \nabla(\phi_U - \phi_L)\} = 0$$

and expand

$$\mathbf{n} \mathbf{V} \cdot \nabla(\phi_U - \phi_L) - \mathbf{V} \cdot \mathbf{n} \nabla(\phi_U - \phi_L) = 0. \quad (7)$$

Equation (7) is satisfied when $\mathbf{V} \cdot \mathbf{n} = 0$; i.e., the surface, W , is aligned with the local flow direction, and $\mathbf{V} \cdot \nabla(\phi_U - \phi_L) = 0$. In the latter case, the gradient of the doublet distribution in the direction of the local mean flow is zero; in other words, the wake doublet distribution is constant along mean streamlines in the wake surface. The doublet value on each streamline is, therefore, determined by the condition at the point where the streamline "leaves" the surface, S . Clearly, at the outset of the problem with both the doublet distribution and wake location unknown, an iterative approach is necessary to obtain a solution. When a converged solution is obtained the upstream edge of the wake, W --and hence the trailing edge of the surface, S --carries no load and so the Kutta trailing-edge condition will be satisfied. At the outset, therefore, the Kutta condition is implied simply by shedding the trailing-edge potential jump ($\phi_U - \phi_L$) as a constant down each "streamwise" line on an initially prescribed wake surface. An explicit Kutta condition in which the doublet gradients on the upper and lower surfaces at the trailing edge are equated to cancel has been used on occasion, but in the formulations described below, this does not appear to be necessary.

2.3 Choice of Singularity Model

In principle, a given flow field can be constructed from an infinite number of combinations of doublet and source distributions on the surface, S , each combination producing a different flow in the inside region. In practice, however, there may be only a small number of singularity combinations which are suitable as a basis for a well behaved numerical model; i.e., one that is accurate, convenient to use and robust (insensitive to user abuse).

A unique combination of singularities can be obtained in Eq. (3) in a number of ways. One way is to specify one of the singularity distributions and to solve for the other using boundary conditions only on one side of the boundary. There are several examples of this: in the source-only formulation (13) the doublet distribution is set to zero; in the doublet-only formulation, e.g., (3) and (4), the source distribution is set to zero; in program VIP3D (2), the doublet distribution (or vorticity) is specified and the method solves for the source distribution; the reverse of the latter has also been used, i.e., specifying the source distribution--usually related to the thickness distribution--and solving for the doublet or vorticity distribution.

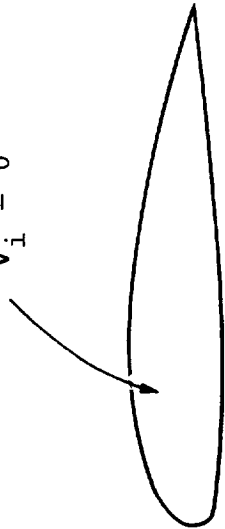
Another way of achieving a unique combination of singularities is to apply certain constraining relationships on the singularity distributions. The "symmetrical singularity method" (5) is one example of this and was examined briefly at the start of the VSAERO program development.

One characteristic that separates "good" singularity models from "bad" ones from the numerical point of view is that the flow field generated in the inner region by a "good" model is rather benign and related to the boundary. This is usually not the case for a "bad" model. In other words, when passing through the boundary, S , the jump from the internal flow to the external flow should be small--thus requiring a minimum of perturbation from the singularities (Eq. (3)). "Bad" singularity methods were observed to have very large internal cross flow between the upper and lower surfaces of wings and required high panel densities in order to achieve acceptable accuracy in the flow solutions. This resulted in a push towards high-order formulation which, for subsonic flows at least, proved quite unnecessary.

One way of achieving "good" characteristics is to treat the internal flow directly in Eq. (3). This is, in fact, another way of obtaining a unique singularity distribution--in this case by specifying boundary conditions on both sides of the surface, S . Earlier methods (14), (15) specified the velocity on the inside surface of S . Alternatively, the inner velocity potential, Φ_i , can be specified directly in Eq. (3). This is referred to as an internal Dirichlet boundary condition. Three possible internal flows were examined for the VSAERO program, Figure 2. Two of

$$\phi_i = \text{CONSTANT}$$

$$\mathbf{V}_i = 0$$



\mathbf{V}_∞
(i) Stagnation Inside

$$\phi_i = \phi_\infty$$

$$\mathbf{V}_i = \mathbf{V}_\infty$$

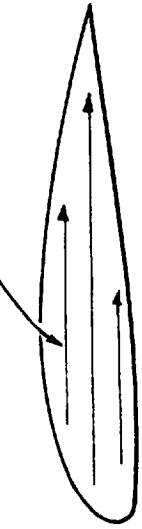


\mathbf{V}_∞
(ii) Zero Perturbation Inside

z
 k

$$\phi_i = -x V_\infty \cos \alpha$$

$$\mathbf{V}_i = i V_\infty \cos \alpha$$



x
 i
(iii) Chordwise Flow Inside

α
 \mathbf{V}_∞

Figure 2. Three of the Possible Internal Flows.

these are described below, the third one, in which the internal flow was aligned with the wing chord line (e.g., $\phi_i = -xV_\infty \cos \alpha$) was examined in a two-dimensional pilot program only. Although this worked very well, the formulation was not as convenient as the other two. Even so, it would be a useful member in a possible general scheme in which the user could select a suitable internal flow for each component in a complicated configuration.

(i) Zero Flow Inside

Consider first the interior stagnation condition which was implied by earlier doublet-only codes (e.g., References 3 and 4) and which used the exterior Neumann boundary condition, $\mathbf{V} \cdot \mathbf{n} = 0$. For the present formulation, set $\phi_i = \text{constant} = 0$, say in Eq. (3), giving

$$\begin{aligned} \phi_P = 0 = & \frac{1}{4\pi} \iint_{S-P} \phi \mathbf{n} \cdot \nabla \left(\frac{1}{r} \right) dS - \frac{1}{2} \phi_P \\ & - \frac{1}{4\pi} \iint_S \frac{1}{r} \mathbf{n} \cdot \nabla \phi dS \\ & + \frac{1}{4\pi} \iint_W (\phi_U - \phi_L) \mathbf{n} \cdot \nabla \left(\frac{1}{r} \right) dW + \phi_{\infty P} \end{aligned} \quad (8)$$

The doublet distribution is now the total velocity potential at the surface and the source distribution is now the total normal velocity of the fluid at the surface, S. This must satisfy the external Neumann boundary condition (Eq. 5); i.e.,

$$\mathbf{n} \cdot \nabla \phi = -V_N$$

This term can be used directly in the second integral of Eq. (8).

For the solid boundary problem, i.e., zero transpiration, V_N is zero and the source term disappears leaving

$$\begin{aligned} & \frac{1}{4\pi} \iint_{S-P} \phi \mathbf{n} \cdot \nabla \left(\frac{1}{r} \right) dS - \frac{1}{2} \phi_P \\ & + \frac{1}{4\pi} \iint_W (\phi_U - \phi_L) \mathbf{n} \cdot \nabla \left(\frac{1}{r} \right) dW + \phi_{\infty P} = 0 \end{aligned} \quad (9)$$

This is by far the simplest formulation for the lifting case with no transpiration. It is, in fact, even simpler than the original zero-lift source method based on the external Neumann boundary condition (13). In a low-order formulation (i.e., constant doublets on flat panels) the method has some minor problems associated with numerical differencing for velocities and with the effect of panel arrangement on accuracy (16). These problems can be alleviated by separating ϕ into a known part and an unknown part--the latter being as small as possible.

The most convenient breakdown is to use the onset flow potential as the known part; i.e., $\phi = \phi_\infty + \phi$. The known part, ϕ_∞ , and its velocity field, \mathbf{V}_∞ , are used directly in the formulation. The solution for ϕ and the subsequent numerical differentiation for surface velocity are then less prone to numerical error.

For the general case with transpiration, inlet flows, jets and unsteady conditions, the source term must be present and so the advantage of the doublet-only formulation diminishes. In the meantime an alternative "zero internal perturbation" formulation had become popular in other methods and is considered below.

(ii) Internal Flow Equal to the Onset Flow

The internal Dirichlet boundary condition, $\phi_i = \phi_\infty$, was used earlier by Johnson and Rubbert (17) and also Bristow and Grose (18) in high-order formulations. With $\phi_i = \phi_\infty$ and $\phi_P = \phi_\infty$, Eq. (3) becomes:

$$\begin{aligned} & \iint_{S-P} \phi \mathbf{n} \cdot \nabla \left(\frac{1}{r} \right) dS - \frac{1}{2} \phi_P + \iint_W (\phi_U - \phi_L) \mathbf{n} \cdot \nabla \left(\frac{1}{r} \right) dW \\ & - \iint_S \frac{1}{r} \mathbf{n} \cdot (\nabla \phi - \nabla \phi_\infty) dS = 0 \end{aligned} \quad (10)$$

where ϕ , the perturbation potential on the exterior surface, is now the doublet density; i.e.,

$$4 \pi \mu = \phi = \Phi - \phi_\infty \quad (11)$$

The source distribution in this formulation is

$$4 \pi \sigma = - \mathbf{n} \cdot (\nabla \phi - \nabla \phi_\infty)$$

Expanding this expression and substituting for $\mathbf{n} \cdot \nabla\phi$ from the external Neumann boundary condition in Eq. (5):

$$4\pi\sigma = V_N - \mathbf{n} \cdot \mathbf{V}_\infty$$

The source distribution is therefore established at the outset.

Again, for solid boundary conditions, V_N is zero; for the more general case here, V_N may have two parts representing (i) boundary layer displacement effect using the transpiration technique (2), and (ii) inflow/outflow for engine inlet/exhaust modeling.

Thus,

$$4\pi\sigma = \frac{\partial}{\partial s} (V_e \delta^*) + V_{\text{NORM}} - \mathbf{n} \cdot \mathbf{V}_\infty \quad (12)$$

The boundary layer term is set to zero for the first potential flow solution; on subsequent iterations it is updated by coupled boundary layer calculations. The V_{NORM} term has a positive value for outflow and negative for inflow.

Compared with the zero internal flow formulation (Eq. 9), the present formulation (Eq. (10) is more forgiving for "bad" panel arrangements (e.g., Reference 16) and is the current formulation in the VSAERO program. The reason for its better behavior probably arises from the smaller jump in the flow condition from the inner to the outer flow; i.e., the singularity strengths are smaller. However, there are situations where this is not the case; e.g., a wing at large angle of attack or a powered nacelle in zero onset flow. In other words, it may be desirable to provide a capability that allows the internal flows to be specified independently of the onset flow so that they can comply more closely with the shape of each component.

Once the doublet solution is known, then Eq. (3) can be applied to determine the velocity potential field, the gradient of which gives the velocity field. For the present formulation, Eq. (3) becomes:

$$\begin{aligned} \phi_P = & \iint_S \mu \mathbf{n} \cdot \nabla\left(\frac{1}{r}\right) dS + K\mu_P + \iint_S \frac{\sigma}{r} dS \\ & + \iint_W \mu_W \mathbf{n} \cdot \nabla\left(\frac{1}{r}\right) dW + \phi_{\infty P} \end{aligned} \quad (13)$$

Where the doublet, μ , and source, σ , are taken from Eqs. (11) and (12), respectively and $\mu_W = \phi_U - \phi_L$ is the wake doublet distribution. The factor, K , has different values depending on the location of the point, P ; if P lies off the surface, then $K = 0$; if P lies on a smooth part of the surface, then $K = 2\pi$ if P is on the outside, and $K = -2\pi$ if P is on the inside; if P is at a crease in the surface, then K takes the value of the appropriate solid angle contained at the crease. In each case when P is on the surface, then the surface integral terms in Eq. (13) exclude P .

If the potential field has been computed at a mesh of points then the velocity field can be generated using local numerical differentiation; i.e.,

$$\mathbf{v}_P = -\nabla\phi_P \quad (14)$$

Alternatively, the velocity field can be obtained by taking the gradient of Eq. (13) directly with respect to the coordinates of point P , thus forming the source and doublet velocity kernels. (This is the present approach in VSAERO.)

$$\begin{aligned} \mathbf{v}_P = & - \iint_S \mu \nabla (\mathbf{n} \cdot \nabla (\frac{1}{r})) dS - \iint_S \sigma \nabla (\frac{1}{r}) dS \\ & - \iint_W \mu_W \nabla (\mathbf{n} \cdot \nabla (\frac{1}{r})) dW + \mathbf{v}_\infty \end{aligned} \quad (15)$$

(The kernels will be developed further in Section 3.) The off-body velocity field is used in the wake-relaxation cycle, in off-body streamline calculations and for general flow-field information.

The discussion so far has been concerned with thick configurations having a distinct internal volume enclosed by the surface, S . If parts of the configuration are extremely thin (e.g., thickness/chord ratio $< 1\%$, say) or are wing-like and remote from the area of interest, then these parts may be represented by open surfaces. When the upper and lower parts of the surface are brought together, the corresponding upper and lower elements can be combined and Eq. (2) becomes

$$\begin{aligned} \phi_P = & \frac{1}{4\pi} \iint_S (\phi_U - \phi_L) \mathbf{n} \cdot \nabla \left(\frac{1}{r}\right) dS - \frac{1}{4\pi} \iint_S \frac{1}{r} \mathbf{n} \cdot (\nabla\phi_U - \nabla\phi_L) dS \\ & + \frac{1}{4\pi} \iint_W (\phi_U - \phi_L) \mathbf{n} \cdot \nabla \left(\frac{1}{r}\right) dW + \phi_{\infty P} \end{aligned} \quad (16)$$

If the normal velocity is continuous through the sheet then the term $\mathbf{n} \cdot (\nabla\phi_U - \nabla\phi_L) = 0$ and the source term disappears. (This is not a necessary step; the source term could be left in the equation for simple modeling of thickness effects.) Removing the source term does not preclude the use of non-zero normal velocity at the surface; the only restriction is that the normal velocity be continuous through the surface. Equation (16) can then be written:

$$\phi_P = \iint_S \mu \mathbf{n} \cdot \nabla \left(\frac{1}{r}\right) dS + \iint_W \mu_W \mathbf{n} \cdot \nabla \left(\frac{1}{r}\right) dW + \phi_{\infty P} \quad (17)$$

where $\mu = \frac{1}{4\pi} (\phi_U - \phi_L)$ is the jump in total potential across the sheet.

In order to satisfy the external Neumann boundary condition (Eq. (5)) the velocity expression is required. Hence, taking the gradient of Eq. (17) with respect to the coordinates of P,

$$\begin{aligned} \mathbf{v}_P = & - \iint_S \mu \nabla (\mathbf{n} \cdot \nabla \left(\frac{1}{r}\right)) dS \\ & - \iint_W \mu_W \nabla (\mathbf{n} \cdot \nabla \left(\frac{1}{r}\right)) dW + \mathbf{v}_{\infty} \end{aligned} \quad (18)$$

And, applying the boundary condition, $\mathbf{n}_P \cdot \mathbf{v}_P = v_{N_P}$ from Eq. (5), then

$$\begin{aligned}
& - \iint_S \mu \mathbf{n}_P \cdot \nabla(\mathbf{n} \cdot \nabla(\frac{1}{r})) dS \\
& - \iint_W \mu_W \mathbf{n}_P \cdot \nabla(\mathbf{n} \cdot \nabla(\frac{1}{r})) dW + \mathbf{n}_P \cdot \mathbf{v}_\infty = v_{N_P} \quad (19)
\end{aligned}$$

This is the basic equation for the unknown doublet distribution on thin surfaces (referred to as Neumann surfaces in VSAERO in accordance with their primary boundary condition). Again, the velocity kernels will be developed further in Section 3.

In the VSAERO program, thin and thick components may exist simultaneously in a configuration.

3.0 NUMERICAL PROCEDURE

The treatment of a given flow problem can be broken down into a number of distinct steps, each step having a certain function. These steps are shown in the VSAERO program outlined in Figure 3. The first step is to define the surface geometry of the configuration and to form the panel model. A matrix of influence coefficients is then formed; this represents a set of simultaneous linear algebraic equations resulting from a discretization of the flow equations in Section 2.0. The solution to these equations provides the surface doublet distribution from which the surface velocities and, hence, surface streamlines, pressures and body forces and moments can be analyzed. With the surface singularity distributions known, the wake-shape calculation can proceed, using computed off-body velocities. The new wake shape must then be repanelled and the matrix of influence coefficients modified for the next pass through the wake-shape iteration loop.

The surface flow solution can be passed to the boundary layer calculation. The computed boundary layer displacement growth rate is passed back to the matrix procedure where the right-hand side terms of the equation are modified for the next pass in the viscous/potential flow iteration loop, Figure 3. Finally, when both iteration loops have been completed, off-body surveys for velocity and streamline paths are processed.

The flow chart showing the relationships of subroutines which perform the above steps is given in Appendix A. Details of the steps are described in the following Subsections.

3.1 Geometrical Description

The surface geometry of the configuration to be analyzed is described in a global coordinate system (G.C.S.) which is a body-fixed frame of reference, Figure 4. The configuration is divided into a number of parts for convenience, Figure 5. The functions and use of these parts are described in detail in the Program User's Manual (1). Briefly, the two major parts are the (solid) SURFACE and the (flexible) WAKE. On a complicated configuration there may be several surfaces and several wakes. The surface and wake are further subdivided as described below.

3.1.1 Patch

Each surface is represented by a set of quadrilateral PANELS which are assembled into a regular array of rows and columns within PATCHES, Figure 6. Patches are grouped together under two headings (Figure 5), COMPONENTS and ASSEMBLIES for user convenience (1).

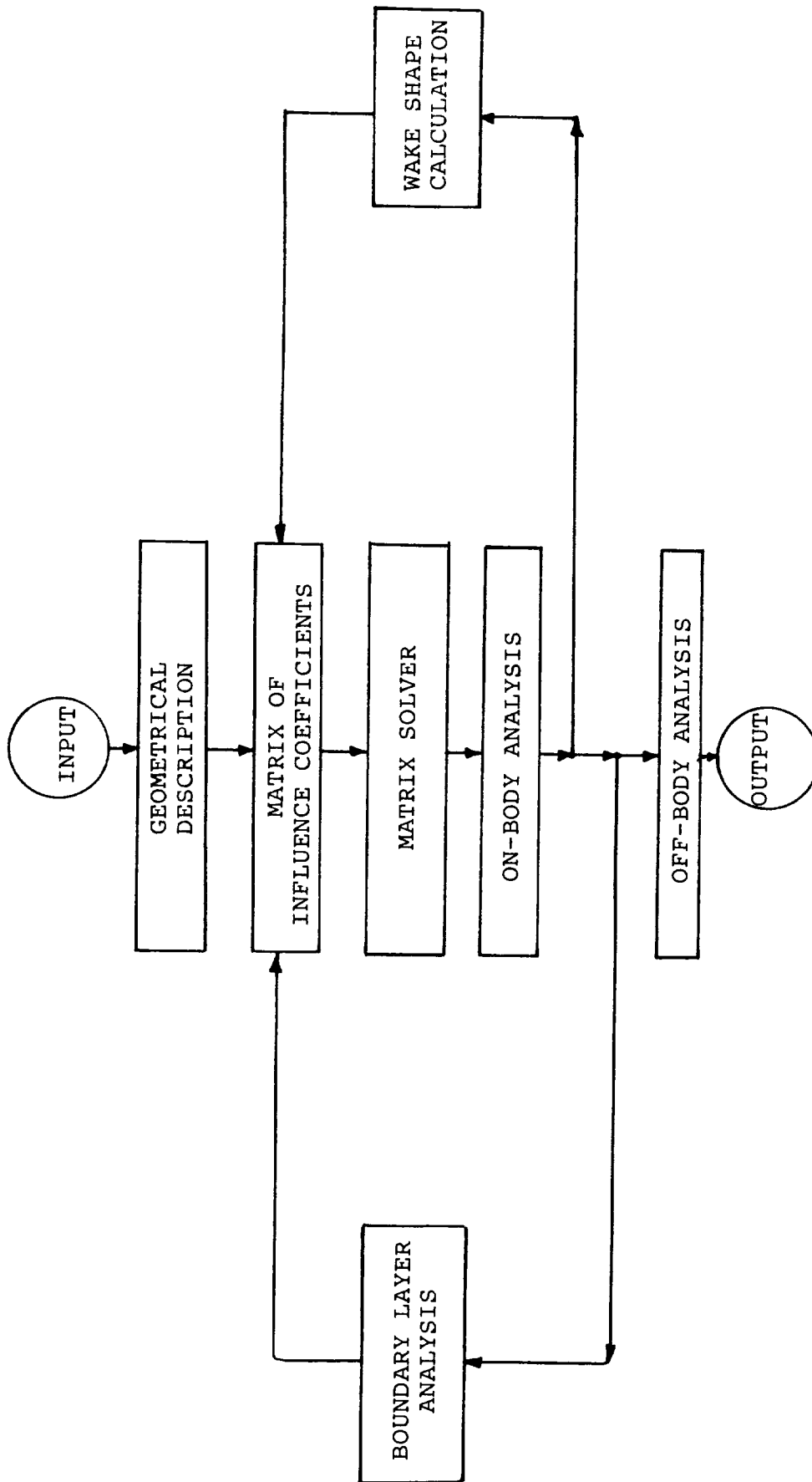


Figure 3. Outline of Steps in the VSAERO Program.

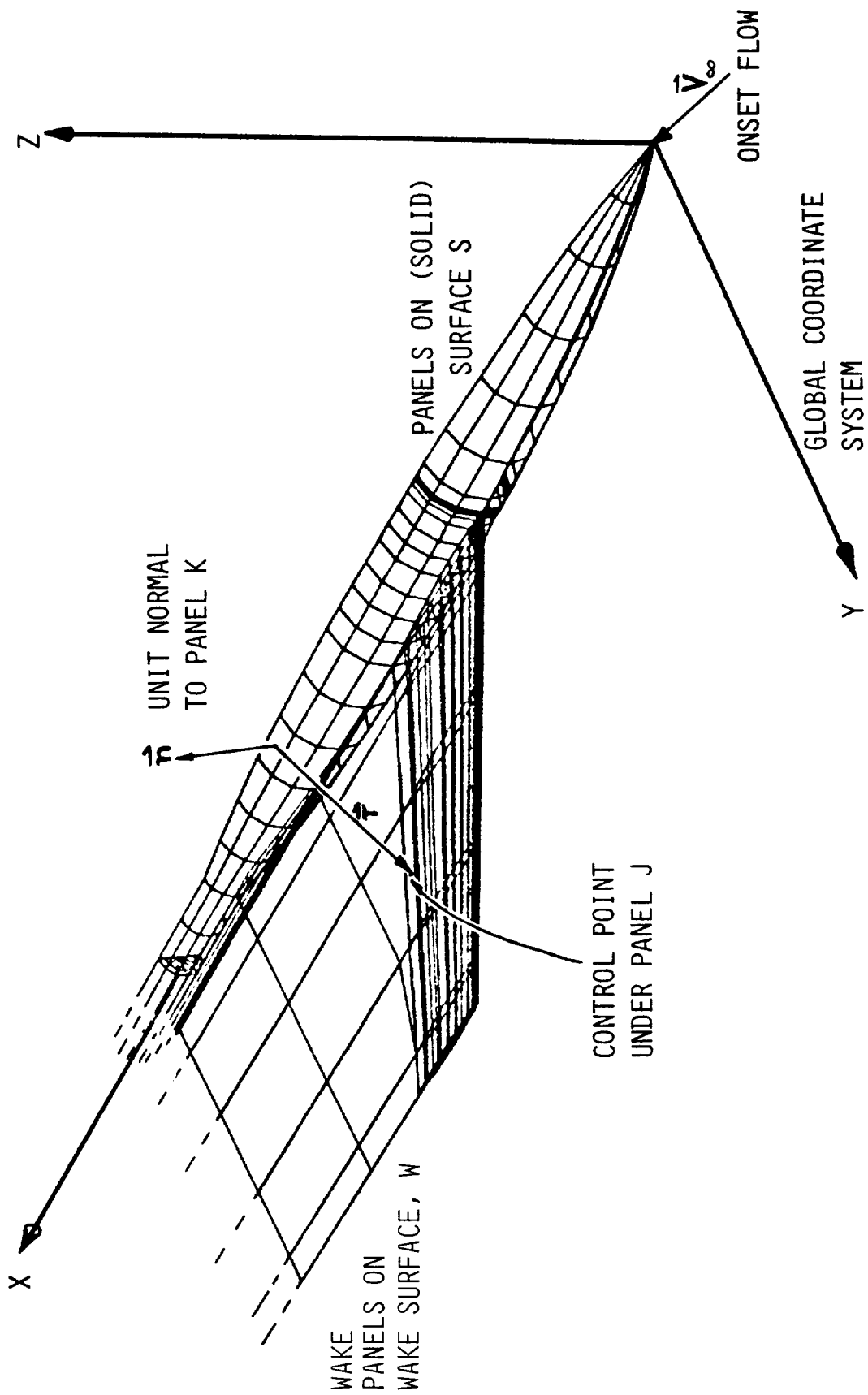


Figure 4. General Arrangement of the Configuration.

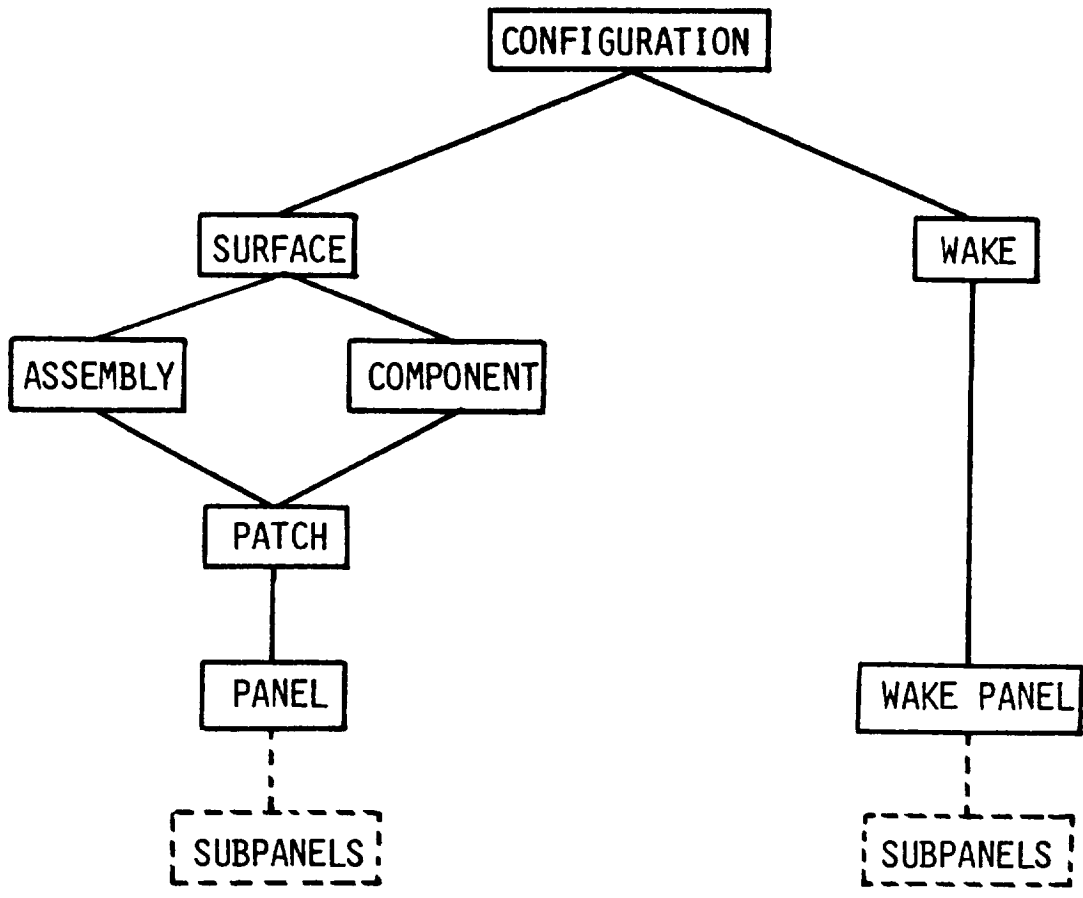


Figure 5. Configuration Hierarchy.

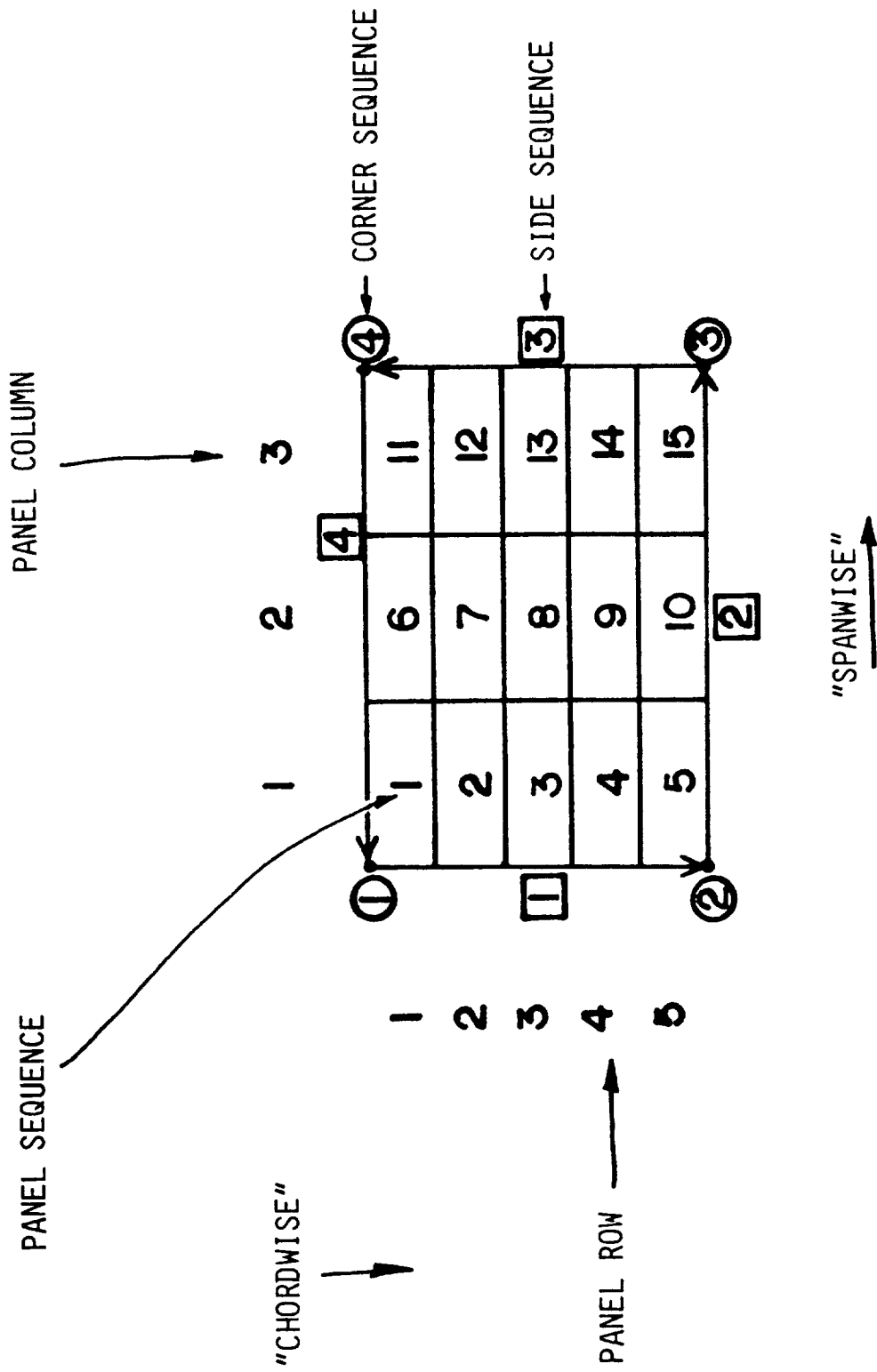


Figure 6. Patch Conventions.

Each patch has a user-supplied IDENT parameter. IDENT=1 and 2 identify patches on wings and fuselages, respectively; the main difference at this time is the printout of computed characteristics (see Subsection 3.4). Both of the above IDENT values are associated with thick surfaces and use the internal Dirichlet boundary condition. Patches with IDENT=3 are associated with thin (i.e., open) surfaces on which only the Neumann boundary condition is used. Again, the main difference as far as the user is concerned is a different printout of computed characteristics, in this case, pressure and velocity information is provided on both sides of these surfaces.

A patch is basically a four-sided shape when its surface is developed; i.e., "opened out". Because the initial objectives were directed towards wing surfaces, the terms "chordwise" and "spanwise" were adopted to describe the two directions across the patch, Figure 6. These terms are still used within the patch even when the patch has a more arbitrary orientation, e.g., on a fuselage.

The order of the sides of a patch must proceed in the anti-clockwise direction when viewed from the flow field, Figure 6. This is important as it affects the direction of the computed surface normal vector which must point into the external flow field (Subsection 3.1.2).

Patch geometry is defined using a set of "chordwise" lines called SECTIONS. The set of sections distributed in the "spanwise" direction across the patch define its surface, Figure 7. The points that are input to describe a section geometry are referred to as BASIC POINTS and are not necessarily panel corner points. From these points the program generates by interpolations a set of TEMPORARY CHORDWISE POINTS using information provided by the user on NODE CARDS (1). The actual panel corner points are obtained by interpolation along spanwise lines; these lines pass through a corresponding temporary chordwise point on each section. The interpolation scheme used in both directions uses a biquadratic equation and is described in Appendix B. The interpolation scheme is part of an automatic paneling procedure, use of which is optional: the user has the choice to input the actual panel corner points if he wants to. A number of input options are provided in the program to help the user generate the panel model (1).

3.1.2 Panel Geometry

The four corner points, R_i , $i=1,4$, defining a quadrilateral panel are in the same sequence as the corners of the parent patch, Figure 8. Two diagonal vectors are constructed from these points:

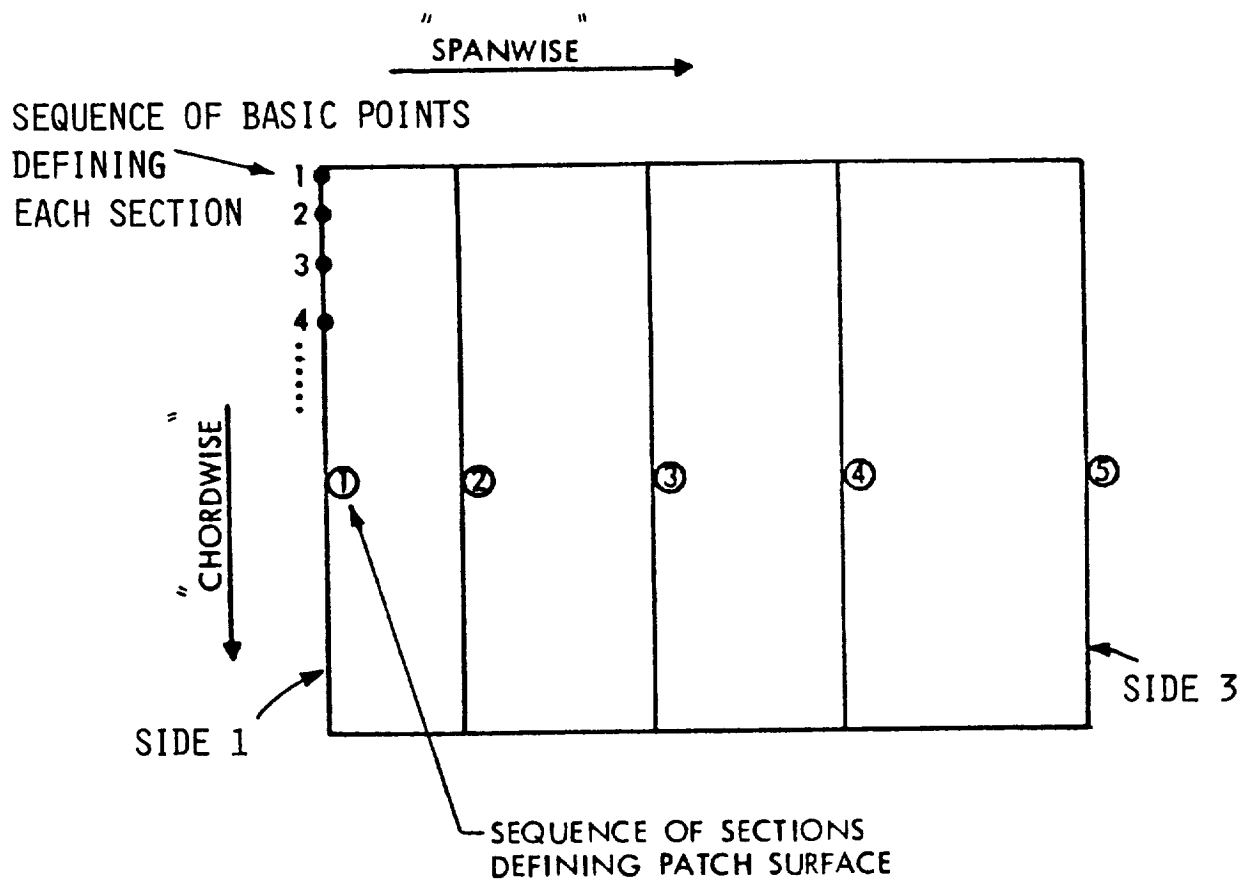


Figure 7. Sections Defining Patch Surface.

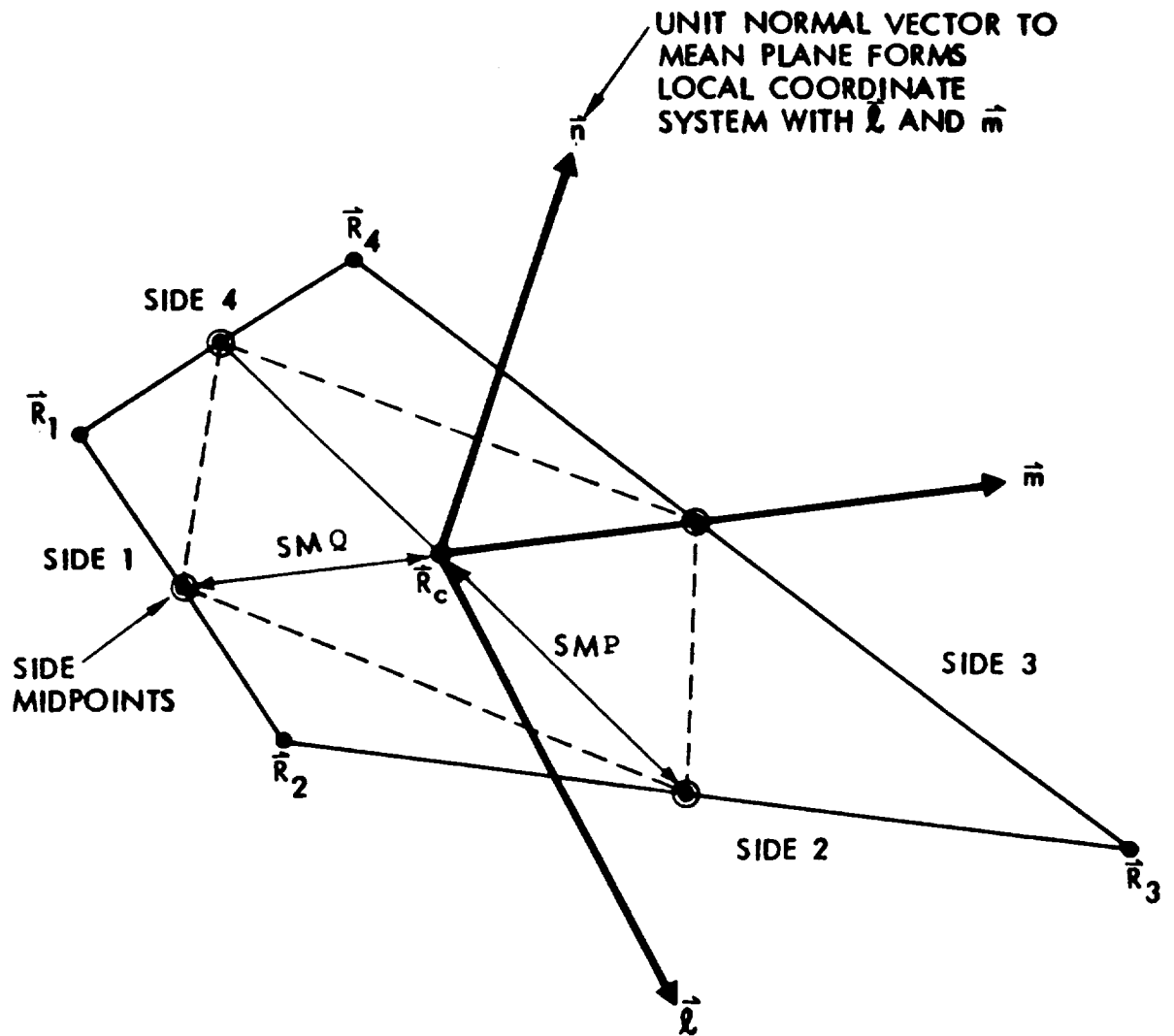


Figure 8. Panel Geometry.

$$\mathbf{D}_1 = \mathbf{R}_3 - \mathbf{R}_1$$

$$\mathbf{D}_2 = \mathbf{R}_4 - \mathbf{R}_2$$

The vector product of these diagonals produces a vector normal to the mean plane of the quadrilateral; i.e.,

$$\mathbf{n} = \mathbf{D}_1 \times \mathbf{D}_2 / |\mathbf{D}_1 \times \mathbf{D}_2|$$

The order of the sides, therefore, is important to ensure that the unit normal is always directed outwards from the surface into the flow field. The modulus of the diagonal vector product also provides the area of the quadrilateral projected onto the mean plane:

$$\text{AREA} = |\mathbf{D}_1 \times \mathbf{D}_2| / 2$$

The center point is defined as the mean of the four corner points:

$$\mathbf{R}_C = \frac{1}{4} \sum_{i=1}^4 \mathbf{R}_i$$

This point is also used as the panel's control point where the boundary conditions are satisfied (see Subsection 3.2).

Two unit tangent vectors, \mathbf{l} , \mathbf{m} , are constructed, which, together with \mathbf{n} form a right-handed orthogonal unit vector system for local coordinates, Figure 8. The origin of this system is the center point, \mathbf{R}_C .

Tangent vector, \mathbf{m} , is directed from \mathbf{R}_C to the mid-point of side 3 of the quadrilateral:

$$\mathbf{m} = \{(\mathbf{R}_3 + \mathbf{R}_4)/2 - \mathbf{R}_C\} / |(\mathbf{R}_3 + \mathbf{R}_4)/2 - \mathbf{R}_C|$$

Thus \mathbf{m} lies in the mean plane of the quadrilateral even if the corner points are not co-planar.

The tangent vector, \mathbf{l} , is constructed orthogonal to \mathbf{m} and \mathbf{n} :

$$\mathbf{l} = \mathbf{m} \times \mathbf{n}$$

The four corner points are projected onto the mean plane and expressed in terms of the local coordinate system. For example, the first point becomes

$$\mathbf{E}_1 = \mathbf{R}_1 - \mathbf{R}_C$$

which has components, E_{ξ_1} , E_{η_1} , in the ℓ and m directions, respectively, where

$$E_{\xi_1} = \mathbf{E}_1 \cdot \boldsymbol{\ell}; \quad E_{\eta_1} = \mathbf{E}_1 \cdot \mathbf{m}$$

The vertical offset, $\mathbf{E}_1 \cdot \mathbf{n}$, is the projection distance of the corner points from the mean plane and is a measure of the skew of the quadrilateral. On a skewed quadrilateral the four corner points are equidistant from the mean plane, two being above and two below. The magnitude of this offset should be kept small in relation to the size of the panel to avoid large holes in the singularity panel representation of the surface. The projected (flat) panel is used in the evaluation of influence coefficients (Subsection 3.2).

Finally, the half median lengths, SMP, SMQ, are evaluated for the quadrilateral. These are (Figure 8)

$$SMP = |(R_2 + R_3)/2 - R_C|$$

$$SMQ = |(R_3 + R_4)/2 - R_C|$$

These are the half-lengths of the diagonals of the parallelogram which is always formed when the mid-points of the adjacent sides of a quadrilateral are joined (even if the latter's corner points are not co-planar); the parallelogram lies in the mean plane of the quadrilateral and its area is half that of the projected quadrilateral.

Within each patch, the regular arrangement of panels causes the adjacent side mid-points of neighboring panels to coincide exactly. This allows the SMP and SMQ lengths of panels to be linked, respectively, in the chordwise and spanwise direction over the patch and thereby provides a close approximation to surface distances between panel centers. This feature is useful in the evaluation of the perturbation velocities (i.e., the derivative of μ with respect to surface distance, see Subsection 3.4).

Finally, the quantity (SMP + SMQ) is used as the average "size" of the panel when expressing the distance of a point from the panel in terms of panel size.

3.1.3 Panel Neighbors

In order that a reasonable two-way differentiation of the surface doublet distribution can be performed (see Subsection 3.4), it is important to locate quickly for each panel the set of four neighboring panels and their orientation. Each panel, therefore, keeps an array of four neighboring panels, $NABOR_i$,

$i=1,4$ (in the same sequence as its sides), together with the adjacent side numbers of those panels, $NABSID_i$, $i=1,4$, Figure 9.

Clearly, within the regular grid system of a patch, locating neighbors is easy; even so, the neighbor information is still stored to form a consistent system and to avoid repetitive calculations. Also, this allows neighbor relationships to be broken between pairs of panels, when, for example, a wake is shed from their common edge. This prevents a doublet gradient being evaluated across a line where there is an actual jump in potential (see Subsection 3.4).

Across the joints between patches panel neighbors are not immediately available; for example, one panel may be neighbor to several smaller panels on an adjoining patch. In order to locate these neighbors an automatic procedure has been installed in the code which scans patch side panels in a search for possible neighbors. In this search only patches within the same assembly are considered. "Undesirable" neighbors are quickly eliminated on the basis of relative geometry during the assembly of a short list of possible neighbors for each side panel. From this list of candidates one PREFERRED NEIGHBOR is selected. At this time, preference is given to the panel whose control point lies closest to a normal plane constructed on the side panel, Figure 10. This plane contains the side panel's control point, unit normal vector and the side mid-point at the patch edge.

3.1.4 Wakes

A wake consists of a number of quadrilateral wake panels which are assembled in streamwise columns. Each column is associated with an upper and a lower wake shedding panel with subscripts, KWPU, KWPL, respectively, Figure 11. The common edge of these two panels is the upstream edge of the wake column. the VSAERO program coding allows any panel edge in the configuration to shed a wake (1)--it is up to the user to specify a wake model that is physically realistic.

The streamwise edges of each column are identified as WAKE LINES, Figure 12. These lines are specified by the user to describe the initial wake; the user may describe the line geometry in as much detail as he likes (1). The program interrogates each line in relation to a system of vertical WAKE-GRID PLANES, Figure 11. The user specifies the location of these planes in accordance with the anticipated track of the wake; because the wake lines are represented by straight line segments between the wake-grid planes, regions where the wake lines are highly curved require an increased density of wake-grid planes.

Wake panels are contained between adjacent wake-grid planes and adjacent wake lines. The wake panel geometry is evaluated in the same way as the surface panels (Subsection 3.1.2) except that the mean plane is constrained to lie in the upstream edge (i.e.,

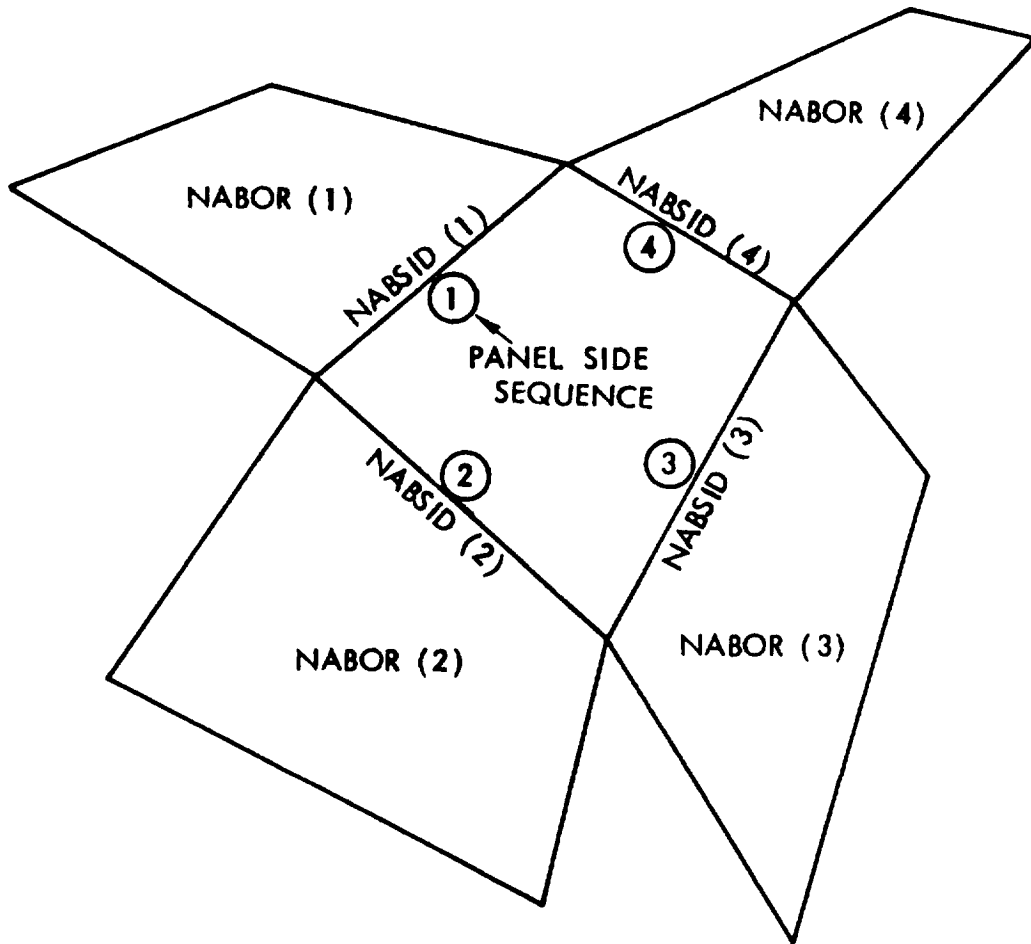


Figure 9. Panel Neighbor Information.

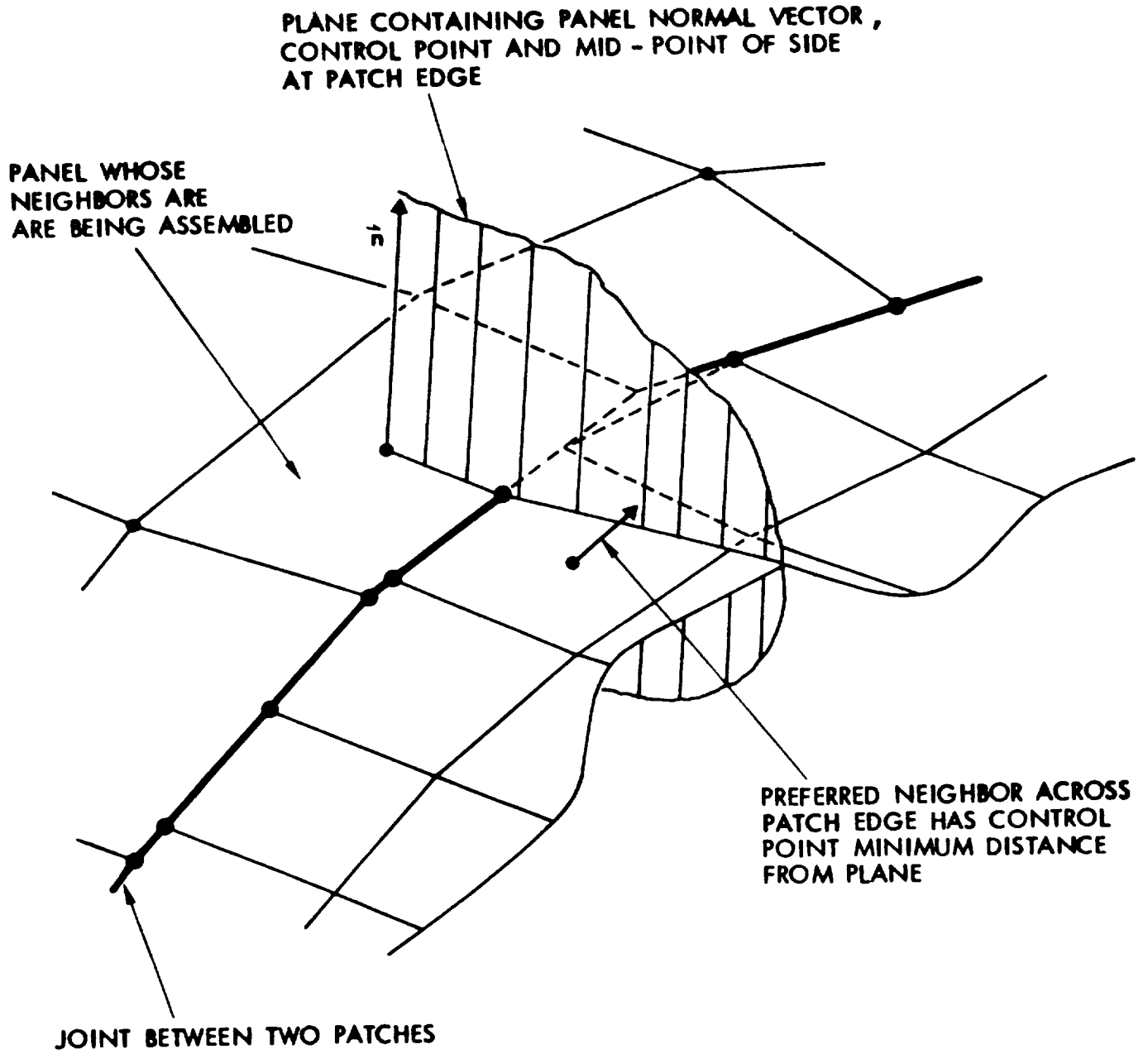


Figure 10. Panel Neighbors Across Patch Edges.

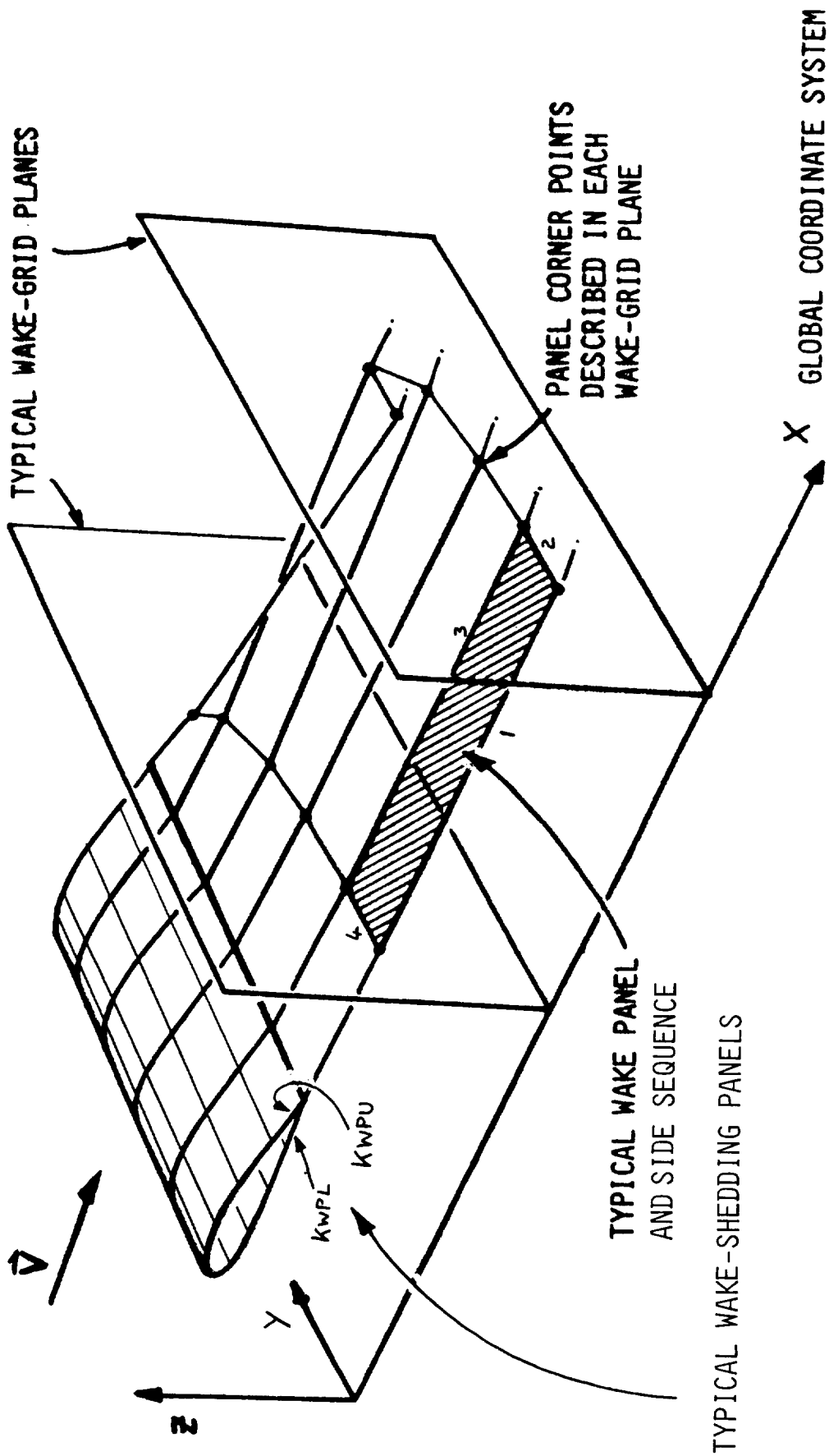


Figure 11. Wake-Grid-Plane Scheme.

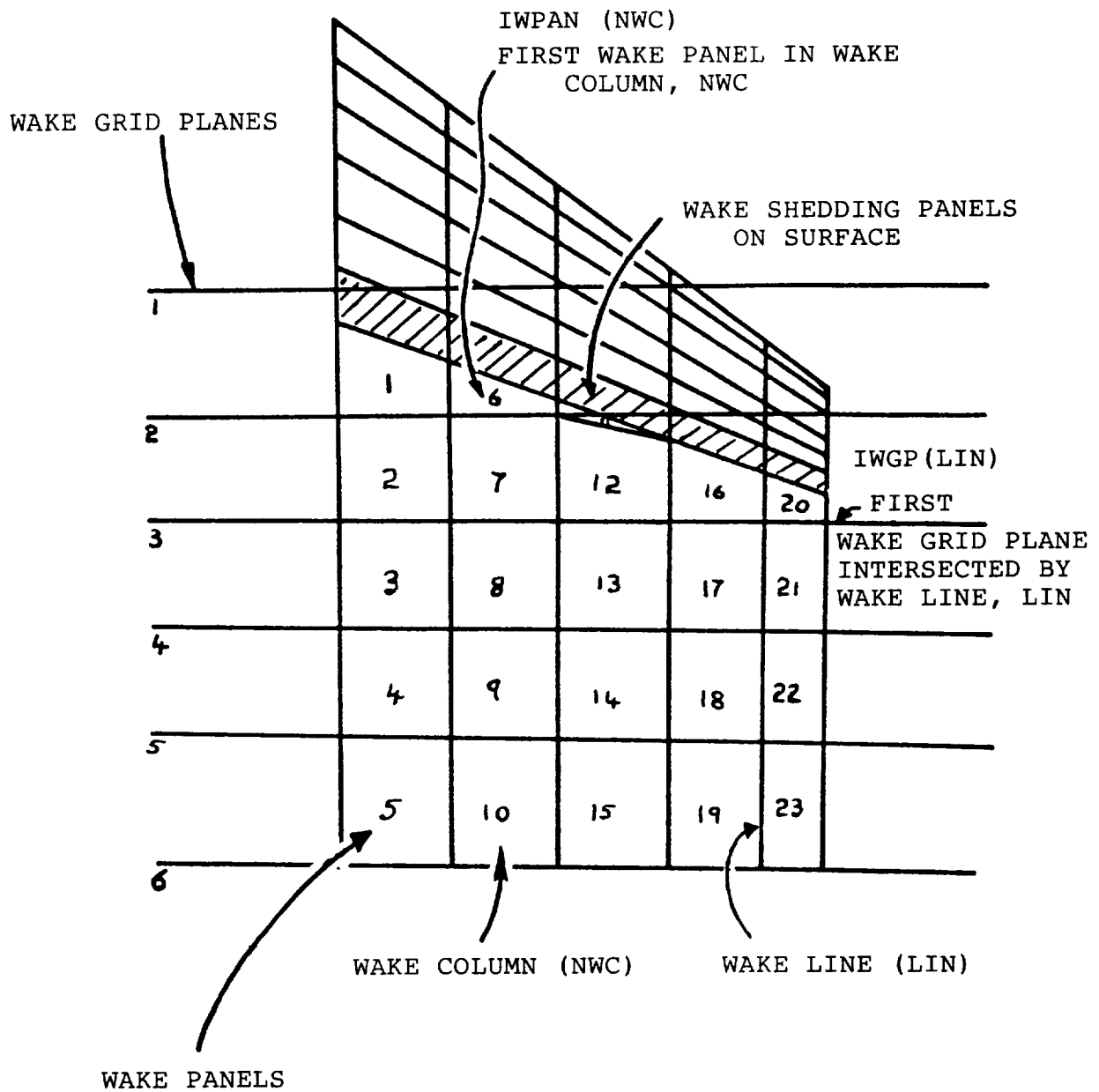


Figure 12. Wake Arrangement.

side 4) and to contain the mid-point of the downstream edge (side 2). In that way the projected wake panels are cleanly attached to the surface separation line even when the panels are skewed.

The wake geometry supplied by the user is used only for the initial solution. The program includes an iteration cycle in which the straight wake-line segments (i.e., panel edges 1 and 3) are aligned with the computed flow direction (see Subsection 3.5).

3.2 Matrix of Influence Coefficients

Equation (10) in Section 2.0 is a Fredholm integral equation of the second kind for the unknown velocity potential distribution over the body surface. A velocity potential distribution which satisfies Eq. (10) at every point of the body surface provides an exact solution for the inviscid, incompressible potential flow about the configuration surface through Eq. (13). In order to obtain a numerical solution the equation is satisfied only at a finite number of points on the surface; i.e., at one point (the control point) on each panel. Also, the doublet and source singularity distributions are assumed to be constant on each panel and the surface integrals in Eq. (10) are performed in closed form over each panel. These integrals, therefore, provide the influence coefficients per unit singularity strength for each panel. The total surface integrals then become summations over all panels and Eq. (10) is transformed into a set of simultaneous linear algebraic equations for the doublet strength on each panel.

$$\sum_{K=1}^{N_S} (\mu_K C_{JK}) + \sum_{L=1}^{N_W} (\mu_{W_L} C_{JL}) + \sum_{K=1}^{N_S} \sigma_K B_{JK} = 0; J=1, N_S$$

(20)

where μ and σ are given by Eqs. (11) and (12), respectively, and $C_{JJ} = -2\pi$.

N_S and N_W are the number of surface and wake panels, respectively. The quantities, B_{JK} and C_{JK} , are the perturbation velocity potential influence coefficients for the constant source and doublet distributions, respectively, on panel K acting on the control point of panel J; i.e., from Eq. (10).

$$B_{JK} = \iint_{\text{Panel K}} \frac{1}{r} dS$$

and

$$C_{JK} = \iint_{\text{Panel K}} \mathbf{n} \cdot \nabla \left(\frac{1}{r} \right) dS \quad (21)$$

where $\mathbf{n} \equiv \mathbf{n}_K$ is a constant for a flat panel, K, and r is the length of the vector from the surface elements, dS, of panel K to the control point of panel J. The gradient is taken with respect to the surface point.

Equation (20) is applied to all panels, J, that occur on "Dirichlet" patches (IDENT=1 or 2); i.e., on patches that are part of a "thick" boundary enclosing an inner volume. If the control point, J, is on a panel on a "Neumann" patch (IDENT=3), i.e., part of an open surface, then a discretized form of Eq. (19) is used.

$$\begin{aligned} & \sum_{K=1}^{N_S} (\mu_K E_{JK}) + \sum_{L=1}^{N_W} (\mu_W E_{JL}) \\ & + \sum_{K=1}^{N_S} \sigma_K D_{JK} + \mathbf{n}_J \cdot \mathbf{v}_\infty - V_{N_J} = 0 \end{aligned} \quad (22)$$

where

$$D_{JK} = \mathbf{n}_J \cdot \mathbf{v}_{\sigma_{JK}}$$

and

$$E_{JK} = \mathbf{n}_J \cdot \mathbf{v}_{\mu_{JK}} \quad (23)$$

are, respectively, the normal velocity influence coefficients for the source and doublet distributions on panel K acting at the

control point of panel J. The velocity vector influence coefficients for the source and doublet are, respectively,

$$\mathbf{v}_{\sigma_{JK}} = - \iint_{\text{Panel K}} \nabla_J \left(\frac{1}{r} \right) dS$$

and

$$\mathbf{v}_{\mu_{JK}} = - \iint_{\text{Panel K}} \nabla_J (\mathbf{n}_K \cdot \nabla \left(\frac{1}{r} \right)) dS \quad (24)$$

with the gradients, ∇_J , being taken with respect to the coordinates of point J.

Note that in generating Eq. (19) for Neumann patches, the source terms disappeared with the assumption of no jump in normal velocity through the surface. However, for the general problem involving a combination of thin and thick components the source term has been left in Eq. (22) to supply the contribution from source panels on thick boundaries.

The influence coefficients for the velocity potential and velocity are developed separately below. In each case the coefficient is determined completely by the geometric details of panel K and the coordinates of the Jth control point.

3.2.1 Velocity Potential Influence Coefficient

3.2.1.1 Doublet Contribution

Consider the doublet velocity potential influence coefficient from Eq. (21). After evaluating the gradient, this becomes

$$C_{JK} = \iint_{\text{Panel K}} \frac{\mathbf{n} \cdot \mathbf{r}}{r^3} dS \quad (25)$$

The integral is evaluated by considering each side of the (projected) panel in turn, each side having a pair of semi-infinite strips of opposing singularity strength equal to half the panel value, Figure 13. The strips lie in the mean plane of the panel and are aligned with the panel's ℓ axis. With the convention adopted for the panel sides (i.e., the side order is anticlockwise when viewed from the flow field) the singularity strength is given a positive sign to the left of the side and a negative sign to the right when looking in the direction of the side, Figure 13. When all four sides of the panel (or for any closed polygon, in fact) have been treated in this way then the contributions from all the overlapping strips cancel outside the panel and reinforce for unit singularity value over the panel.

Consider the contribution from one side. The kernel can be simplified by combining corresponding pairs of positive and negative elements, $d\xi$, dy , located at equal distance, ξ , from a point (x,y) on the side (Figure 14); i.e.,

$$C_{JK} = \frac{1}{2} \int_{y=y_a}^{y_b} \int_{\xi=0}^{\infty} \left\{ \frac{\mathbf{n} \cdot \mathbf{r}_1}{r_1^3} - \frac{\mathbf{n} \cdot \mathbf{r}_2}{r_2^3} \right\} d\xi dy \quad (26)$$

where

$$\begin{aligned} \mathbf{r}_1 &= \mathbf{R}(\eta) + \xi \boldsymbol{\ell} \\ \mathbf{r}_2 &= \mathbf{R}(\eta) - \xi \boldsymbol{\ell} \\ \mathbf{R}(\eta) &= \mathbf{a} - \eta \mathbf{s} \\ \eta &= (y - y_a) / (y_b - y_a) \end{aligned}$$

where y_a , y_b are the beginning and end of the projection of the side on the \mathbf{m} axis and \mathbf{a} is the position vector of the J^{th} control point relative to the start of this side (Figure 14).

The final expression for the doublet velocity potential contribution from side i of the panel is (using variables which closely follow the computer coding):

$$C_{JK_i} = \tan^{-1} \{ \text{RNUM/DNOM} \} \quad (27)$$

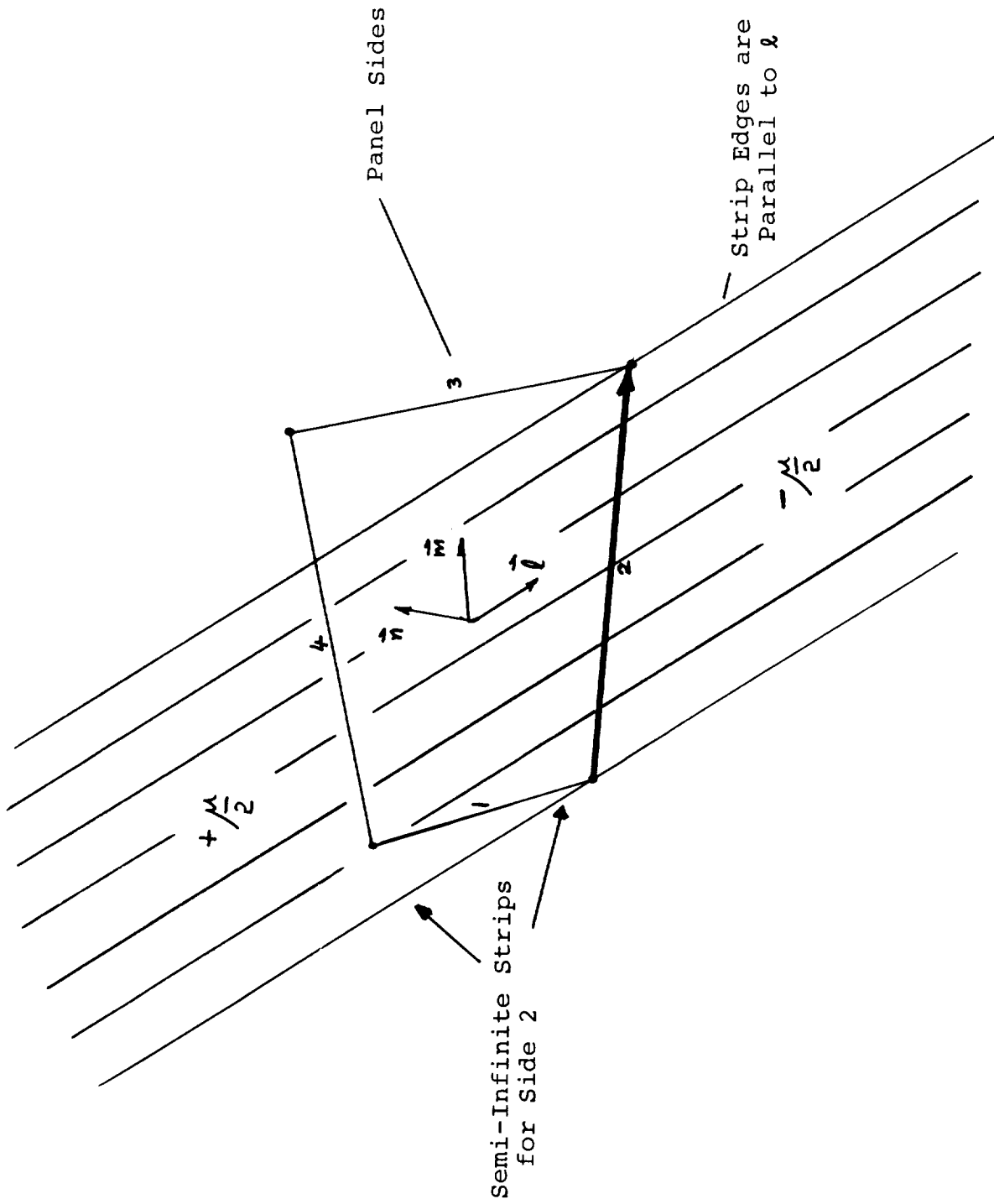


Figure 13. Model used in the Evaluation of the Surface Integrals.

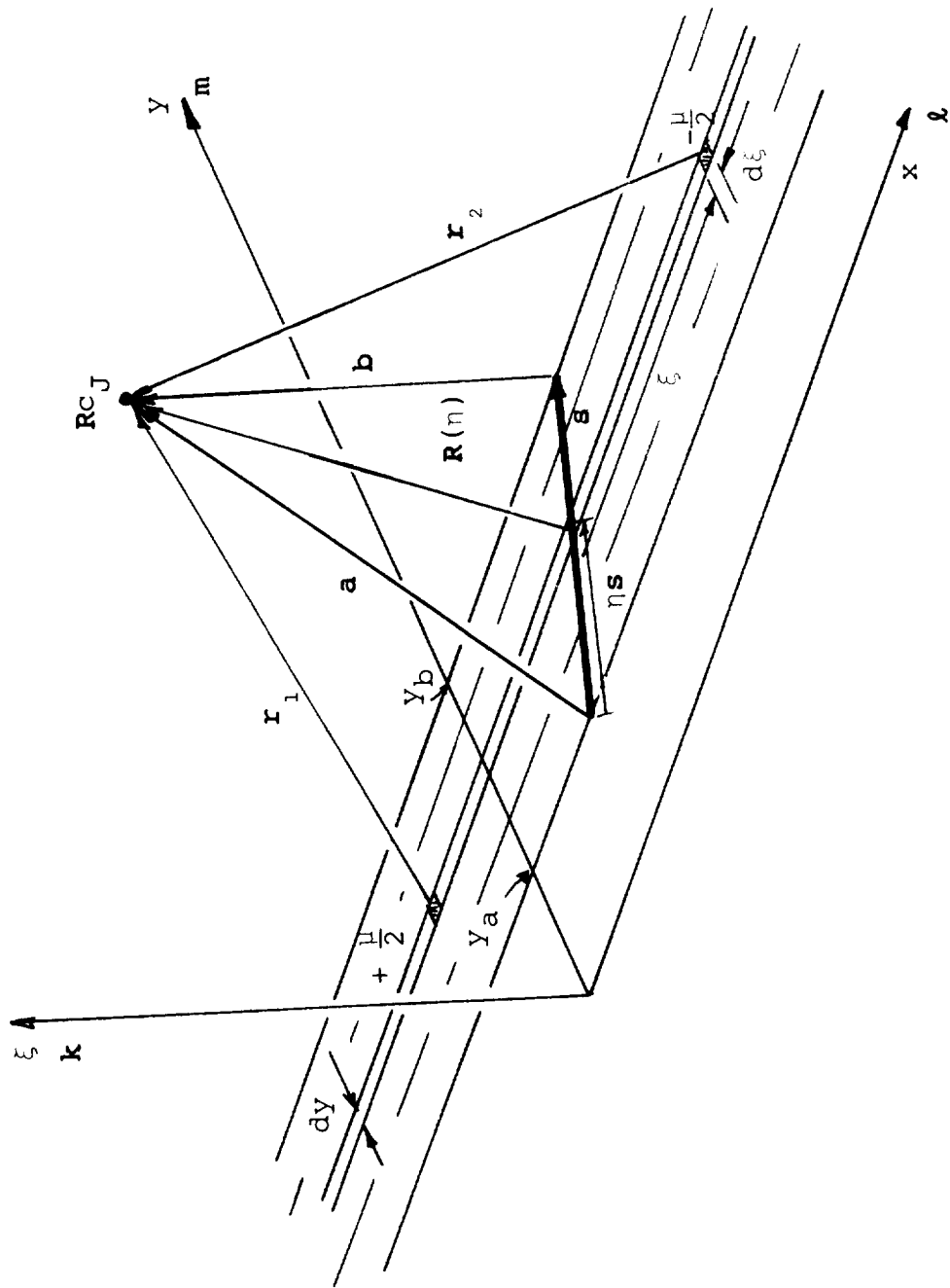


Figure 14. Evaluation of the Surface Integrals for One Side of a Panel.

where

$$RNUM = SM * PN * (B * PA - A * PB)$$

$$DNOM = PA * PB + PN^2 * A * B * SM^2$$

$$PN = P_{JK} \cdot n_K$$

$$P_{JK} = R_{C_J} - R_{C_K}$$

$$A = |a|$$

$$B = |b|$$

$$PA = PN^2 * SL + A1 * AM (= a \cdot \{\ell \times (a \times s)\})$$

$$PB = PN^2 * SL + A1 * BM = PA - A1 * SM$$

$$SM = s \cdot m$$

$$SL = s \cdot \ell$$

$$AM = a \cdot m$$

$$BM = b \cdot m$$

$$A1 = AM * SL - AL * SM (= n \cdot (s \times a))$$

b is the position vector of the J^{th} control point relative to the end of this side, Figure 14 (i.e., $b = a - s$)

The subscript, i , has been omitted from the above variables; a , b and s are constructed for each side in turn, noting that $a_i = b_{i-1}$.

There is a limiting condition as PN --the projected height of control point J from the mean plane of panel K --goes to zero:

$$\lim_{PN \rightarrow 0^+} (C_{JK_i}) \begin{cases} = \pm \pi & \text{within the strip (DNOM < 0)} \\ = \pm \frac{\pi}{2} & \text{on the edge of the strip (DNOM = 0)} \\ = 0 & \text{outside the strip (DNOM > 0)} \end{cases}$$

The positive sign occurs for points to the right of the side and negative to the left. If $PN \rightarrow 0^-$, all the above signs on π are reversed.

The total velocity potential influence coefficient for the unit doublet on the panel is the sum for all four sides, from Eq. (27).

$$C_{JK} = \sum_{i=1}^4 C_{JK_i} \quad (28)$$

The four arc-tangent functions in this summation can be combined into a single arc tangent; however, extreme care is required to ensure the resultant angle is in the correct quadrant in the range, $\pm 2\pi$.

For plane of symmetry and/or ground effect problems the contribution to C_{JK} from image panels (having the same singularity strength as the real panel) is evaluated simply by repeating the calculation for the real panel influencing the images of control point J. This is possible because the geometrical relationship between the image of panel K and the point J is identical to that of the actual panel K and image of point J (Figure 15). Hence, for a symmetrical problem in ground effect there would be four contributions for each panel, Figure 15. This treatment is more convenient than considering the image panels directly. The vertical plane of symmetry is the $y = 0$ plane in the G.C.S., while the ground plane is the $z = 0$ plane. Thus, for ground effect problems the configuration height and orientation above the ground require care during input (1).

The above expression for C_{JK} is used when panel J is close to panel K. When panel J is remote from panel K, i.e., in the far field, then a far-field formula is used under the assumption that the quantity, $\frac{\mathbf{n} \cdot \mathbf{r}}{r^3}$, in Eq. (25) is essentially constant over the panel. Then $\mathbf{r} = \mathbf{P}_{JK}$ and

$$C_{JK} = \frac{PN_{JK} * AREA_K}{P_{JK}^3} \quad (29)$$

where

$$PN_{JK} = \mathbf{P}_{JK} \cdot \mathbf{n}_K$$

$$\mathbf{n}_K = \text{the unit normal to panel K}$$

$$AREA_K = \text{the area of panel K (see Subsection 3.1.2)}$$

$$P_{JK} = |\mathbf{P}_{JK}|, \text{ is the distance between the control points, K and J}$$

Equation (29) is the contribution from a point doublet at \mathbf{R}_{CK} with orientation \mathbf{n}_K and is used when $P_{JK} > RFF * (SMP + SMQ)_K$. The quantity, $(SMP + SMQ)_K$, is the "size" of panel K (see Subsection 3.1.2) and RFF is the user-defined, far-field radius factor which has a default value of 5 in the program. This value

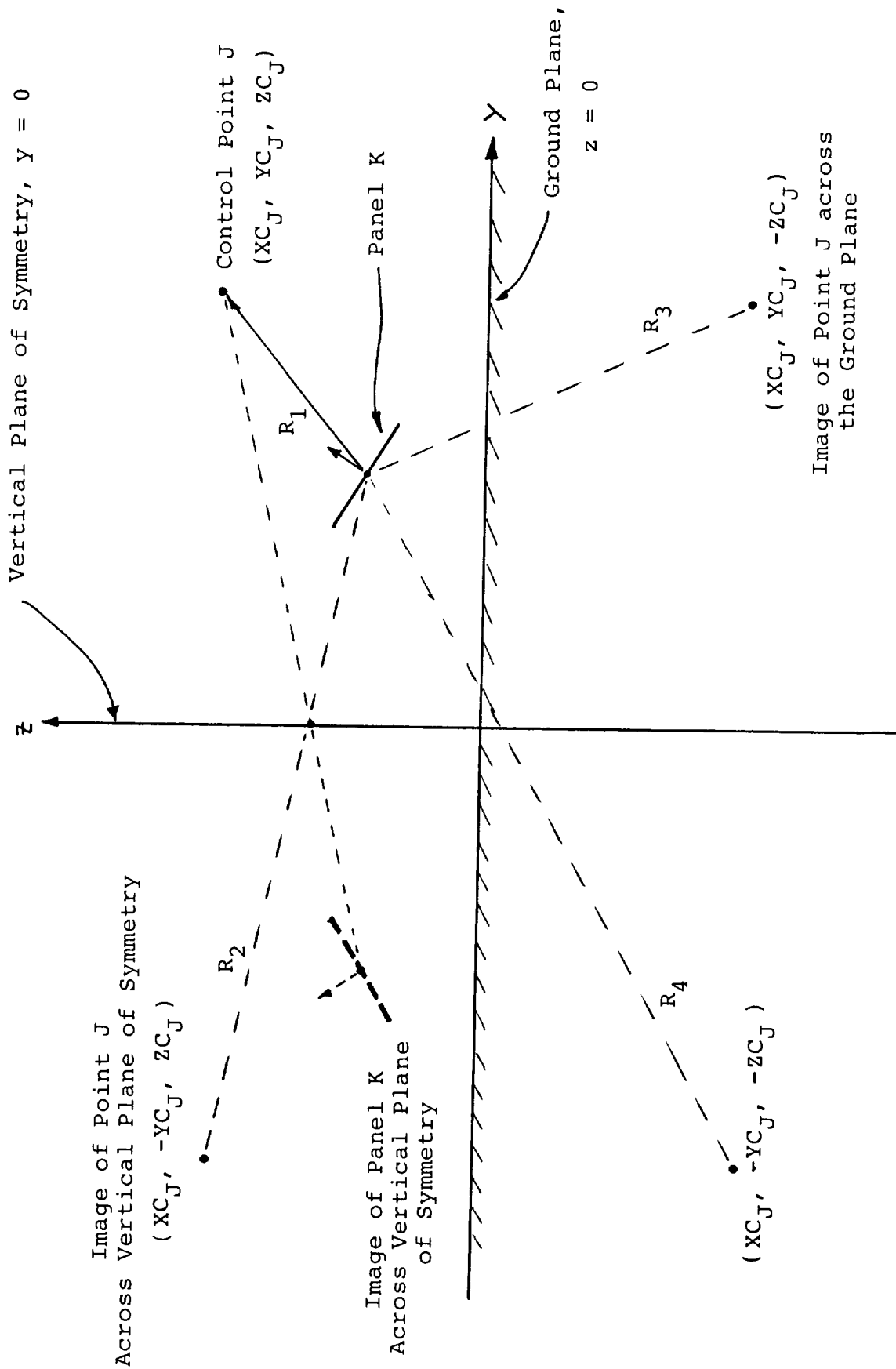


Figure 15. Treatment of Symmetry and Ground-Plane Problems.

was established following initial test cases on a wing and on a wing-body configuration. Use of the expression gives a significant reduction in computing time; however, a user may use the near-field equation (Eq. (25)) throughout the configuration if he wishes simply by giving a very large value for RFF in the input file (1).

3.2.1.2 Source Contribution

The velocity potential influence coefficient for a unit uniform source distribution on the panel, K, is, from Eq. (21),

$$B_{JK} = \iint_{\text{Panel K}} \frac{1}{r} ds$$

The integral is treated for each side of the panel as in the case of the doublet. Thus, for one side

$$B_{JK_i} = \frac{1}{2} \int_{y=y_a}^{y_b} \int_{\xi=0}^{\infty} \left\{ \frac{1}{r_1} - \frac{1}{r_2} \right\} d\xi dy$$

where r_1 , r_2 , y_a , y_b are defined under Eq. (26). This becomes:

$$B_{JK_i} = A1 * GL - PN * C_{JK_i} \quad (30)$$

where

$$GL = \frac{1}{s} \text{LOG} \left| \frac{A + B + s}{A + B - s} \right|$$

and

$$s = |s|$$

$A1$, PN , C_{JK_i} , A and B are defined in Eq. (27). (Note that a second LOG term arises in the above integral but its total contribution from all sides of a closed polygon cancels exactly.)

Again, the total source velocity potential influence coefficient is obtained by summing the contribution from all four sides of the panel; i.e.,

$$B_{JK} = \sum_{i=1}^4 B_{JK_i} \quad (31)$$

Symmetry and/or ground-effect treatment is the same as that described for the doublet contribution.

The expression for B_{JK} for points that are in the far field from panel K is, using a similar approach to that for the doublet (Eq. (29)),

$$B_{JK} = \frac{\text{AREA}_K}{P_{JK}} \quad (32)$$

With the above expressions for C_{JK} , B_{JK} substituted in Eq. (20), the zero internal perturbation formulation is similar to that given by Morino (19), who applied Green's Theorem directly to the external flow.

3.2.2 Velocity Vector Influence Coefficients

3.2.2.1 Doublet Contribution

The velocity induced at control point, J, by a constant doublet distribution of unit value on panel K is, from Eq. (24),

$$V_{\mu_{JK}} = - \int \int_{\text{Panel K}} \nabla_J (\mathbf{n} \cdot \nabla(\frac{1}{r})) dS \quad (33)$$

The kernel is one of the terms resulting from the expansion of a triple vector product. Hence, $\mathbf{V}_{\mu_{JK}}$ can be written

$$\mathbf{V}_{\mu_{JK}} = - \int \int_{\text{Panel K}} \{ (\mathbf{n} \times \nabla_J) \times \nabla(\frac{1}{r}) + \mathbf{n} \nabla_J \cdot \nabla(\frac{1}{r}) \} dS$$

But, $\nabla_J \cdot \nabla(\frac{1}{r}) = 0$.

Hence,

$$\mathbf{v}_{\mu_{JK}} = - \iint_{\text{Panel K}} (\mathbf{n} \times \nabla_J) \times \nabla\left(\frac{1}{r}\right) dS \quad (34)$$

or

$$\mathbf{v}_{\mu_{JK}} = - \oint \nabla\left(\frac{1}{r}\right) \times d\mathbf{r} \quad \text{by Stokes' Theorem.}$$

Thus,

$$\mathbf{v}_{\mu_{JK}} = - \oint \frac{\mathbf{r} \times d\mathbf{r}}{r^3} \quad (35)$$

The integral can be performed along the straight line of each side of the panel, Figure 16. Hence, the contribution from side i is

$$\mathbf{v}_{\mu_{JK_i}} = \frac{\mathbf{a} \times \mathbf{b}}{\mathbf{a} \times \mathbf{b} \cdot \mathbf{a} \times \mathbf{b}} * (\mathbf{A} + \mathbf{B}) * \left(\frac{\mathbf{A} * \mathbf{B} - \mathbf{a} \cdot \mathbf{b}}{\mathbf{A} * \mathbf{B}} \right)$$

This expression is singular when the point, P , is in line with the side ($\mathbf{a} \times \mathbf{b} = 0$). However,

$$\mathbf{a} \times \mathbf{b} \cdot \mathbf{a} \times \mathbf{b} = (\mathbf{A} * \mathbf{B} - \mathbf{a} \cdot \mathbf{b})(\mathbf{A} * \mathbf{B} + \mathbf{a} \cdot \mathbf{b}).$$

And so an alternative expression is

$$\mathbf{v}_{\mu_{JK_i}} = \frac{\mathbf{a} \times \mathbf{b} * (\mathbf{A} + \mathbf{B})}{\mathbf{A} * \mathbf{B} * (\mathbf{A} * \mathbf{B} + \mathbf{a} \cdot \mathbf{b})} \quad (36)$$

This becomes singular only when the point, P , lies on the side. The singularity is avoided by applying a finite-core model on the vortex line. (The core radius can be set by the user (1).)

The total velocity coefficient induced by the unit doublet on the panel is the sum of Eq. (36) over all four sides.

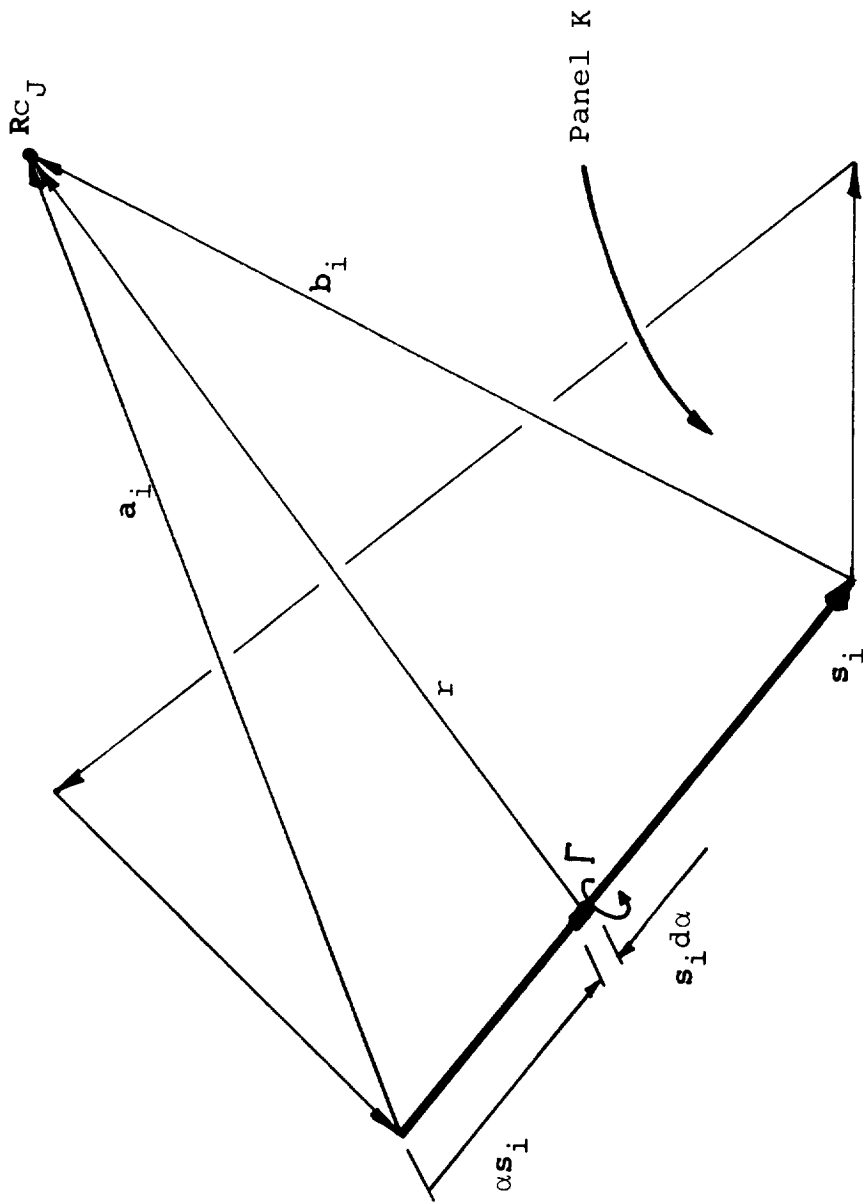


Figure 16. Evaluation of the Line Integral.

$$\mathbf{v}_{\mu_{JK}} = \sum_{i=1}^4 \mathbf{v}_{\mu_{JK_i}} \quad (37)$$

For points in the far-field, the integrand in Eq. (33) is treated directly as a point doublet; i.e.,

$$\mathbf{v}_{\mu_{JK}} = - \nabla_J (\mathbf{n}_K \cdot \nabla \left(\frac{1}{r}\right)) \text{ AREA}_K$$

or

$$\mathbf{v}_{\mu_{JK}} = - \text{AREA}_K * \nabla_J \left(\frac{\mathbf{n}_K \cdot \mathbf{r}}{r^3} \right)$$

Thus,

$$\mathbf{v}_{\mu_{JK}} = \text{AREA}_K * \{3 * \text{PN}_{JK} * \mathbf{P}_{JK} - \text{P}_{JK}^2 * \mathbf{n}_K\} / \text{P}_{JK}^5 \quad (38)$$

The above variables are defined in Eq. (29).

Cases with a vertical plane of symmetry and/or ground effect are treated as before by evaluating the influence of the real panel at each image point rather than vice versa. With this approach the velocity vector contribution must have its component normal to the symmetry plane reversed in sign in order to obtain the actual contribution from the image panel acting on the real control point.

The normal velocity influence coefficient, E_{JK} , in Eq. (23) can now be evaluated; i.e.,

$$E_{JK} = \mathbf{n}_J \cdot \mathbf{v}_{\mu_{JK}}$$

Where the velocity influence, $\mathbf{v}_{\mu_{JK}}$, is taken from either Eq. (37) or Eq. (38) depending on the distance of the point, J, from panel K.

3.2.2.2 Source Contribution

The velocity induced at control point, J, by a constant source distribution on panel K is, from Eq. (24),

$$\mathbf{v}_{\sigma_{JK}} = - \iint_{\text{Panel K}} \nabla_J \left(\frac{1}{r}\right) ds$$

and taking the gradient with respect to the coordinates of point J, this becomes

$$\mathbf{V}_{\sigma JK} = \iint_{\text{Panel K}} \frac{\mathbf{r}}{r^3} dS \quad (39)$$

The integral is treated for each side of the panel as in the case for the velocity potential evaluation. From side i , the contribution is

$$\mathbf{V}_{\sigma JK_i} = GL * (SM * \mathbf{l} - SL * \mathbf{m}) + C_{JK_i} \mathbf{n} \quad (40)$$

Where GL is defined under Eq. (30), and SM , SL and C_{JK_i} are defined under Eq. (27). The total for the panel is the sum over all four sides.

$$\mathbf{V}_{\sigma JK} = \sum_{i=1}^4 \mathbf{V}_{\sigma JK_i} \quad (41)$$

For points in the far field, the panel's source distribution is concentrated in a single source at the panel center. In this case the source velocity coefficient becomes (from Eq. (39))

$$\mathbf{V}_{\sigma JK} = \frac{\text{AREA}_K * \mathbf{P}_{JK}}{P_{JK}^3} \quad (42)$$

The above variables are defined in Eq. (29).

Cases with a vertical plane of symmetry and/or ground effect are treated as before by evaluating the influence of the real panel at each image point rather than vice versa. With this approach the velocity vector contribution must have its component normal to the symmetry plane reversed in sign in order to obtain the actual contribution from the image panel acting on the real control point.

Finally, the normal velocity influence coefficient for the source term in Eq. (23) can be evaluated; i.e.,

$$D_{JK} = \mathbf{n}_J \cdot \mathbf{V}_{\sigma JK}$$

The source velocity coefficient, $\mathbf{V}_{\sigma JK}$, is taken from either Eq. (41) or Eq. (42), depending on the distance of point J from panel K.

3.2.3 Matrix Assembly

The matrix equations, Eq. (20) and (22), can now be formed by assembling the singularity influence coefficients for all the surface and wake panels in the configuration acting at the control point of each surface panel in turn. In the VSAERO program the surface and wake contributions are computed separately: the surface matrix of influence coefficients, once computed, remains fixed throughout the treatment of a configuration while the wake contribution varies with each wake-shape iteration. The wake contribution is, in fact, recomputed and combined with the wake-shedding panel influence coefficients after each wake-shape calculation.

Consider the wake influence in Eq. (20); i.e.,

$$\sum_{L=1}^{N_W} \mu_W C_{JL}$$

Now from the boundary condition imposed on the wake (Eq. (7)) the value for μ_W is constant down each wake column and has the value of the jump in total potential at the start of the column (from Eq. (10)); i.e., for the M^{th} column,

$$\mu_{W_M} = \phi_{KWPU_M} - \phi_{KWPL_M} \quad (43)$$

is constant down the column; $KWPU_M$, $KWPL_M$ are the upper and lower surface panels shedding the M^{th} wake column (Subsection 3.1.4).

Thus,

$$\mu_{W_M} = \mu_{KWPU_M} - \mu_{KWPL_M} + \phi_{\infty KWPU_M} - \phi_{\infty KWPL_M}$$

And the wake influence contribution can be written

$$\sum_{L=1}^{N_W} \mu_W C_{JL} = \sum_{M=1}^{NWCOL} \left\{ \text{PHC}_{JM} * (\mu_{KWPU_M} - \mu_{KWPL_M}) \right. \\ \left. + \text{PHC}_{JM} * (\phi_{\infty KWPU_M} - \phi_{\infty KWPL_M}) \right\} \quad (44)$$

where

$$\text{PHC}_{JM} = \sum_{L=1}^{NWP_M} C_{JL}$$

$NWCOL$ = Total number of wake columns

and

NWP_M = Number of wake panels on the M^{th} column

The result of the summation of the doublet influence coefficient down a column, i.e., PHC_{JM} , is therefore added to and subtracted from the associated upper and lower wake shedding panel influences ($KWPU_M$, $KWPL_M$), respectively.

It is tempting to discard the last term of Eq. (44) because the quantity $(\phi_{\infty KWPU_M} - \phi_{\infty KWPL_M})$ vanishes in the limit as the upper and lower control points on the wake-shedding panels approach the trailing edge in high density paneling. However, with practical panel densities, this quantity will rarely be zero and, in fact, Youngren et al. (20) noticed that a serious error in circulation results if the term is omitted for thick trailing edges. The term is, in fact, readily evaluated and is combined with the source terms to form the known "right-hand side" of the equations.

3.3 Matrix Solver

With the matrix of influence coefficients formed, the solution routine can proceed. VSAERO employs either a direct or an iterative matrix solver depending on the number of unknowns (i.e., number of panels). The direct solver is Purcell's vector method (21) and is used when the number of panels is less than 320. When the number of unknowns is greater than 320, then a "blocked controlled successive under- or over-relaxation" (22) technique is used based on the Gauss-Seidel iterative technique.

The iterative technique proceeds by forming inverses of smaller submatrices centered around the diagonal and by multiplying the residual error vector with the stored inverse of each submatrix. The submatrix blocks are formed automatically within the code on the basis of complete columns of panels. An option is provided for the user to specify his own blocks when the arrangement of patches and panels becomes difficult in awkward geometrical situations. Placing two strongly interacting panels in an order which prevents their inclusion in the same block can lead to poor convergence and sometimes divergence in the blocked Gauss-Seidel routine.

3.4 On-Body Analysis

The matrix solver provides the doublet (i.e., the perturbation velocity potential) value for each surface panel in the configuration. These values and the source values are now associated with the panel center points in the evaluation of the velocity on each panel.

The local velocity is:

$$\mathbf{V} = -\nabla\phi$$

or

$$\mathbf{V} = \mathbf{V}_\infty + \mathbf{v} \quad (45)$$

The perturbation velocity, \mathbf{v} , is evaluated in the panel's local coordinate system; i.e.,

$$\mathbf{v} = V_L\mathbf{l} + V_M\mathbf{m} + V_N\mathbf{n} \quad (46)$$

The normal component is obtained directly from the source form, Eq. (12); i.e.,

$$V_N = 4\pi\sigma \quad (47)$$

The tangential components, V_L , V_M , are evaluated from the gradient of μ , assuming a quadratic doublet distribution over three panels in two directions in turn, Figure 17. Thus, when evaluating the velocity on, say, panel K, the four immediate neighboring panels, N1, N2, N3, N4, are assembled together with

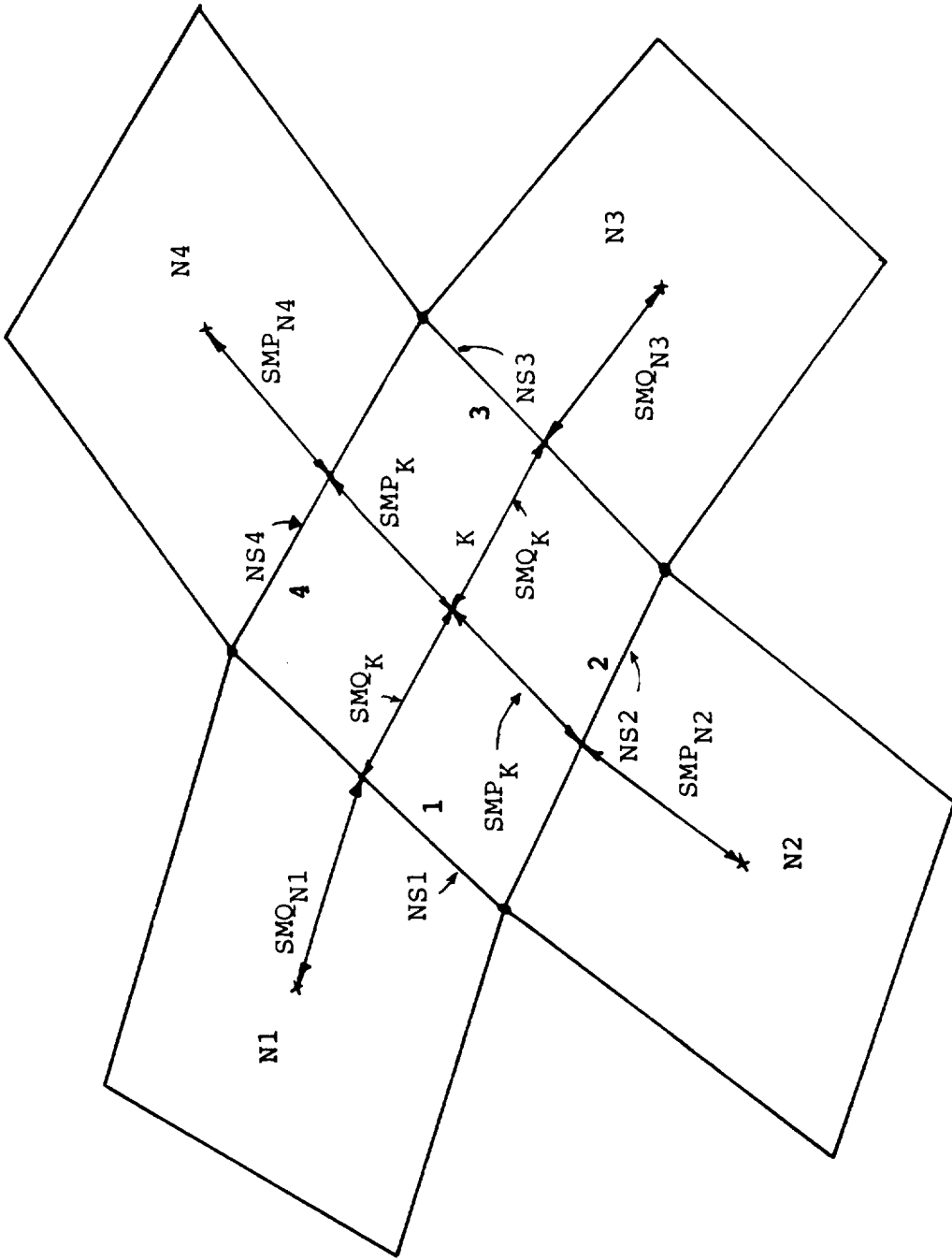


Figure 17. Evaluation of Perturbation Velocity on Panel K (All Neighbors Available and on Same Patch as Panel K).

the neighboring sides of those panels, NS1, NS2, NS3, NS4. This information is obtained directly from stored neighbor information ((NABOR(I,K), NABSID(I,K), I=1,4), K=1,NS), see Subsection 3.1.3. Surface distances are constructed using the SMP, SMQ information for each panel (Subsection 3.1.3), noting that the distance from the center of panel K to the midpoint of either side 1 or side 3 is SMQ_K and, similarly, the distance to the midpoint of either side 2 or side 4 is SMP_K . The additional distance from the midpoint of a side of panel K to the midpoint of the neighboring panel of that side depends on the NABSID value. For example, the additional distance to the neighbor, N1, from side 1 of panel K is SMQ_{N1} if NABSID(1,K) is 1 or 3 and is SMP_{N1} if NABSID(1,K) is 2 or 4; the former is always the case when the neighbor is in the same patch as panel K (Figure 17) and the latter will occur when the neighbor is on a different patch with a different orientation.

Consider the regular case where the neighboring panels are available and are on the same patch as panel K. Then the derivative of the quadratic fit to the doublet distribution in the SMQ direction on panel K can be written

$$DELQ = (DA * SB - DB * SA)/(SB - SA) \quad (48)$$

where

$$SA = - (SMQ_K + SMQ_{N1})$$

$$SB = SMQ_K + SMQ_{N3}$$

$$DA = (\mu_{N1} - \mu_K)/SA$$

$$DB = (\mu_{N3} - \mu_K)/SB$$

A similar expression based on SMP rather than SMQ and using neighbors, N4, N2, instead of N1, N3, gives the gradient DELP in the SMP direction.

DELQ and DELP provide the total gradient of μ and, hence, by resolving into the ℓ and m directions, the perturbation tangential velocity components (Eq. (46)) can be written

$$VL = -4\pi * (SMP * DELP - TM * DELQ)/TL$$

and

$$VM = -4\pi * DELQ \quad (49)$$

The vector, TL, TM, with modulus, SMP, is the center of side 2 relative to the panel center expressed in the local coordinate system of panel K.

The complete set of panel neighbors is not always available for the above derivative operation. Neighbor relationships are cancelled by the program across each wake shedding line to prevent a gradient being evaluated across a potential jump. The program also terminates neighbor relationships between panels when one has a normal velocity specified and the other has the default zero normal velocity. In addition, the user can prevent neighbor relationships being formed across a patch edge simply by setting different ASSEMBLY numbers for the two patches and, finally, the user can actually terminate neighbor relationships on a panel-by-panel basis in the input. This is applied wherever there is a potential jump (e.g., where a wake surface butts up to the fuselage side) or where there is a shape discontinuity in the flow properties (e.g., a sharp edge) or where there is a large mismatch in panel density from one patch to another.

When a panel neighbor is unavailable on one or more sides of a panel, then the doublet gradient routine locates the neighbor of the neighbor on the opposite side to complete a set of three. For example, if neighbor N2 is not available, Figure 18, the neighbor on the opposite side is N4 with adjacent side NS4. Going to the far side of panel N4, i.e., away from panel K, the neighboring panel is NABOR(MS4,N4) with adjacent side NABSID(MS4,N4), where

$$MS4 = NS4 \pm 2; \quad 1 \leq MS4 \leq 4$$

If this panel is available then the set of three is complete, the gradient now being taken at the beginning rather than the middle of the quadratic. If the panel is not available then the program uses simple differencing based on two doublet values. (If no panel neighbors are available, then the program cannot evaluate the tangential perturbation velocity for the panel K.)

With the local velocity known, the pressure coefficient is evaluated on panel K:

$$C_{PK} = 1 - V_K^2 / V_\infty^2 \quad (50)$$

The force coefficient for a configuration or for parts of a configuration are obtained by summing panel contributions. The contribution from panel K is (Figure 19)

$$\frac{\Delta F_K}{q_\infty} = - C_{PK} * AREA_K * n_K + C_{f_K} * AREA_K * t_K \quad (51)$$

where

q_∞ is the reference dynamic pressure

C_{PK} is the pressure coefficient evaluated at the panel center, Eq. (50)

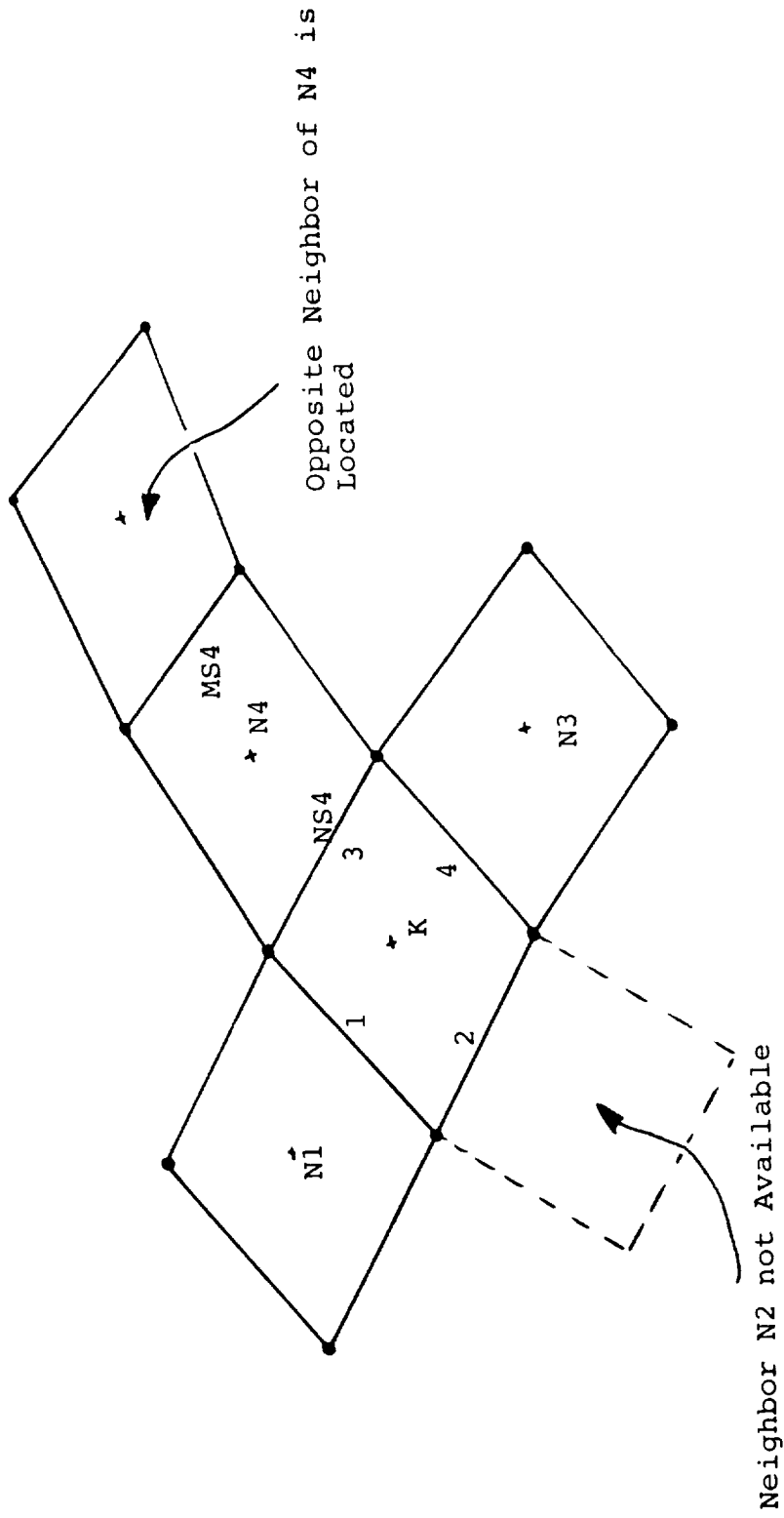


Figure 18. Evaluation of Perturbation Velocity on Panel K when a Neighbor is not Available.

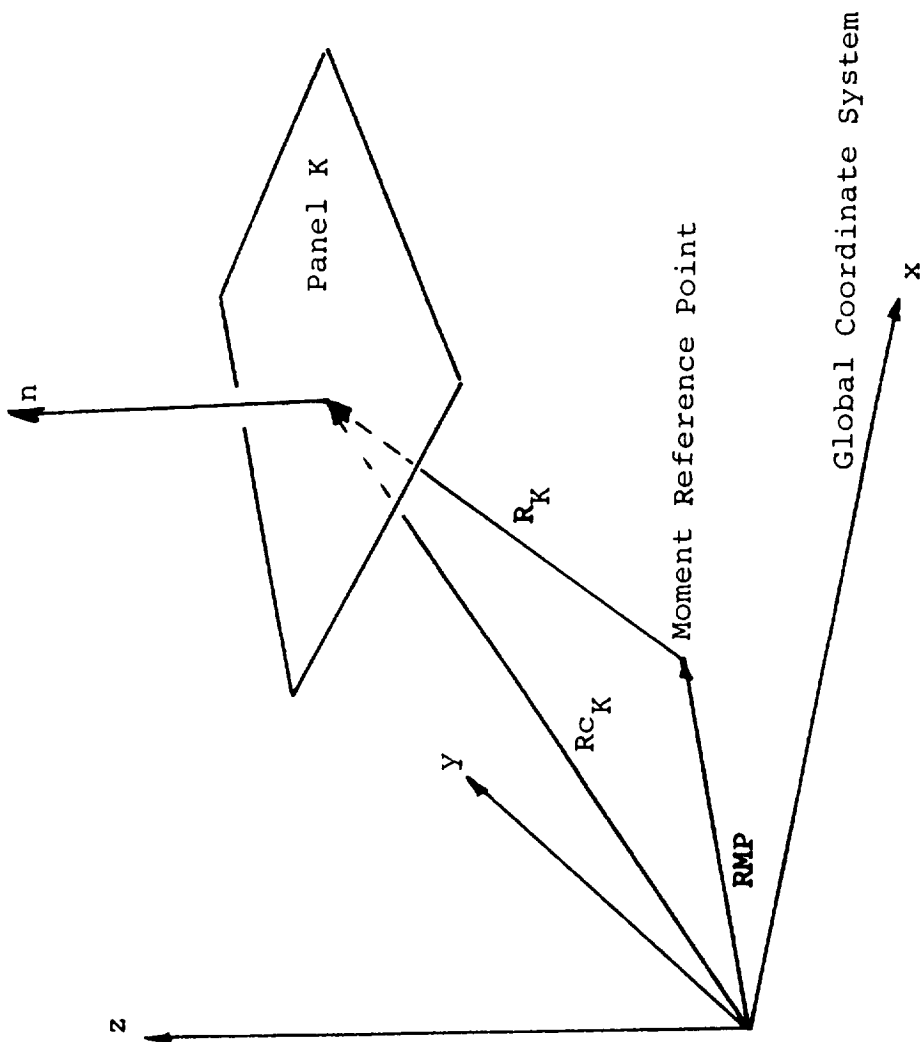


Figure 19. Force Contribution from Panel K.

$AREA_K$ is the panel area projected onto the panel's mean plane

n_K is the unit vector normal to the panel's mean plane

t_K is the unit vector parallel to the panel's mean plane and in the direction of the local (external) velocity; i.e., $t_K = \mathbf{V}_K / |\mathbf{V}_K|$

C_{f_K} is the local skin friction coefficient

The force vector for a patch is then

$$\frac{\mathbf{F}_P}{q_\infty} = \sum_{K=K_1}^{K_2} \frac{\Delta \mathbf{F}_K}{q_\infty} \quad (52)$$

where K_1, K_2 are the first and last panel subscripts in the patch. The force coefficient vector is

$$\mathbf{C}_{F_P} = \mathbf{F}_P / q_\infty S_{REF} = \sum_{K=K_1}^{K_2} \frac{\Delta \mathbf{F}_K}{q_\infty} / S_{REF} \quad (53)$$

where S_{REF} is the reference area specified by the user.

The components of the force coefficient vector are printed out in both wind axes, C_L, C_D, C_S , and body axes, C_X, C_Y, C_Z , (i.e., the global coordinate system), Figure 20.

For symmetrical configurations the total force vector is doubled prior to printout. This means that the printed side force value, i.e., the component normal to the plane of symmetry, is actually twice the side force on one side of the configuration rather than being cancelled to zero for the total configuration.

The skin friction coefficient, C_{f_K} , in Eq. (51) is zero for the first time through the potential flow calculation. During the viscous/potential flow iteration cycle the C_f values are computed along the surface streamlines passing through user-specified points. The program then sets the local C_f value on each panel crossed by a streamline. Panels not crossed by streamlines have C_f values set by interpolation through local panels that have been set, provided these are in the same patch. Patches having no streamlines crossing them are left with zero C_f values on their panels; consequently, it is up to the user to

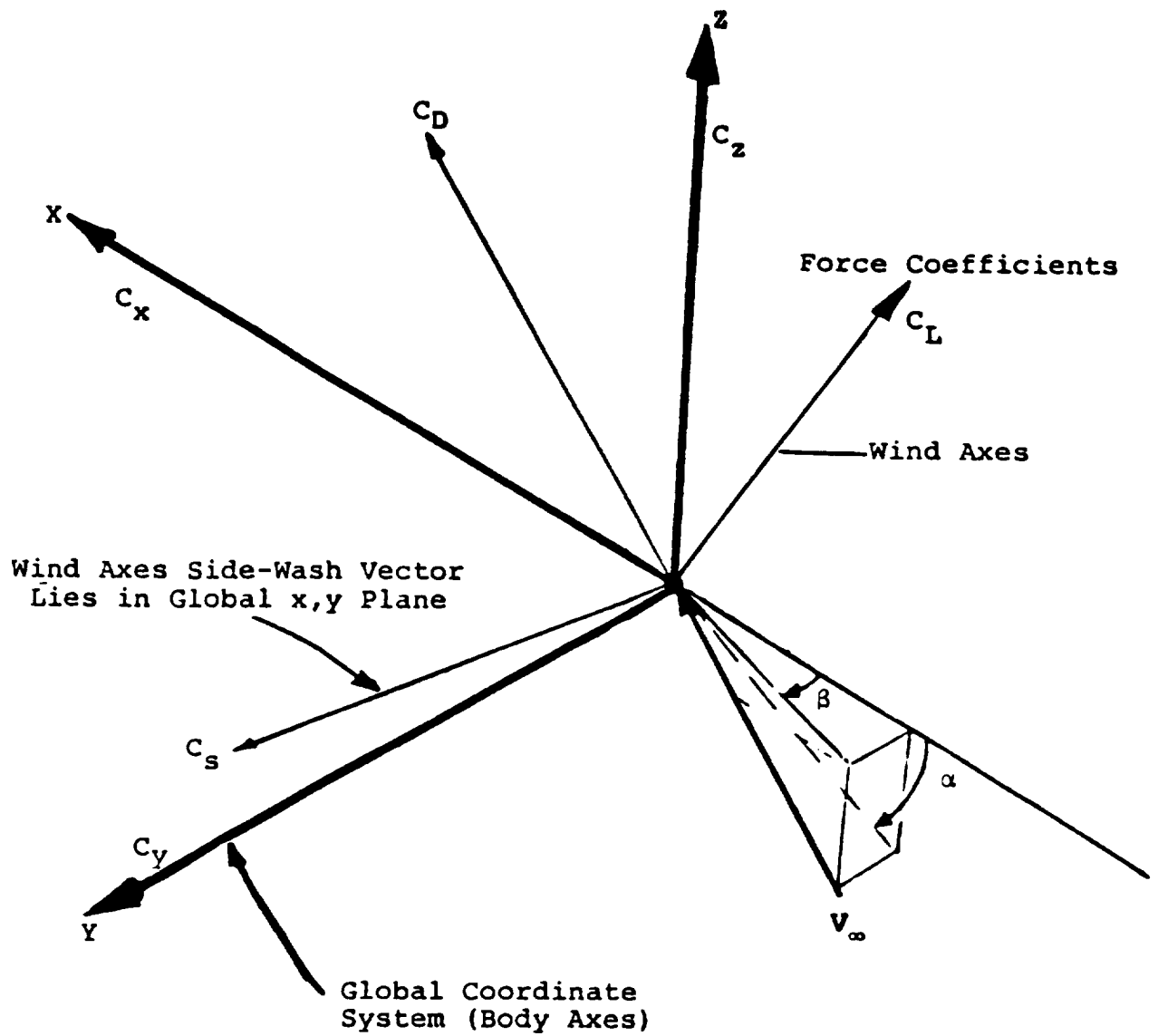


Figure 20. Global and Wind Axis Systems.

adequately cover the regions of interest with streamline requests (1). If a patch is folded (i.e., a wing) and/or there is a dividing stream surface approaching the patch, then streamlines should be requested on both sides of the attachment line.

The contribution to the moment coefficient vector from the K^{th} panel is:

$$\Delta C_{M_K} = \frac{\mathbf{R}_K \times \Delta \mathbf{F}_K}{q_\infty \cdot S_{\text{REF}} \cdot L} \quad (54)$$

where \mathbf{R}_K is the position vector of the control point on the panel, K , relative to the moment reference point; $L = \text{SSPAN}$, the reference semispan for the x and z components of moment (rolling and yawing moments); and $L = \text{CBAR}$ (the reference chord) for the y component of the moment (pitching moment). CBAR and SSPAN are specified by the user (1).

The summation is carried out on the basis of patches, components and assemblies. Summation of the forces and moments acting on user-specified sets of panels can also be obtained.

Patches with $\text{IDENT} = 1$ have an additional output of local force and moment contribution from the summation down each patch. This is useful for "folded" patches representing wing-type surfaces.

Patches with $\text{IDENT} = 3$ include both upper and lower surface velocity and pressure output. On these patches the doublet gradient (Eq. (49)) provides the jump in tangential velocity component between the upper and lower surfaces. The program first computes the mean velocity (i.e., excluding the local panel's contribution) at the panel's center then adds to this one half of the tangential velocity jump for the upper surface and similarly subtracts for the lower surface.

3.5 Wake-Shape Calculation

With the panel singularity values known, the velocity vector can be computed at any point in the flow field using the panel velocity influence coefficients and summing over all surface and wake panels (Eq. (18)). In the wake-shape calculation procedure the velocity vector is computed at each wake panel corner point and each "streamwise" edge; i.e., sides 1 and 3 of a panel, Figure 11, is aligned with the average of its two end velocities.

The wake shape calculation is performed in a marching procedure, starting at an upstream station and progressing through the set of vertical wake-grid planes, Figure 11. In each wake-grid plane the full set of (streamwise) wake lines intersecting that plane is first assembled and the full set of velocities computed at that station. In assembling the set of wake lines for treatment, certain lines can be left out, e.g., lines on wakes identified as rigid by the user (1); individual lines that have been identified as rigid, for example, the line where the wing wake butts up to the fuselage side; and lines that are coincident with other lines that are already in the set.

The step from one wake-grid plane to the next is performed for all lines before another set of velocities is computed. Thus, for a given set of points, $RW_{i,M}$; $i=1, NL_M$, in the M^{th} wake-grid plane, the set of points in the next wake-grid plane is:

$$RW_{i,M+1}^j = RW_{i,M}^J + \bar{V}_i^j * DX / |\bar{V}_{x_i}^j|; i=1, NL_M \quad (55)$$

where NL_M is the number of wake lines being moved in the M^{th} wake-grid plane; \bar{V}_i^j is the mean velocity across the interval for the i^{th} line in the j^{th} predictor/corrector cycle.

$$\bar{V}_i^j = \left(v_{i,M}^J + v_{i,M+1}^{j-1} \right) / 2 \quad (56)$$

J is the total number of predictor/corrector cycles in use (default is 2).

$v_{i,M+1}^0$ is set of $v_{i,M}^J$, and $v_{i,M+1}^{j-1}$ is computed at the point, $RW_{i,M+1}$.

In each predictor/corrector cycle the complete set of points in each wake-grid plane are moved and the current movement vector

$$d_i = RW_{i,M}^j - RW_{i,M}^{j-1}$$

is applied to all the points downstream on each line, before the next set of velocities is computed. A limiting movement can be applied as a damper in difficult situations.

When all the wake-grid planes have been processed, the wake panel parameters are reformed using the new corner points. The modified set of influence coefficients can then be computed for the next solution.

3.6 Boundary Layer Analysis

The solution from the on-body analysis (Subsection 3.4) can be transferred to the boundary layer analysis. Two integral boundary layer analyses are provided in the VSAERO program: the first method, which is described in Reference 23, provides the boundary layer characteristics along computed (external) surface streamlines. The location of a point (panel) on each streamline is provided by the user who is, therefore, responsible for ensuring that a family of streamlines adequately covers the regions of interest. The method, which is applicable for wings and bodies, includes the effects of surface curvature and streamline convergence/divergence under the assumption of local axisymmetric flow. The surface streamline tracking procedure is described in (8) and (24) and is based on a second-order surface stream function formulation. The streamline boundary layer calculation can be expected to break down in regions of large cross flow. However, the procedure has given surprisingly good guidance for the onset of separation for a wide range of practical problems.

The second method, which is installed in the VSAERO program and which is described in Reference 2, includes a cross-flow model. This method is an infinite swept wing code and is applied in a strip-by-strip basis across wing surfaces, with the user specifying which strips are to be analyzed.

The boundary layer module is fully coupled with the VSAERO inviscid code in an outer viscous/potential iteration loop, Figure 3. In further iterations, the displacement effect of the boundary layer is modelled in the potential flow calculation using the source transpiration technique; i.e., the boundary layer displacement term appears in the external Neumann boundary condition equation as a local non-zero normal velocity component (Eq. (12)), and is thereby related directly to source singularities in this formulation. The boundary layer calculation also provides a separation point on each streamline, thereby defining a boundary of separation for a family of streamlines. The criterion for separation is currently a vanishingly small skin friction coefficient (in the direction of the external streamline).

3.7 Off-Body Analyses

When the iterative loops for the effects of wake shape and boundary layer are complete, the VSAERO program offers options for field velocity surveys and off-body streamline tracking. These options, which are discussed separately below, both use the off-body velocity calculation, Eq. (18), based on a summation of the contributions from all surface and wake panels added to the onset flow.

3.7.1 Velocity Survey

Off-body velocity calculations are performed at user selected points. Normally, the points are assembled along straight scan lines. These lines in turn may be assembled in planes and the planes in volumes. The shape of the scan volume is determined by the parameter, MOLD. Two options are currently available (1).

MOLD=1 Allows a single point, points along a straight line, straight lines within a parallelogram or within a parallelepiped.

MOLD=2 Allows points along radial lines in a cylindrical volume.

A number of scan boxes can be specified, one after the other. A MOLD=0 value terminates the off-body velocity scan.

The location of scan lines within the scan boxes can be controlled in the input. The default option is equal spacing generated along the sides of the box. The location of points along a scan line can be controlled also in the input, but again, the default option is equal spacing.

If a scan line intersects the surface of the configuration, an intersection routine locates the points of entry and exit through the surface paneling. The scan line points nearest to each intersection are then moved to coincide with the surface. Points falling within the configuration volume are identified by the routine to avoid unnecessary velocity computations. These points are flagged in the printout. The input parameter, MEET, controls the calls to the intersection routine: MEET=0 (default) makes the routine active, while MEET=1 switches it off; clearly, if the selected velocity scan volume is known to be outside the configuration volume, then there is no need for the program to compute where the scan lines intersect the configuration surface.

The velocity routine, VEL, computes the velocity vector at each point by summing the contributions from all surface panels, wake panels, image panels (if present), onset flow, etc. The

routine includes near-field procedures for dealing with points that are close to the surface panels or wake panels. The near-field routine involves a lot of extra computation; if, therefore, it is known that a scan box is well clear of the configuration surface and wake then it is worthwhile turning off the near-field routine to avoid unnecessary computation. This is controlled by the input parameter, NEAR; NEAR=0 (default) keeps the near-field routine active while NEAR=1 switches it off.

3.7.2 Off-Body Streamline Procedure

The numerical procedure for calculating streamline paths is based on finite intervals, with a mean velocity vector being calculated in the middle of each interval, Figure 21. The velocity calculation point, RP , is obtained by extrapolation from the two previous intervals on the basis of constant rate of change in the velocity vector direction; i.e.,

$$RP = R_n + .5 s_n t \quad (57)$$

where R_n is the previous point calculated on the streamline, s_n is the present interval length, and t is a projected tangent vector.

$$t = \left(\frac{s_n + s_{n-1}}{s_{n-2} + s_{n-1}} \right) (t_{n-1} - t_{n-2}) + t_{n-1} \quad (58)$$

where $t_{n-1} = \frac{V_{n-1}}{|V_{n-1}|}$, etc. V_{n-1} is the velocity calculated in the middle of the previous interval.

RP does not necessarily lie on the streamline path. The calculated velocity, V_n , at RP , is used to evaluate the next point on the streamline; i.e.,

$$R_{n+1} = R_n + \frac{s_n V_n}{|V_n|} \quad (59)$$

An automatic procedure is included in the routine which changes the interval length, s_n , in accordance with the change in tangent direction. If a large change in direction is calculated, the value of s_n is decreased and the calculation is repeated until the change in direction is within a specified amount. If the change in direction is smaller than a certain amount, then the interval length for the next step is increased.

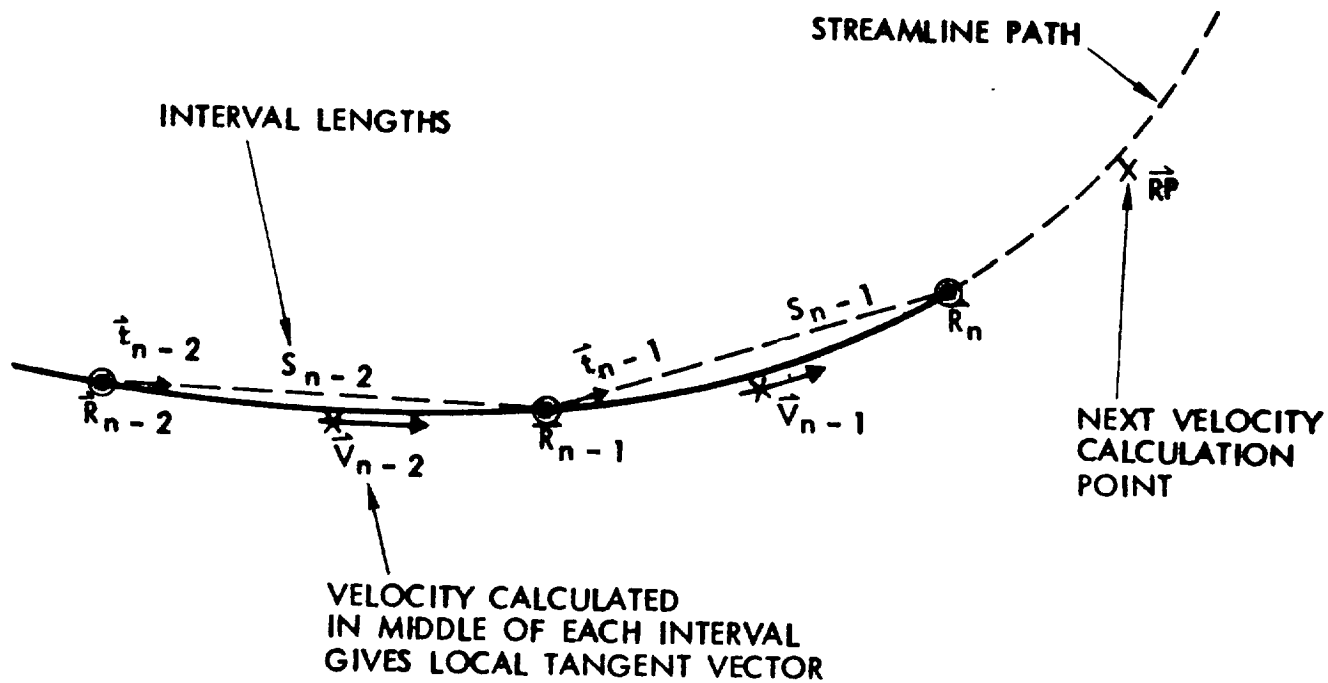


Figure 21. Streamline Calculation.

4.0 DISCUSSION OF RESULTS

Correlation studies discussed below include exact and nominally exact solutions of a number of basic test cases, some of which had proved difficult for earlier low-order panel methods. In addition, some comparisons are made between calculated and experimental data.

4.1 Swept Wing

Figure 22 shows the chordwise pressure distribution at $\eta = 0.549$ on a thin, swept wing at 5° incidence. The wing has a mid-chord sweep of 30° , aspect ratio 6, taper ratio $1/3$, and a NACA 0002 section. A nominally exact datum solution (25) for the case was computed by Roberts' third-order method using a 39 (chordwise) by 13 (spanwise) set of panels. The present calculations, based on the $\phi_i = 0$ formulation, use 10 spanwise panels with both 80 and 20 chordwise panels on a "cosine" spacing, giving increased panel density towards leading and trailing edges. Roberts' datum paneling is heavily weighted towards the leading edge: he has, in fact, 4 more panels ahead of the most forward panels in the present 80 cosine spacing case.

The comparison in Figure 22 indicates that the low- and high-order methods give essentially the same solution where the control point density is the same. The present calculations using 20 panels chordwise deviate from the datum solution near the leading and trailing edges where the control point densities are different. Good agreement is restored in those regions by the 80-panel case which, at the trailing edge at least, has a similar panel density to the datum case. (Note: not all the 80-panel pressure values are plotted in the central region of the chord in Figure 22.)

4.2 Wing with Strake

The fact that surface velocities are obtained by numerical differentiation in the present method might lead to inaccuracies in awkward situations. So far, no serious trouble has been experienced. Any problem that might arise with the derivative scheme (e.g., in a region of mismatched paneling) can usually be alleviated by cutting panel neighbor relationships at that station, thus forcing a forward or backward differencing (Subsection 3.4). One situation that could be difficult and which has caused a problem for other methods is the evaluation of the spanwise velocity component, V_y , in the neighborhood of the kink on a wing with strake. In the case considered in Reference 25, the leading-edge kink occurs at 25% of the semispan and the leading-edge sweep is 75° inboard and 35° outboard. The trailing-edge sweep is 9° . Again, the wing section is a NACA 0002 and incidence 5° .

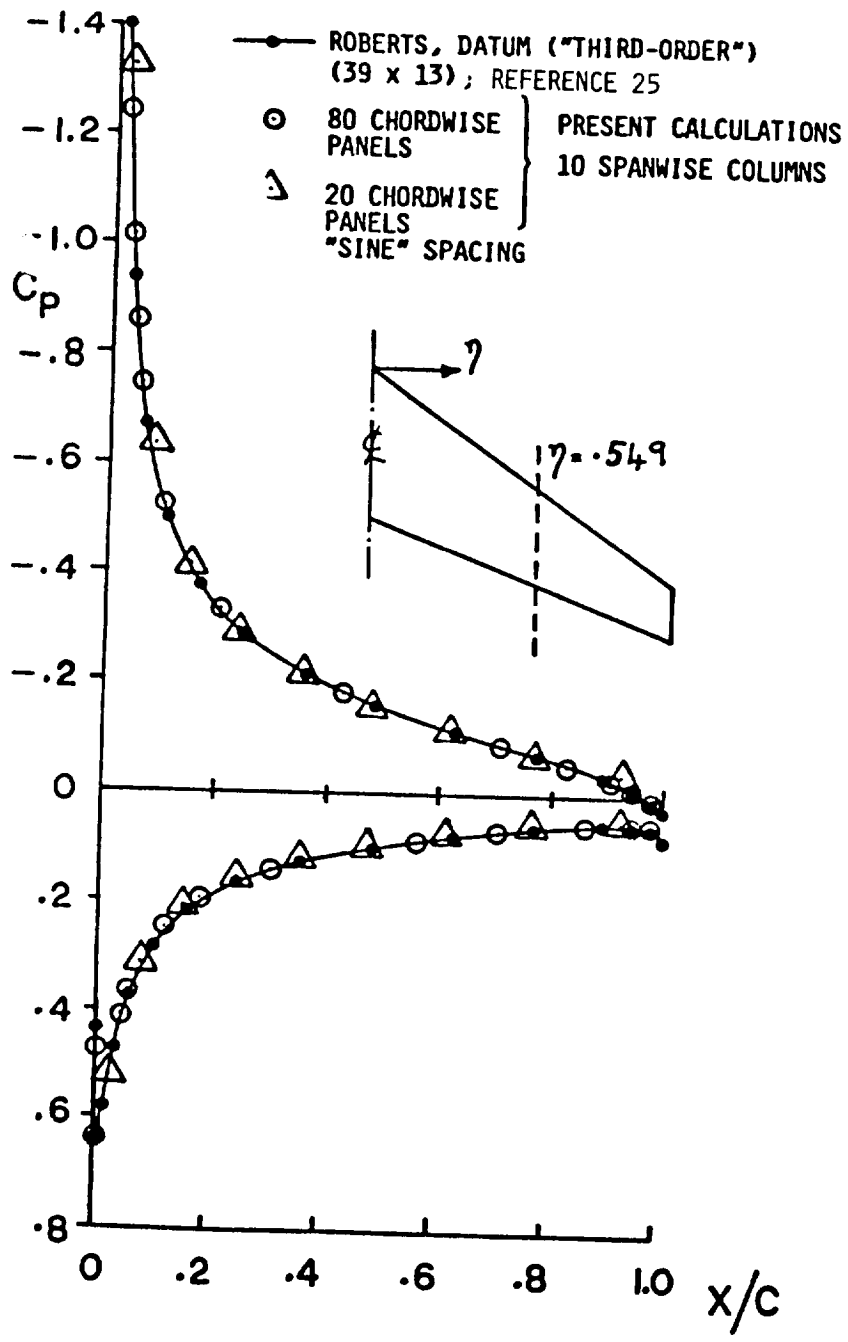


Figure 22. Comparison of Calculated Chordwise Pressure Distributions on a Thin Swept Wing. NACA 0002 Section; $\alpha = 5^\circ$.

The chordwise distribution of V_y is plotted in Figure 23 at stations $\eta = .219$ and $.280$; i.e., just inboard and just outboard of the kink, respectively.

Two higher-order datum solutions are plotted (25) from Roberts' third-order method and from Johnson and Rubbert's (17) second-order method. These datum solutions agree on the outboard distribution but disagree by a small amount on the inboard cut. The disagreement might be caused by the different ways the interpolation is set up across the kink.

The present calculations are in close agreement with the datum solutions and favor the second-order solution near the upstream part of the inboard cut. The case was run as part of a "shakedown" exercise of the code and used 946 panels in a 44 (chordwise) by 20 (spanwise) array with 66 panels on the tip-edge surface. The chordwise paneling was on a "sine" distribution with density increasing towards the leading edge. Such a high number of panels was probably not needed for this case, but the calculation took approximately $2\frac{1}{2}$ minutes on a CDC 7600.

4.3 Nacelles

In the past, low-order solutions for internal flows have suffered badly from "leakage" problems in between control points. The present code was, therefore, applied to two nacelle cases. The first of these is a simple through-flow nacelle formed by rotating a NACA 0010 about the nacelle axis such that the minimum area is one fourth of the inlet and exit areas, Figure 24. This example, taken from Reference 18, shows how the earlier, first generation, low-order analysis, because of the leakage, cannot match the internal flow calculated by the higher-order methods. However, the low-order, VSAERO solution (with the internal potential set to zero) is in close agreement with the high-order solutions and evidently does not have this leakage problem.

The second nacelle case considered is also an open nacelle, but with an exit diameter 0.3 of the chord. The nacelle surface is generated by a NACA 0005 section tilted leading edge out by 5° from the x-axis.

Two higher-order datum solutions (25) are shown in Figure 25. for the chordwise pressure distribution. These are due to Hess and also Roberts.

Roberts' solution shows a slightly lower pressure inside the duct compared with Hess's solution. The present calculations, based on the $\phi_i = \phi_\infty$ formulation, use 10 panel intervals around half the circumference and with two chordwise distributions, 26 cosine and 48 sine, around the complete section. Both results are in very close agreement with the datum solutions with a tendency for slightly lower pressure inside the duct compared with Hess's solution. This could be caused by the slightly

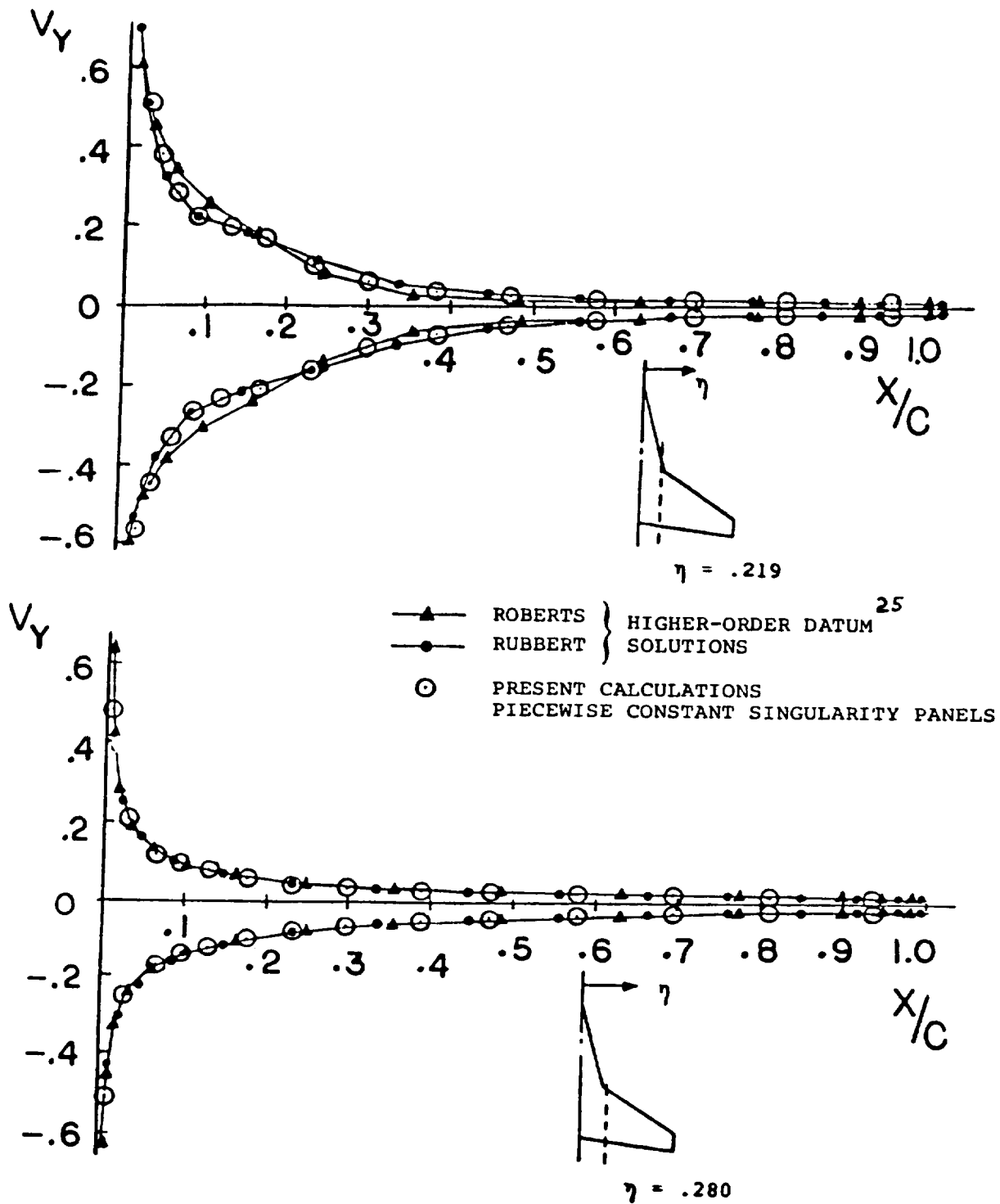


Figure 23. Comparison of Calculated y Component of Velocity at Two Stations on a Wing with Strake. NACA 0002 Section; $\alpha = 5^\circ$.

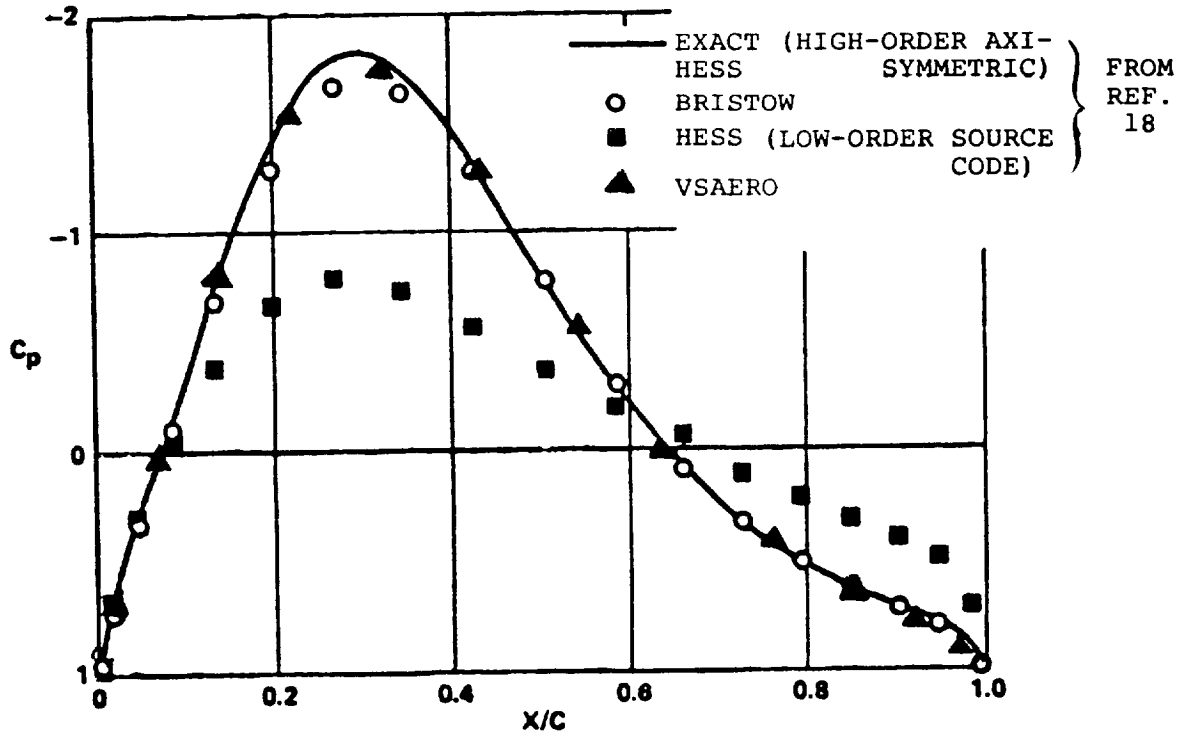
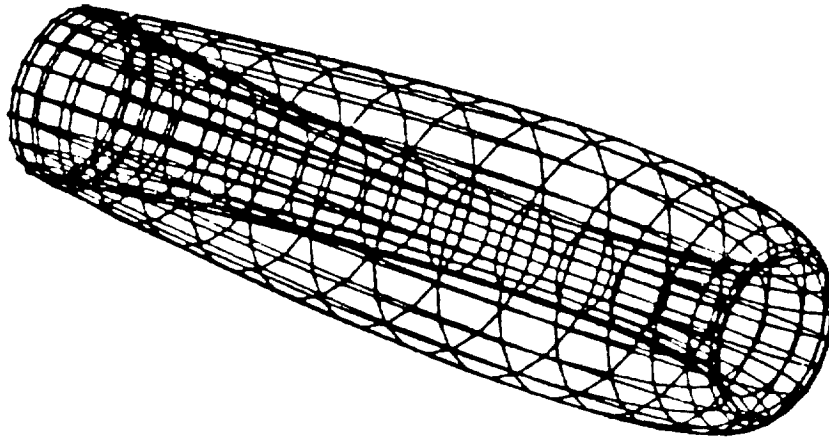


Figure 24. Comparison of Internal Pressure Calculated using a Range of Methods Showing Leakage of Low-Order First Generation Model.

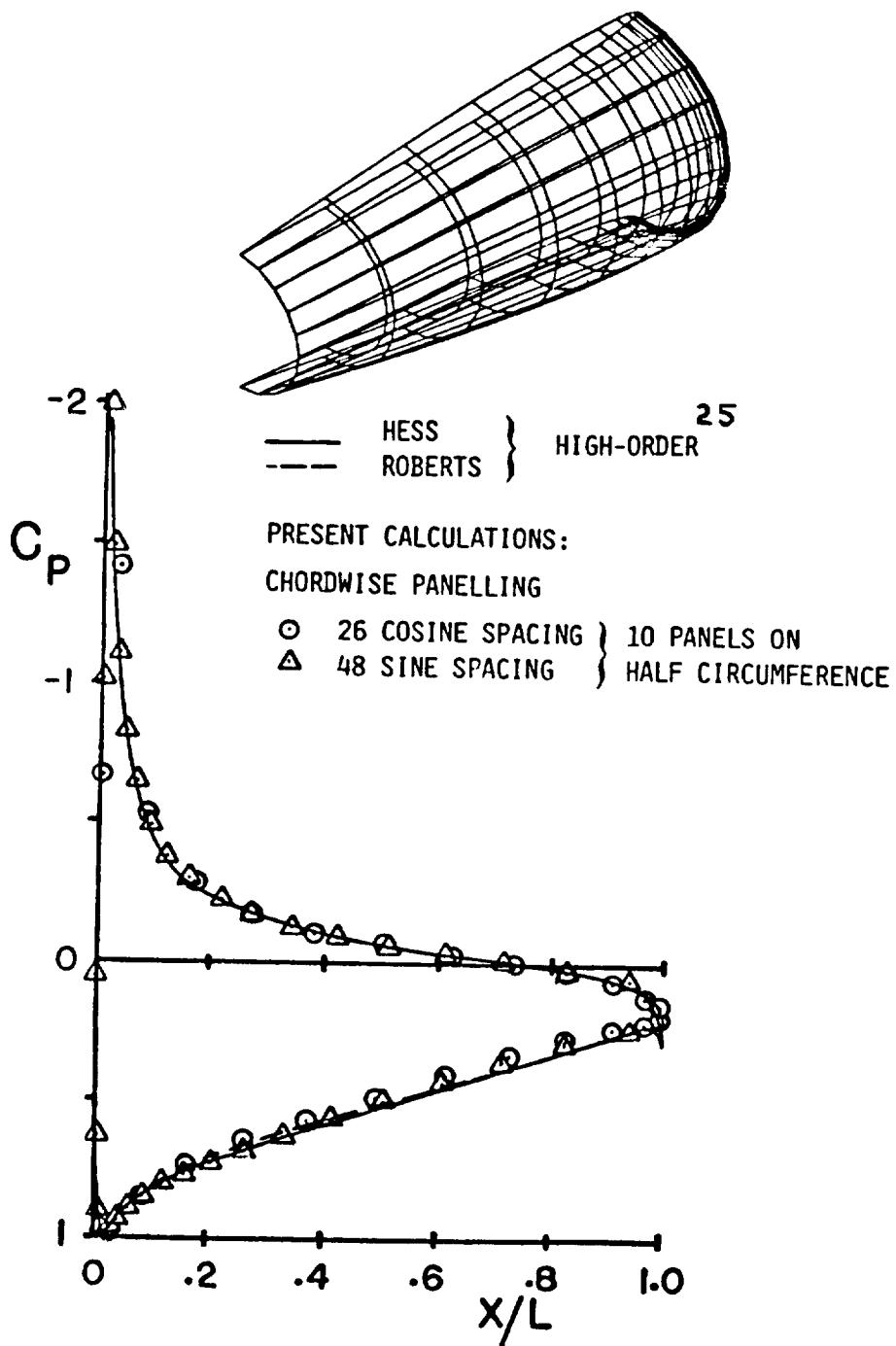


Figure 25. Comparison of Calculated Pressure Distributions on a Nacelle with Exit Diameter/Chord .3. NACA 0005 Section; $\alpha = 0^\circ$.

smaller duct cross-section area generated by the present 10 flat panel representation. Again, there is no leakage problem with this formulation.

4.4 Wing-Flap Cases

Cases with slotted flaps have proven troublesome for some earlier, low-order panel methods, especially those using a specified doublet or vorticity singularity distribution and employing "Kutta points" where tangential flow is specified just downstream of the trailing edges (e.g., (23)). In closely interacting multi-element configurations the interference of the downstream element acting on the "Kutta point" of the upstream element can result in a circulation error; in addition, the solution can be sensitive to the shape of the prescribed loading distribution on the upstream element--this is quite different from that on the regular single-element wing section.

Two wing-flap cases are considered below for the VSAERO program. The first case is one of the exact two-dimensional, two-element cases provided by Williams (26). Figure 26 shows the close agreement between the VSAERO calculations and the exact solution for configuration B on both the main element, Figure 26(a) and the flap, Figure 26(b). Part of the high aspect ratio paneling in the VSAERO calculation is shown in Figure 26(c), and has 110 panels chordwise on the main and 60 on the flap.

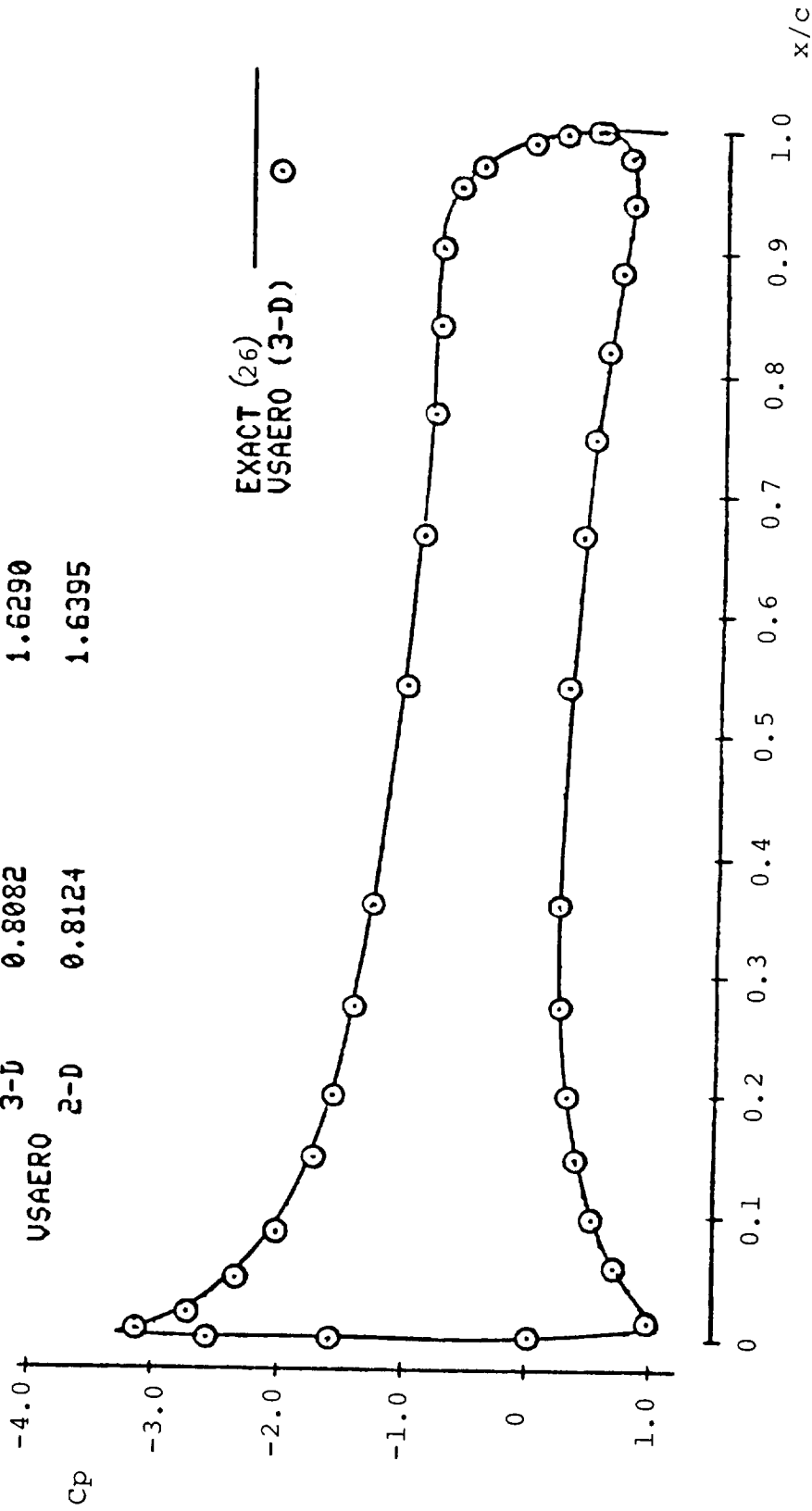
The second wing-flap case involves a part-span flap. The inset in Figure 27 shows a general view of a wing-flap configuration at 16° incidence. The wake shape is shown after one iteration cycle. The wing has an aspect ratio of 6 and the basic section is a NACA 0012. The 30% chord Fowler flap is deflected 30° and the flap cutout extends to $\eta = .59$ on the semispan. The surfaces of the wing tip edge, the flap edge and the end of the cove are covered with panels.

Vortex separations were prescribed along the wing tip edge and the flap edge. The present calculations of surface pressures are compared with experimental data (27) at two stations in Figure 27. A section through the flap at $\eta = .33$ is shown in Figure 27(a) and one just outboard of the flap edge at $\eta = .6$ in Figure 27(b).

Boundary layer calculations have not been included in this calculation yet, and so the agreement between the results at this incidence (16°) is probably too close. The lower peak suction in the flap data, Figure 27(a), may be caused by interference from a nearby flap support wake.

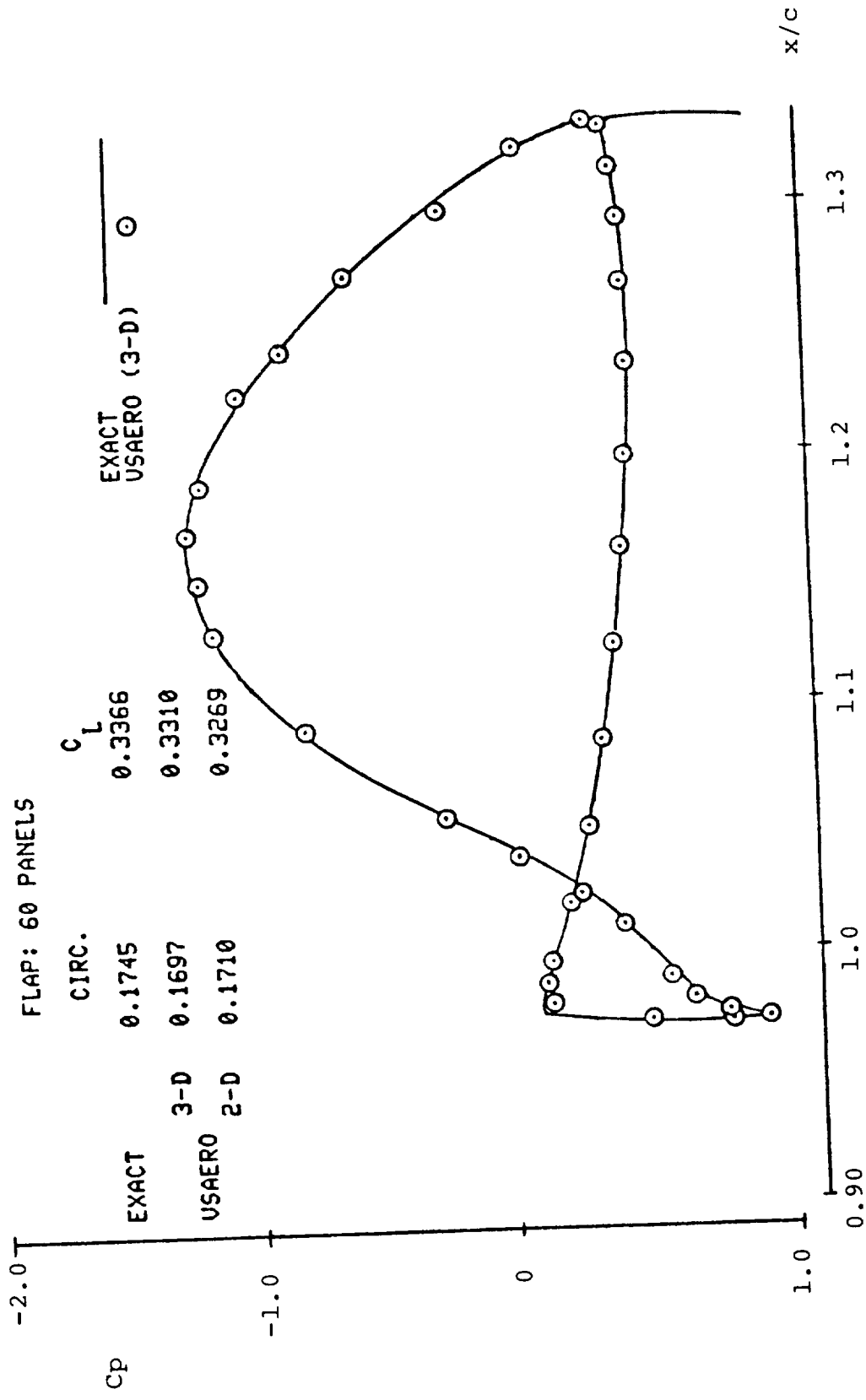
MAIN ELEMENT: 110 PANELS

EXACT	3-D	USAERO	2-D	CIRC.	C_L
0.8400		0.8082			1.6915
		1.6290			1.6290
		0.8124			1.6395

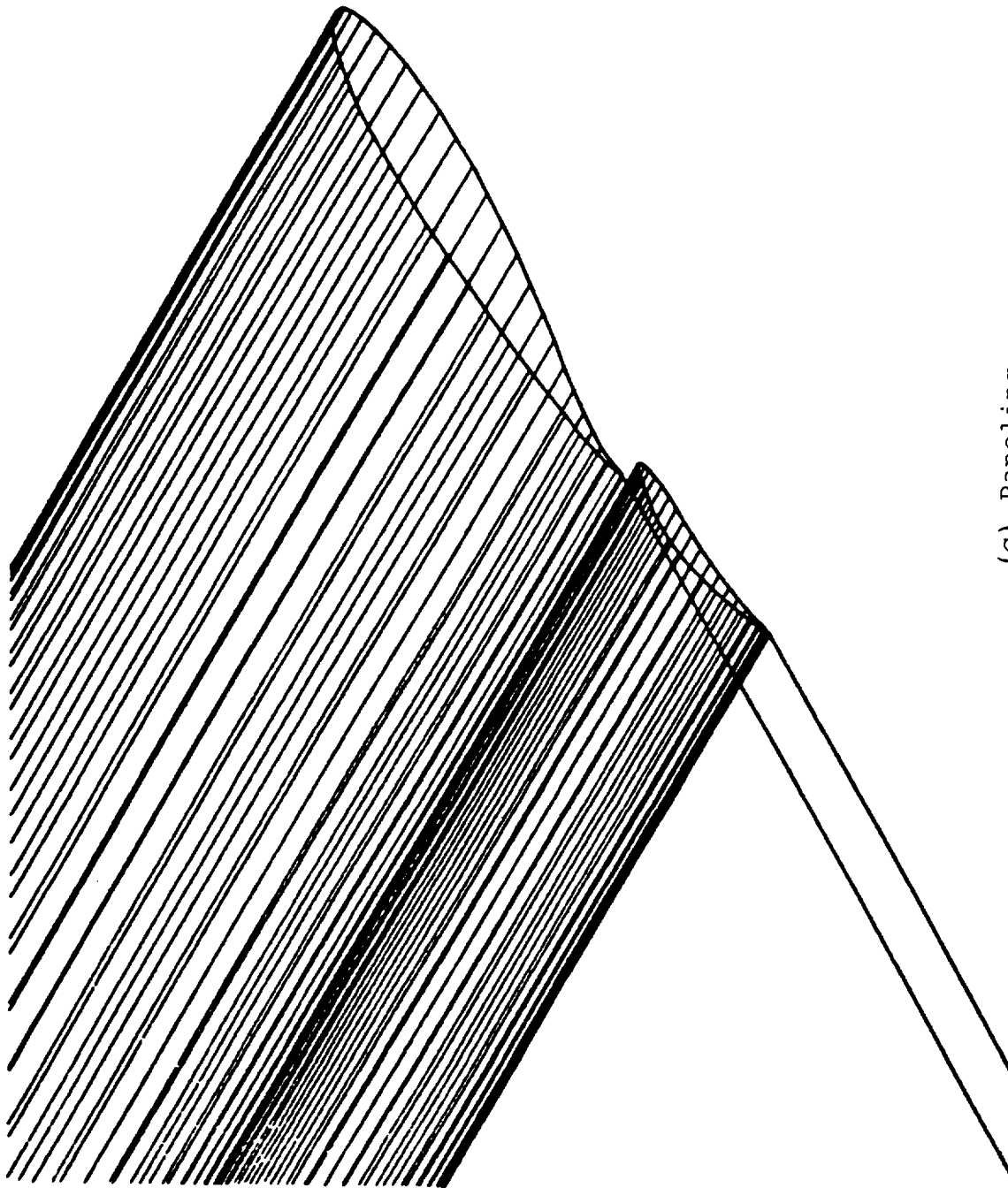


(a) Main Element

Figure 26. Comparison of VSAERO Calculation with Exact Solution for Williams (26) Two-Element Case B.

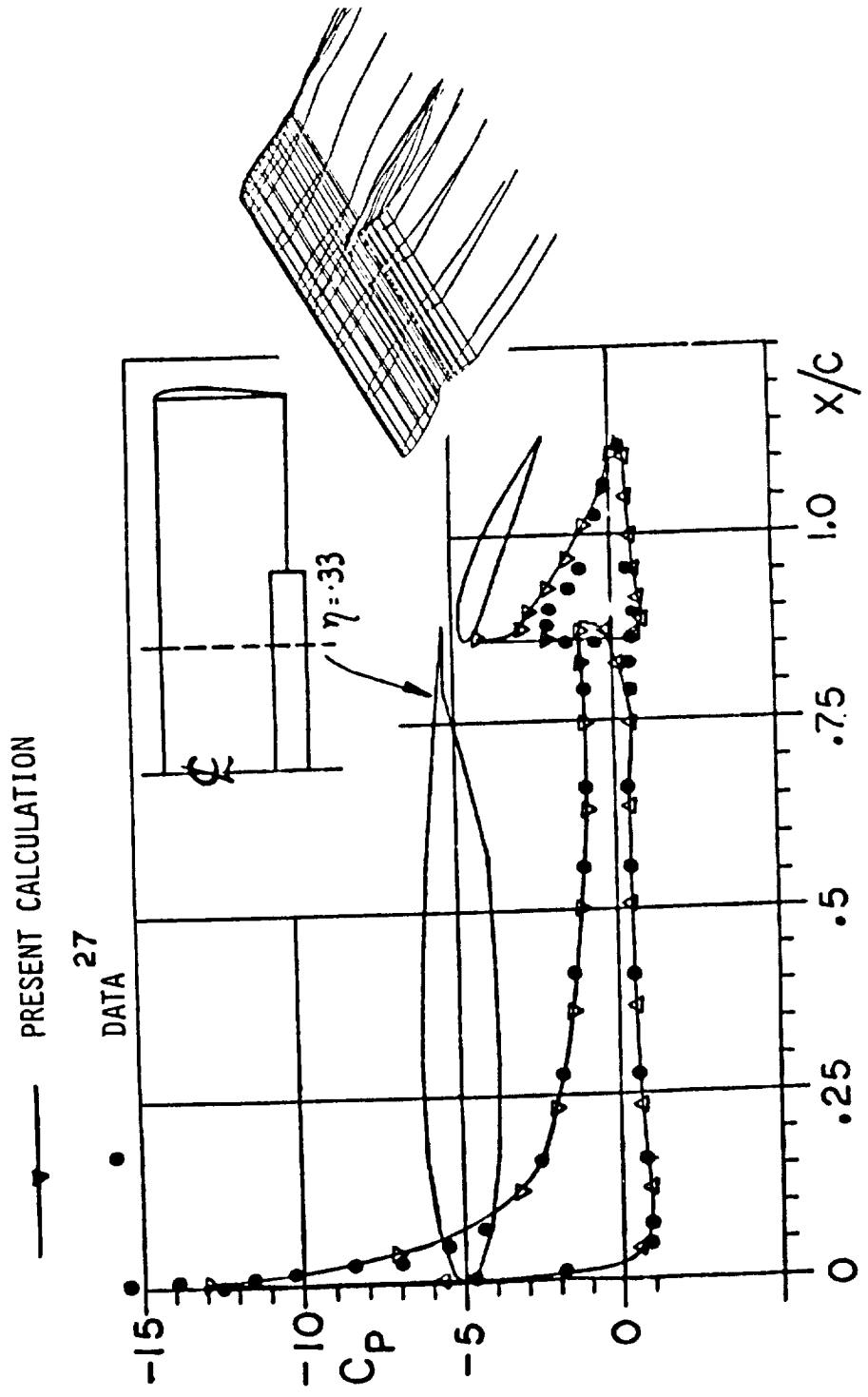


(b) Flap
Figure 26. Continued.



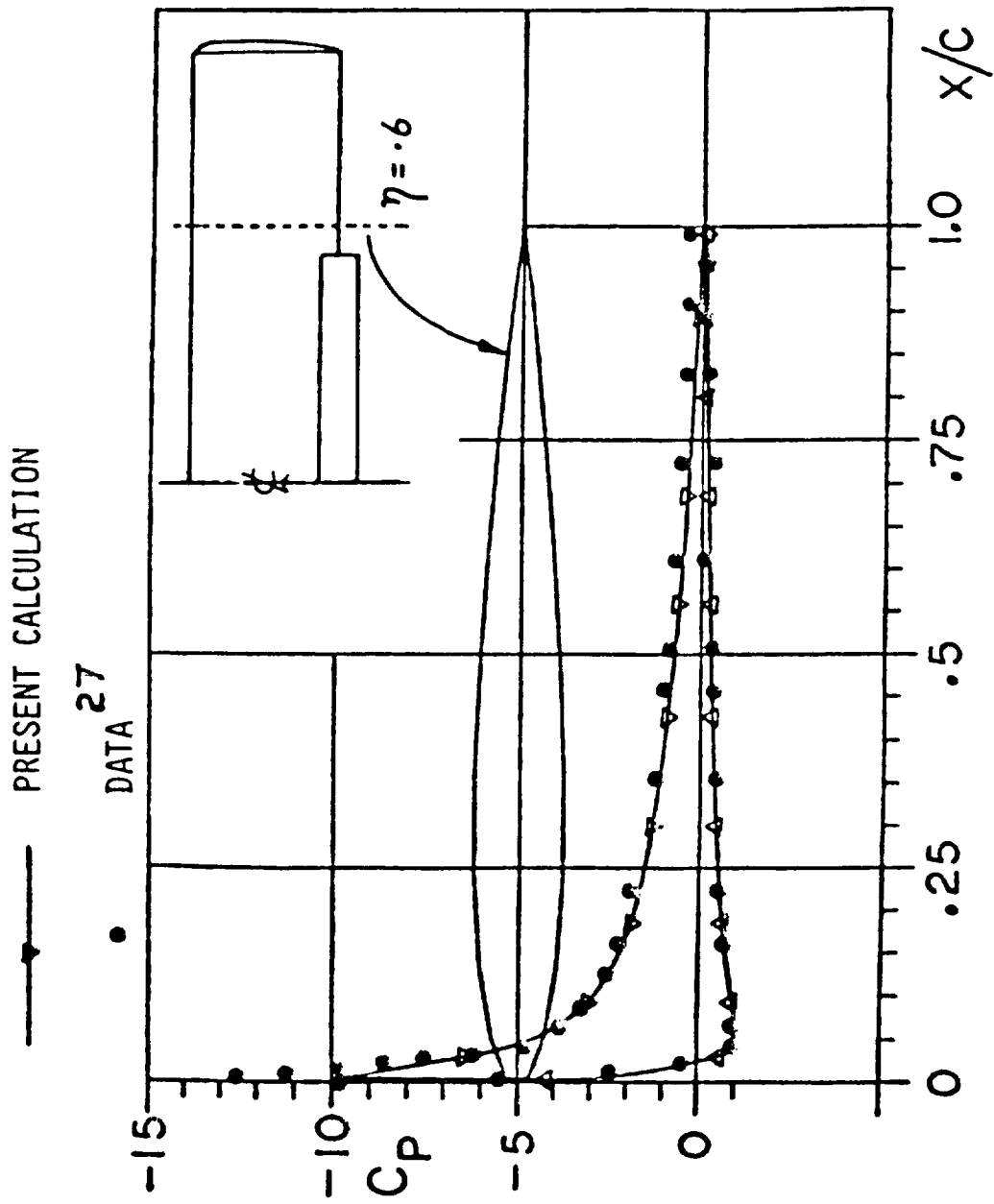
(c) Paneling

Figure 26. Concluded.



(a) Section at $\eta = .33$

Figure 27. Comparison of Pressure Distributions on an Aspect Ratio 6 Wing with Part-Span Fowler Flap; $\alpha = 16^\circ$.



(b) Section at $\eta = .6$

Figure 27. Concluded.

4.5 Body Alone

The case of 4:1 spheroid at 5° angle of attack was run to test the prediction accuracy of body cases. Figure 28 shows the very good agreement between the VSAERO prediction and the exact (non-lifting) solution. The calculation has 10 panels around the half-body and 20 longitudinally, with the case being run with the vertical plane of symmetry. Small discrepancies in the $C_p \sim Z$ plot are probably partly due to the control points being on the inscribed polygon (i.e., a plot of $C_p \sim \theta$ would look better, but the $C_p \sim Z$ plot is more practical for the general case.

4.6 Wing-Body Cases

Concave corners have posed a problem to some low-order methods in the past, making it necessary to use high panel densities. Also, such a region might cause a numerical differentiation scheme to misbehave. Two wing-body cases are considered here. Figure 29(a) shows a longitudinal cut through a pressure distribution on a wing-body case from Reference 28 for $\alpha = 4^\circ$. The cut passes just above the wing-body junction. The present calculations compare well with other solutions and are in good agreement with experimental results.

A spanwise cut through the present calculations at $X/L = .48$ is shown in Figure 29(b) together with the surface geometry shape. The pressure distribution passes smoothly from the body surface onto the wing surface even though relatively large panels are present on the fuselage side (only 6 around the half section).

In this calculation the wing and body form one complete volume in which $\phi_i = \phi_\infty$.

The second wing-body case is the Swearingen Metroliner wind tunnel model. Figure 30 shows the VSAERO paneling and it will be noticed that there has been no treatment of the intersection region; i.e., the wing and fuselage panel models are from separate wing-alone and body-alone runs. This is not a recommended practice; however, it is interesting to observe that--at least in the present configuration--the results are good and compare very well with experimental data right into the junction region. (Note that the doublet gradient procedure has not used panel information that falls inside the fuselage or wing.)

Comparisons between experimental (29) and calculated pressure distributions are made in Figure 31, 32 and 33 at two spanwise stations, $y = 9.0$ ($y/b/2 = .22$) and $y = 18.0$ ($y/b/2 = .43$). The location of the body side is at $y = 5.0$ ($y/b/2 = .12$). The calculations include one wake relaxation iteration. Superimposed on each plot is the geometry of the local cross section.

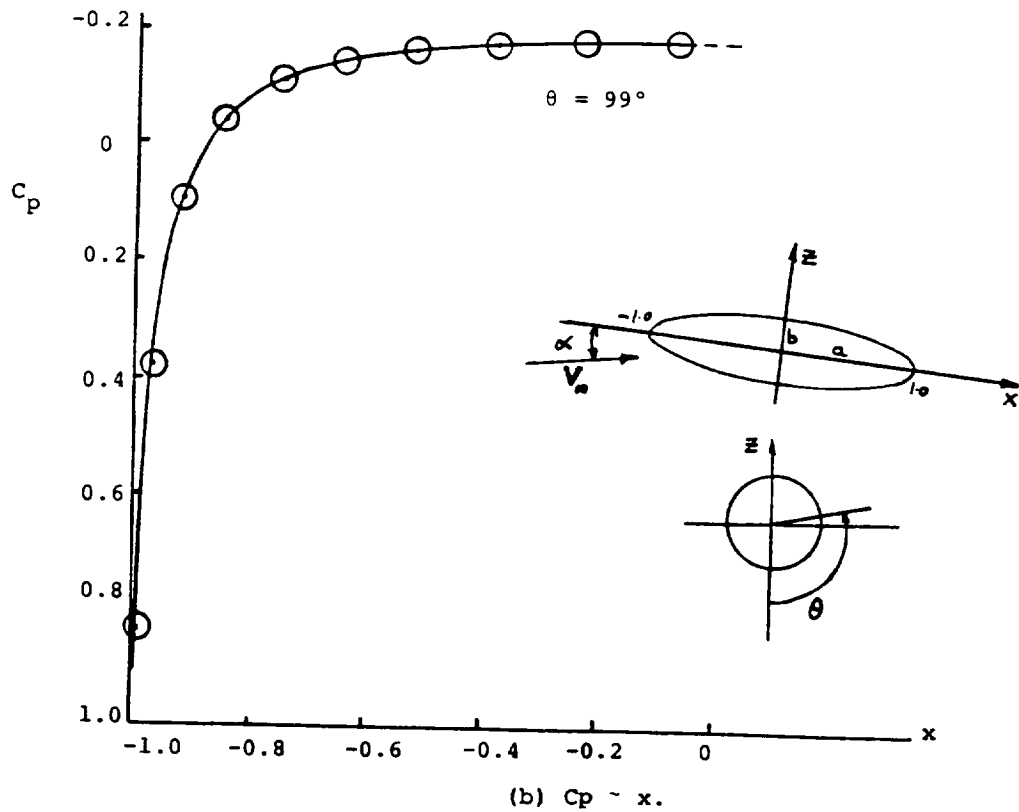
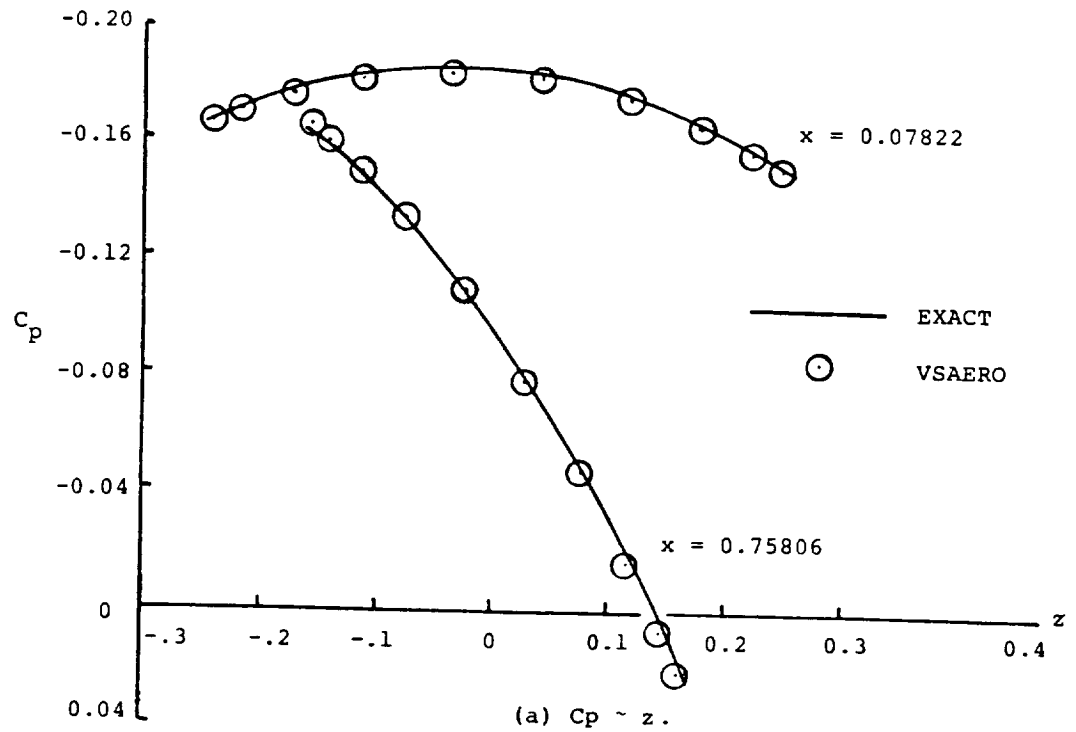
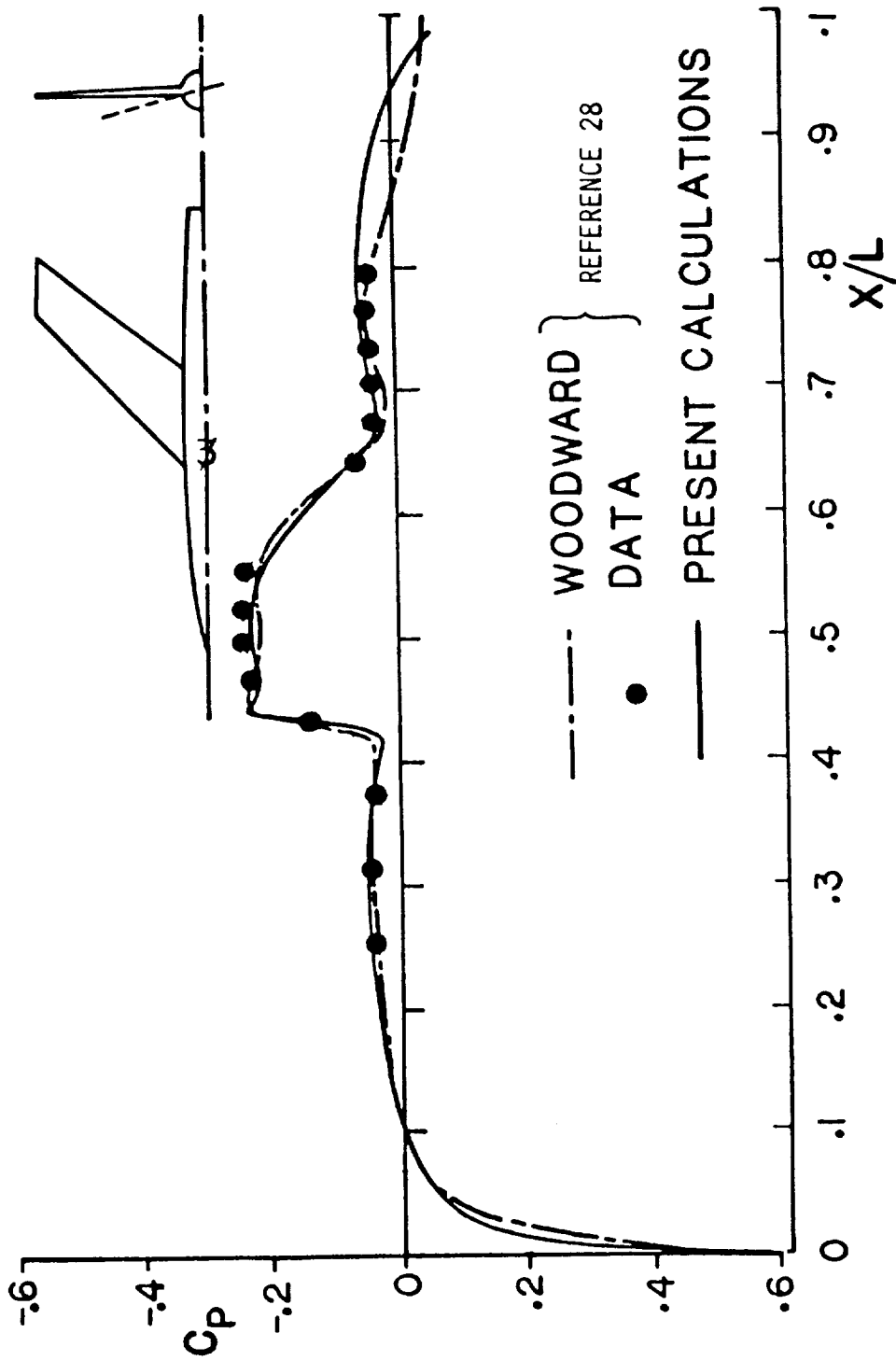
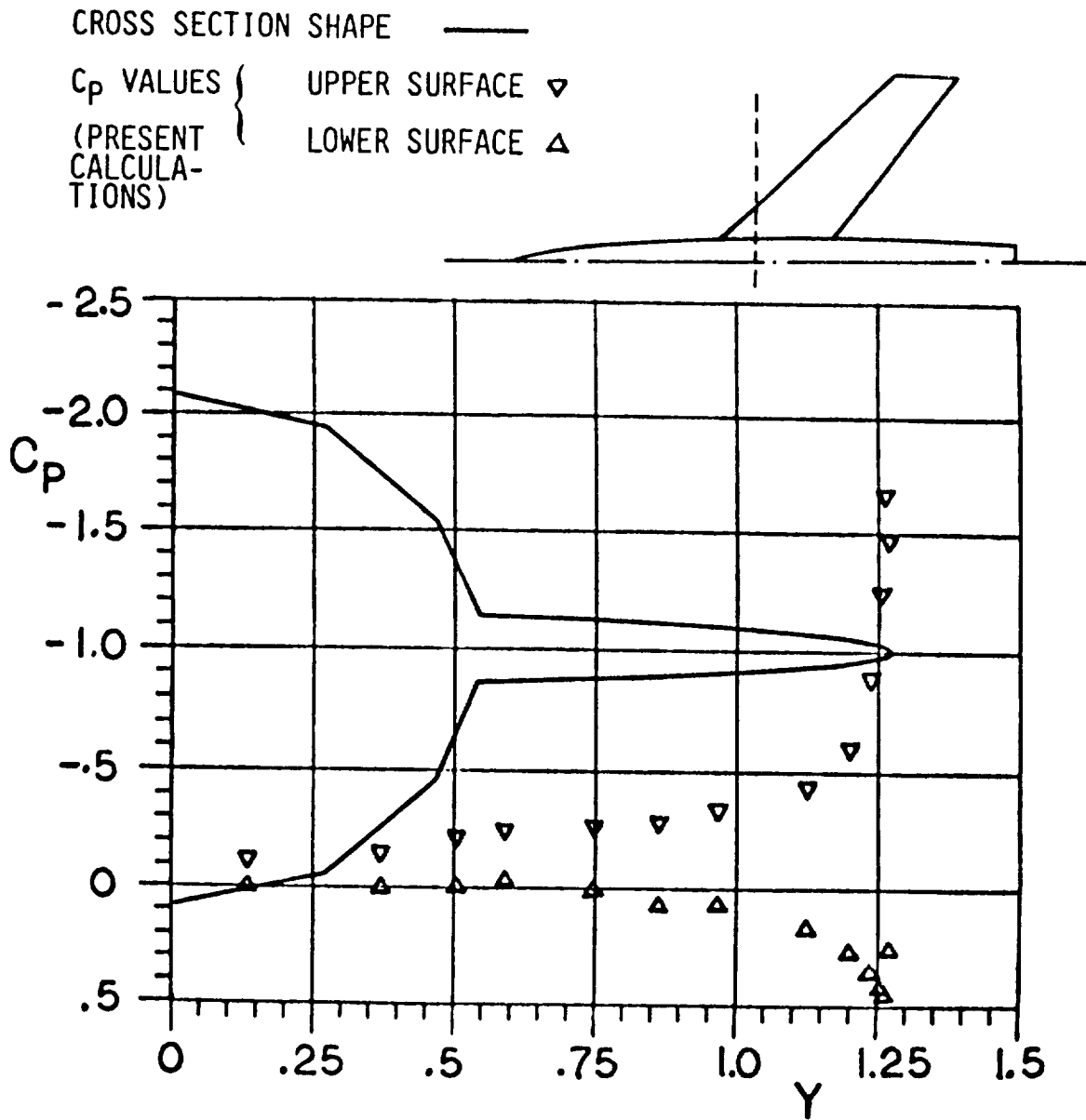


Figure 28. Comparison of Calculated and Exact Pressure Distributions on a 4:1 Spheroid at $\alpha = 5^\circ$.



(a) Above Wing-Body Junction Pressures

Figure 29. Pressure Distributions on a Wing-Body Configuration at $\alpha = 4^\circ$, $M_\infty = .6$.



(b) Spanwise Cut through Present Calculations at $X/L = .48$

Figure 29. Concluded.

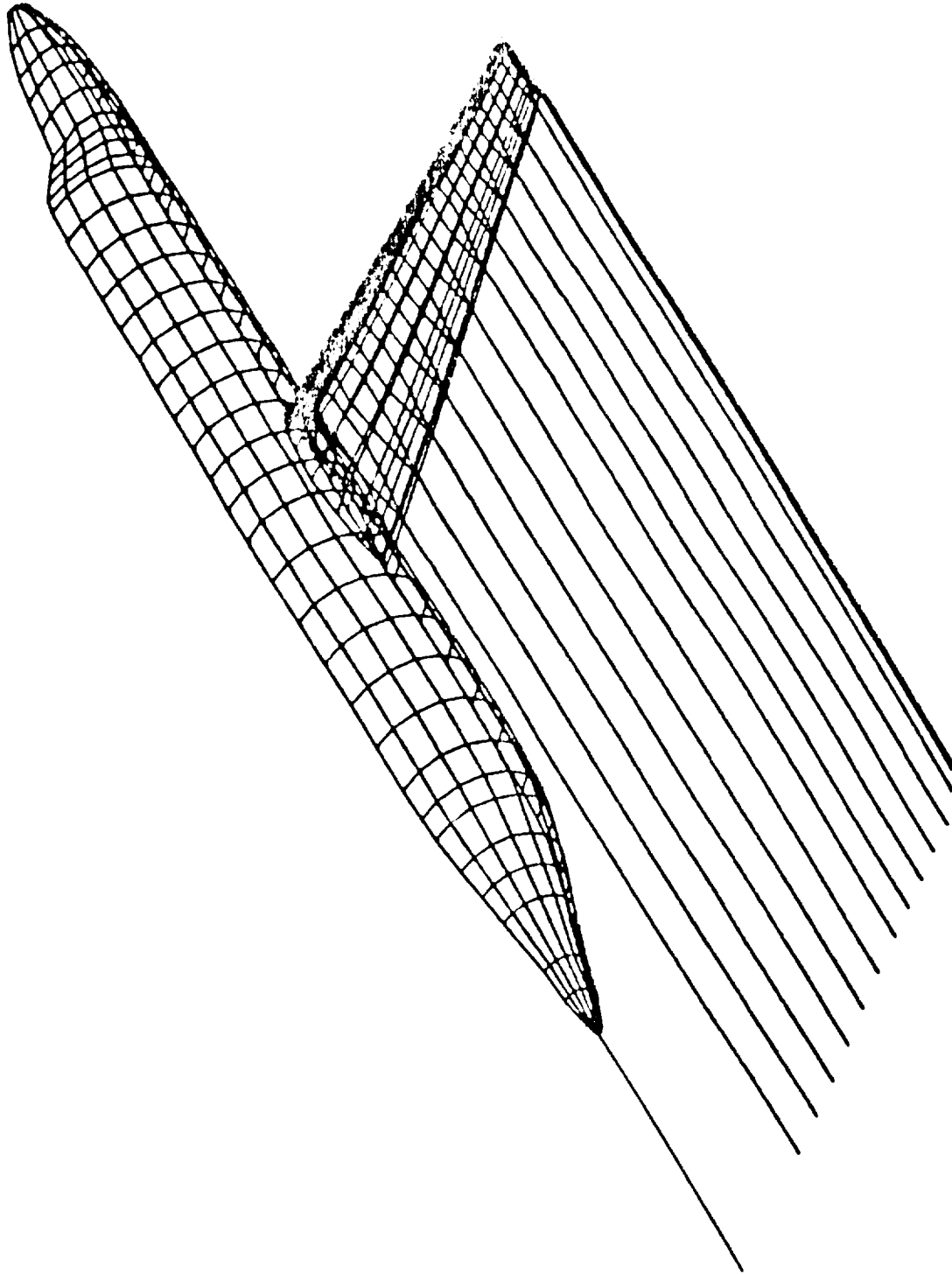
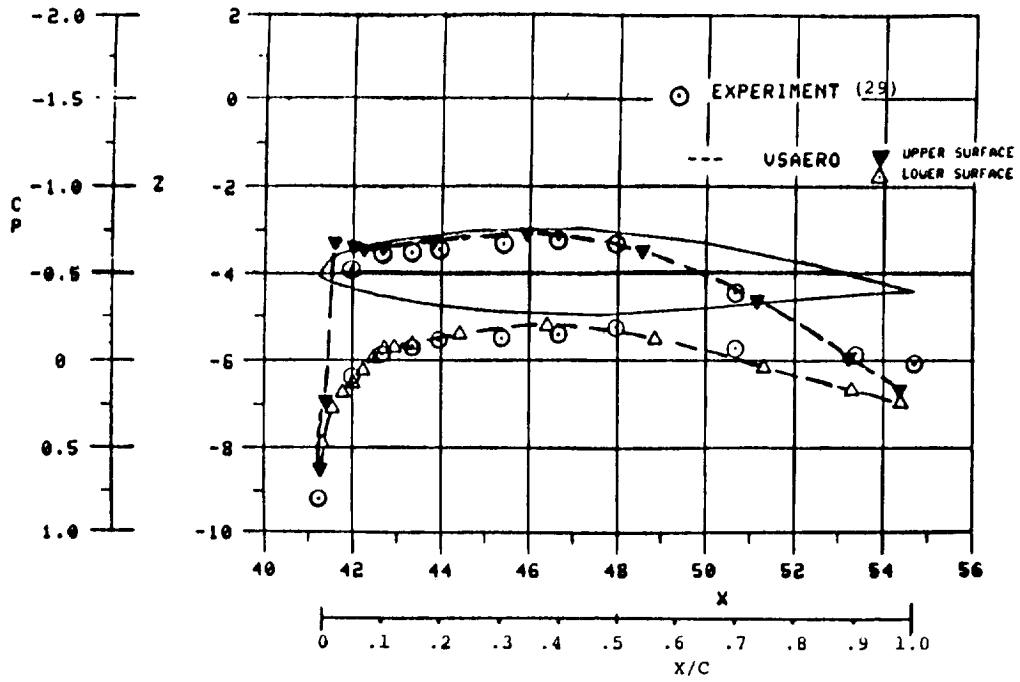
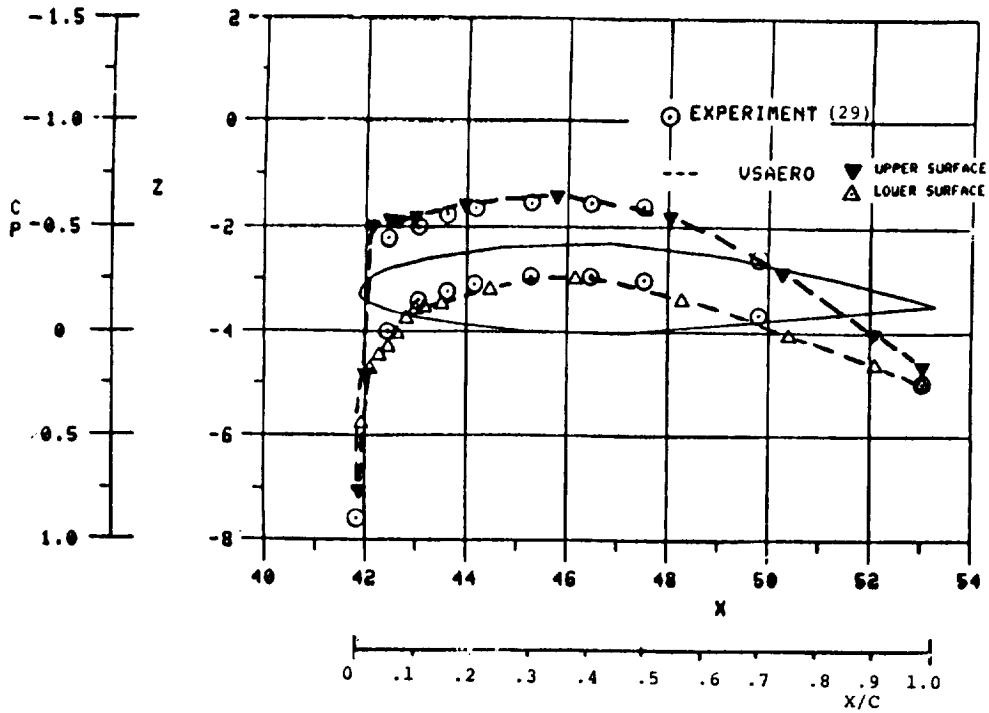


Figure 30. Swearingen Metro W.T. Model.

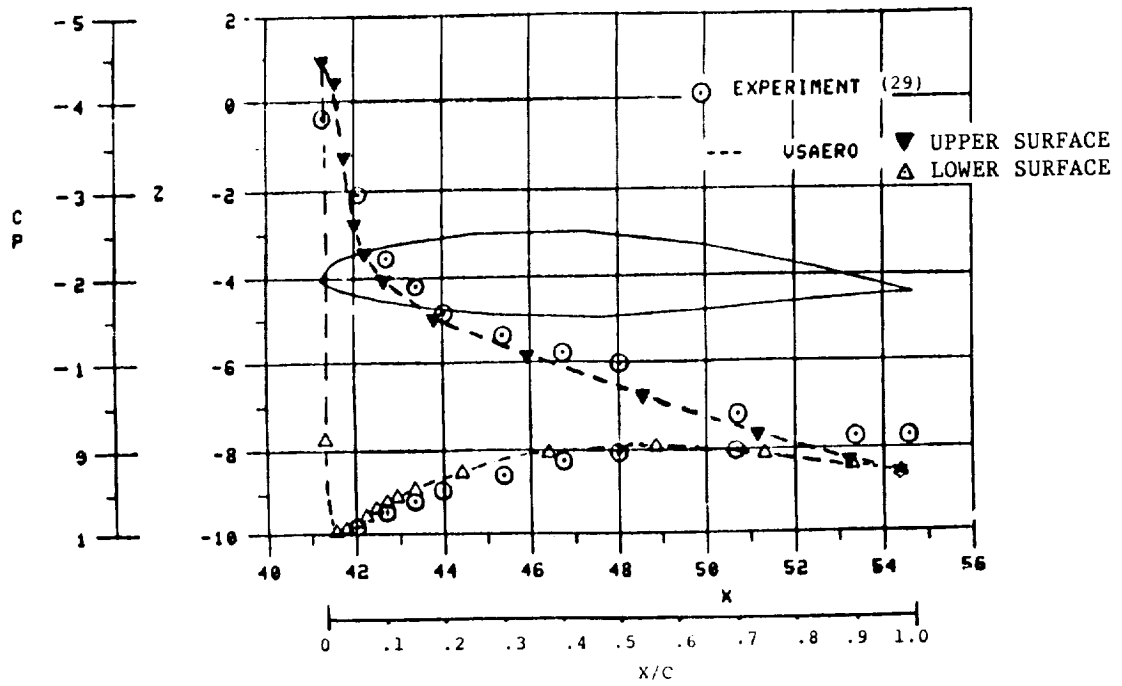


(a) Buttline Cut $Y = 9.0$.

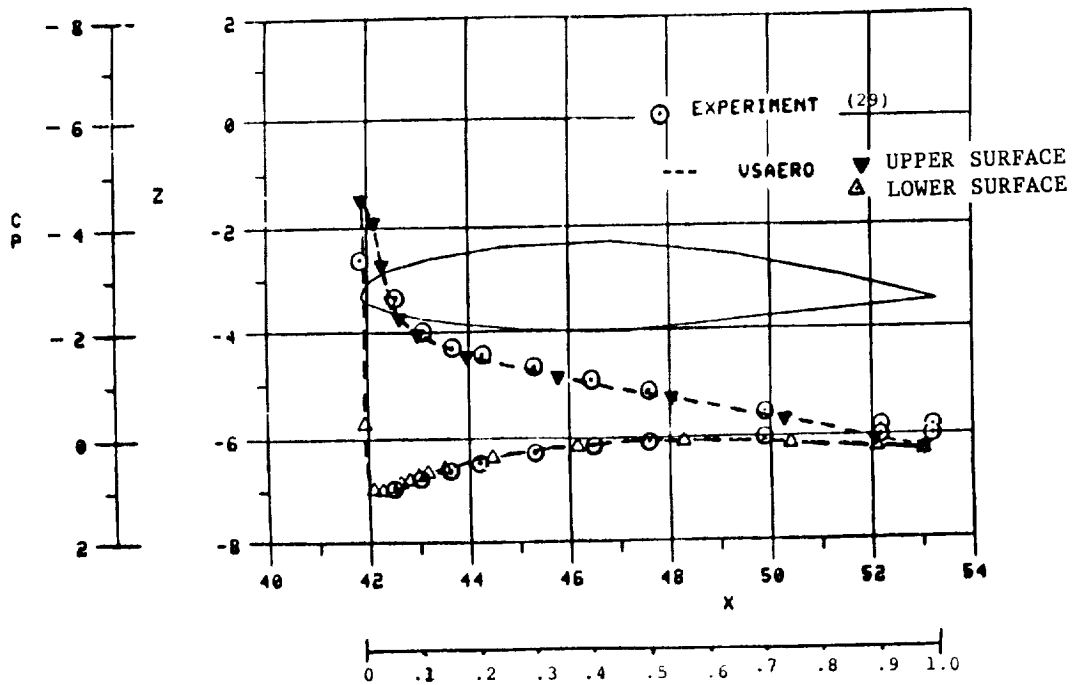


(b) Buttline Cut $Y = 18.0$.

Figure 31. Comparison of Calculated and Experimental Pressure Distributions on the Swearingen Metroliner Wind Tunnel Model at $\alpha = 0.0$, $M_\infty = 2.0$.

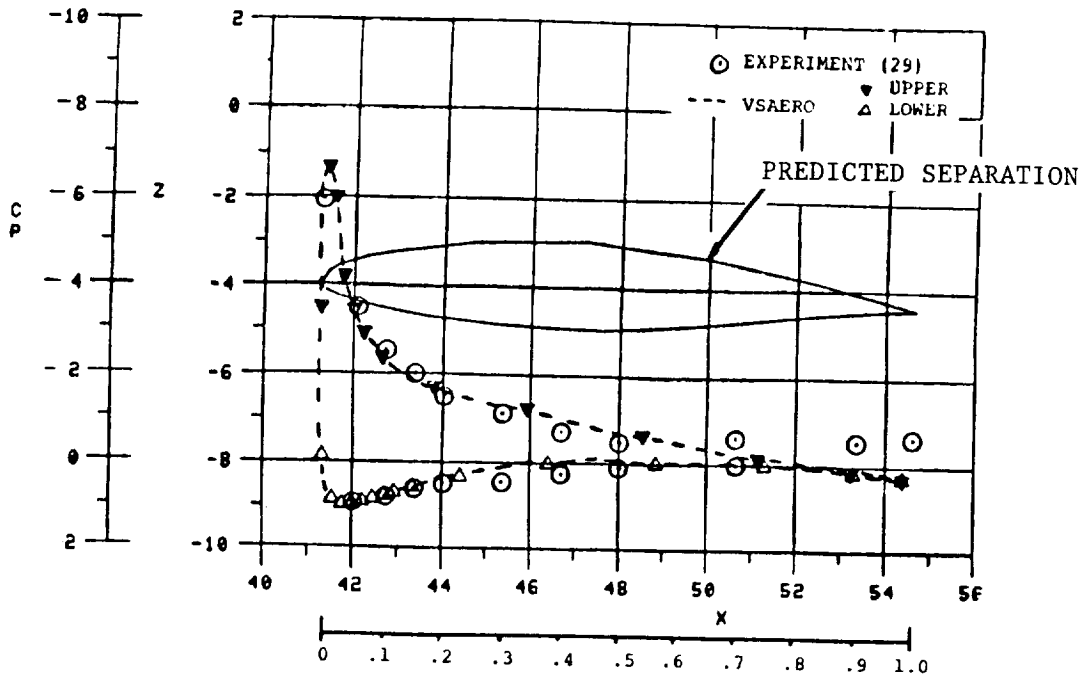


(a) Buttline Cut, $Y = 9.0$.

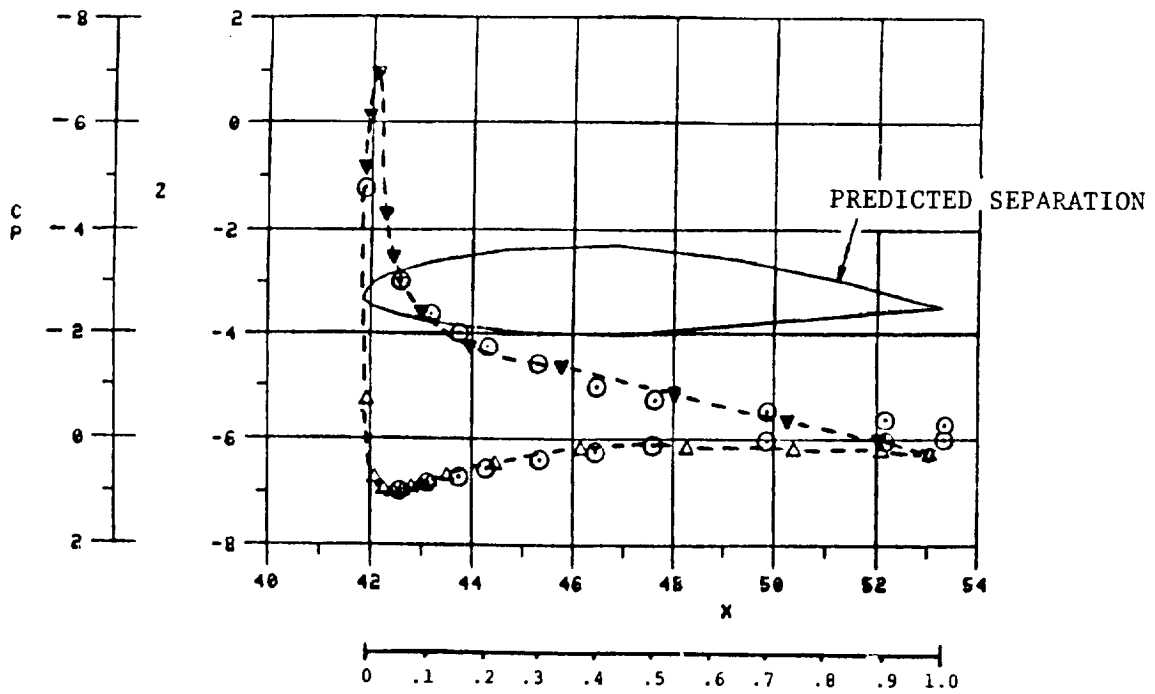


(b) Buttline Cut, $Y = 18.0$.

Figure 32. Comparison of Calculated and Experimental Pressure Distributions on the Swearingen Metroliner Wind Tunnel Model at $\alpha = 12^\circ$, $M_\infty = 2.0$.



(a) Buttline Cut, Y = 9.0.



(b) Buttline Cut, Y = 18.0.

Figure 33. Comparison of Calculated and Experimental Pressure Distributions on the Swearingen Metroliner Wind Tunnel Model at $\alpha = 16^\circ$, $M_\infty = 2.0$.

Figure 31 shows the comparisons at $\alpha = 0^\circ$. The experimental results at the inboard station indicate a small separation zone near the trailing edge and show slightly lower C_p values near the leading edge compared with the calculated data. The latter does not include a viscous/potential iteration for this case. The outboard station shows a much closer agreement between the results (Figure 31(b)).

Figure 32 shows the comparisons at $\alpha = 12^\circ$. The results are in remarkably good agreement except for the separated zone near the trailing edge, which has grown to approximately 20% of the chord.

Figure 33 shows the comparison at $\alpha = 16^\circ$. The calculations include one viscous potential iteration and the figure indicates the calculated location of separation which is in reasonable agreement with experimental data. Figure 34 shows the calculated surface streamlines and separation zone on the wing for this case.

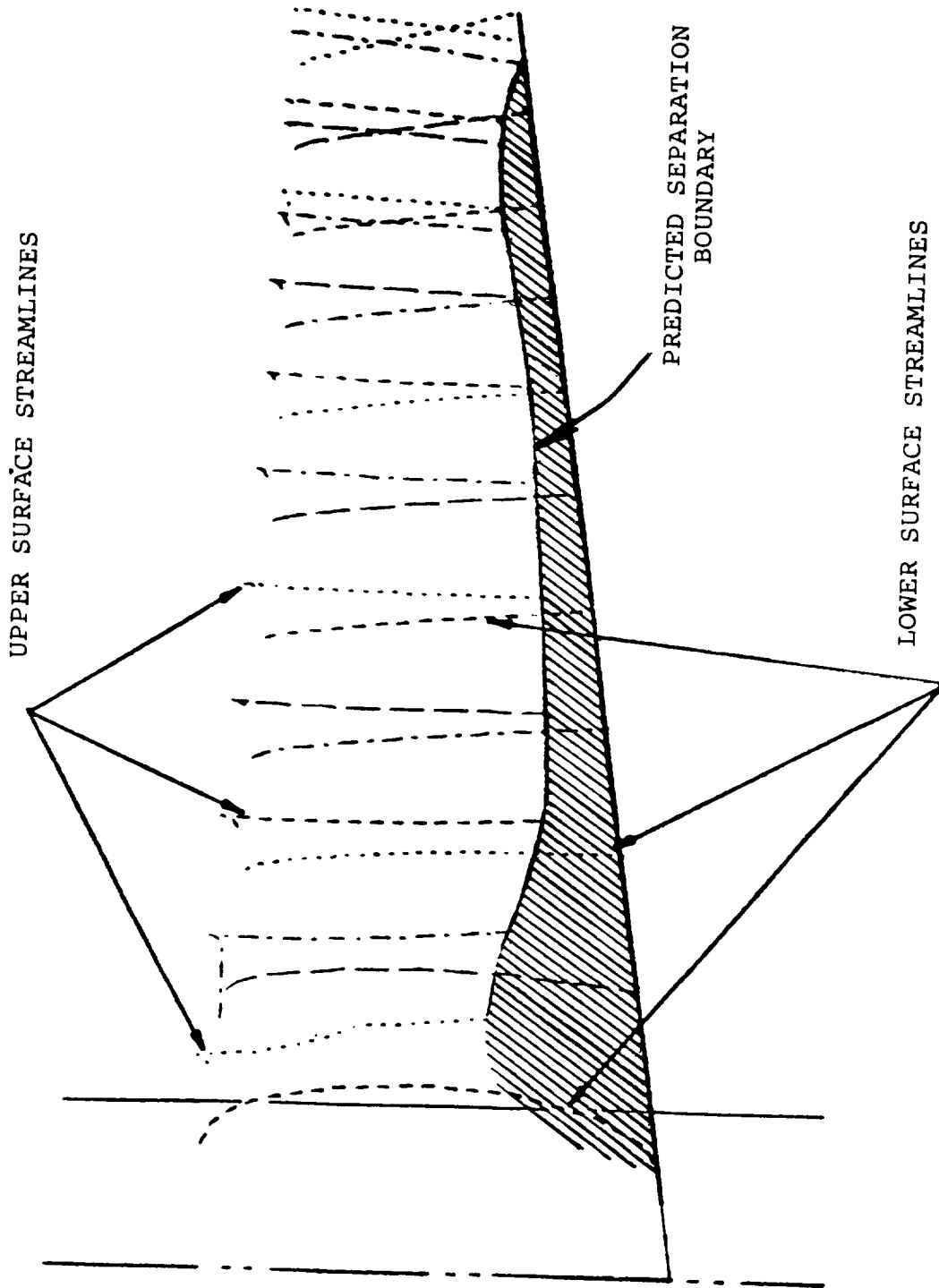


Figure 34. Calculated Streamlines and Separation Zone on the Swearingen Metroliner Wind Tunnel Model at $\alpha = 16^\circ$.

5.0 CONCLUSIONS

The formulation of the VSAERO program is described and a number of basic test cases examined. The panel method module of the program, based on simple quadrilateral panels with constant doublet and source, has produced results of comparable accuracy to those from higher-order methods given the same density of control points. The calculated results compare very well with exact, nominally exact and also experimental data cases. Problems associated with earlier low-order panel methods do not appear with the present formulation based on internal Dirichlet boundary conditions. Moreover, the low computing cost of the simple panel method makes it practical for applications to non-linear problems requiring iterative solutions, e.g., for wake-shape and surface boundary layer effects.

6.0 REFERENCES

1. Maskew, B., "Program VSAERO, A Computer Program for Calculating the Nonlinear Aerodynamic Characteristics of Arbitrary Configurations, User's Manual", NASA CR-166476, November 1982.
2. Dvorak, F.A., Woodward, F.A. and Maskew, B., "A Three-Dimensional Viscous/Potential Flow Interaction Analysis Method for Multi-Element Wings", NASA CR-152012, July 1977.
3. Maskew, B., "Calculation of the Three-Dimensional Potential Flow around Lifting Non-Planar Wings and Wing Bodies using a Surface Distribution of Quadrilateral Vortex Rings", Loughborough University of Technology, Dept. of Transport Tech. Report TT 7009, September 1970.
4. Maskew, B., "A Quadrilateral Vortex Method Applied to Configurations with High Circulation", Paper No. 10, Presented at the NASA Workshop on Vortex-Lattice Utilization, Langley Research Center, NASA SP-405, May 1976.
5. Maskew, B. and Woodward, F.A., "A Symmetrical Singularity Model for Lifting Potential Flow Analysis", AIAA J. Aircraft, September 1976.
6. Lamb, H.Y., Hydrodynamics, 6th Ed., Dover Publications, New York, Article No. 58, 1945.
7. Maskew, B., Rao, B.M. and Dvorak, F.A., "Prediction of Aerodynamic Characteristics for Wings with Extensive Separations", Paper No. 31 in 'Computation of Viscous-Inviscid Interactions', AGARD CP-291, February 1981.
8. Maskew, B., Vaidyanathan, T.S., Nathman, J.K. and Dvorak, F.A., "Prediction of Aerodynamic Characteristics of Fighter Wings at High Angles of Attack", Analytical Methods Report 8405a, Prepared for Office of Naval Research, Arlington, VA, under Contract N00014-82-C-0354, March 1984.
9. Maskew, B., "Influence of Rotor Blade Tip Shape on Tip Vortex Shedding--An Unsteady Inviscid Analysis", Proc. 36th Annual Forum of the AHS, Paper 80-6, May 1980.
10. Summa, J.M., "Advanced Rotor Analysis Methods for the Aerodynamics of Vortex/Blade Interactions in Hover", Paper No. 2.8, Presented at 8th European Rotorcraft and Powered Lift Aircraft Forum, Aix-en-Provence, France, August-September 1982.
11. Maskew, B. and Dvorak, F.A., "Prediction of Dynamic Stall Characteristics using Advanced Nonlinear Panel Methods", Analytical Methods Report 8406, Final Report, Prepared under

Contract F49620-82-C-0019 for AFOSR/NA, Bolling AFB, D.C., April 1984.

12. Maskew, B., "Calculation of Two-Dimensional Vortex/Surface Interference using Panel Methods", NASA CR-159334, November 1980.
13. Hess, J.L. and Smith, A.M.O., "Calculation of Non-Lifting Potential Flow about Arbitrary Three-Dimensional Bodies", Douglas Aircraft Company Report No. ES 40622, March 1962.
14. Martinsen, E., "The Calculation of the Pressure Distribution on a Cascade of Thick Airfoils by Means of Fredholm Integrand Equation of the Second Kind", NASA TT F-702, July 1971.
15. Maskew, B., "A Surface Vorticity Method for Calculating the Pressure Distribution over Aerofoils of Arbitrary Thickness and Camber in Two-Dimensional Potential Flow", Loughborough University of Technology Report TT 6907, 1969.
16. Maskew, B., "Prediction of Subsonic Aerodynamic Characteristics: A Case for Low-Order Panel Methods", J. Aircraft, Vol. 19, No. 2, February 1982, pp. 157-163.
17. Johnson, F.T. and Rubbert, P.E., "A General Panel Method for the Analysis and Design of Arbitrary Configurations in Subsonic Flows", NASA CR-3079, 1980.
18. Bristow, D.R. and Grose, G.G., "Modification of the Douglas-Neumann Program to Improve the Efficiency of Predicting Component Interference and High Lift Characteristics", NASA CR-3020, 1978.
19. Morino, L., Chen, L.-T. and Suci, E.O., "Steady and Oscillatory Subsonic Aerodynamics around Complex Configurations", AIAA J., Vol. 13, No. 3, March 1975.
20. Youngren, H.H., Bouchard, E.E., Coopersmith, R.M. and Miranda, L.R., "Comparison of Panel Method Formulations and its Influence on the Development of QUADPAN, an Advanced Low-Order Method", Paper AIAA-83-1827, Presented at the AIAA Applied Aerodynamics Conference, Danvers, Mass., July 1983.
21. Purcell, E.W., "The Vector Method of Solving Simultaneous Linear Equations", J. Math. Physics, Vol. 23, No. 180, 1953.
22. Bratkovich, A. and Marshall, F.J., "Iterative Techniques for the Solution of Large Linear Systems in Computational Aerodynamics", J. Aircraft, Vol. 12, No. 2, February 1975.
23. Dvorak, F.A., Maskew, B. and Woodward, F.A., "Investigation of Three-Dimensional Flow Separation on Fuselage Configurations", Analytical Methods, Inc.; USAAMRDL-TR-77-4, Eustis

Directorate, U.S. Army Air Mobility Research and Development Lab., Fort Eustis, VA, March 1977.

24. Vaidyanathan, T.S., "A Flow Field Analysis Procedure Based upon Velocity Potentials", Paper Presented at AIAA Applied Aerodynamics Conference, Danvers, Mass., July 1983.
25. Sytsma, H.S., Hewitt, B.L. and Rubbert, P.E., "A Comparison of Panel Methods for Subsonic Flow Computation", AGARD AG-241, 1979.
26. Williams, B.R., "An Exact Test Case for the Plane Potential Flow about Two Adjacent Lifting Aerofoils", R.A.E. Tech. Rep. 71197, 1971.
27. Weston, B., "Refinement of a Method for Determining the Induced and Profile Drag of a Finite Wing from Detailed Wake Measurements", Ph. D. Dissertation, Univ. of Florida, March 1981. Also, data to be published in a NASA TP.
28. Loving, D.L. and Estabrooks, B.B., "Transonic Wing Investigation in the Langley 8-Foot, High-Speed Tunnel at High Subsonic Mach Numbers and at a Mach Number of 1.2", NACA RM L51F07, September 1951.
29. Morgan, D.G., Galloway, T.L. and Gambucci, B.J., "Unpowered Aerodynamic Characteristics of a 15% Scale Model of a Twin-Engine Commuter Aircraft", NASA TM-81284, July 1981.

APPENDIX A

SUBROUTINE FLOW CHART

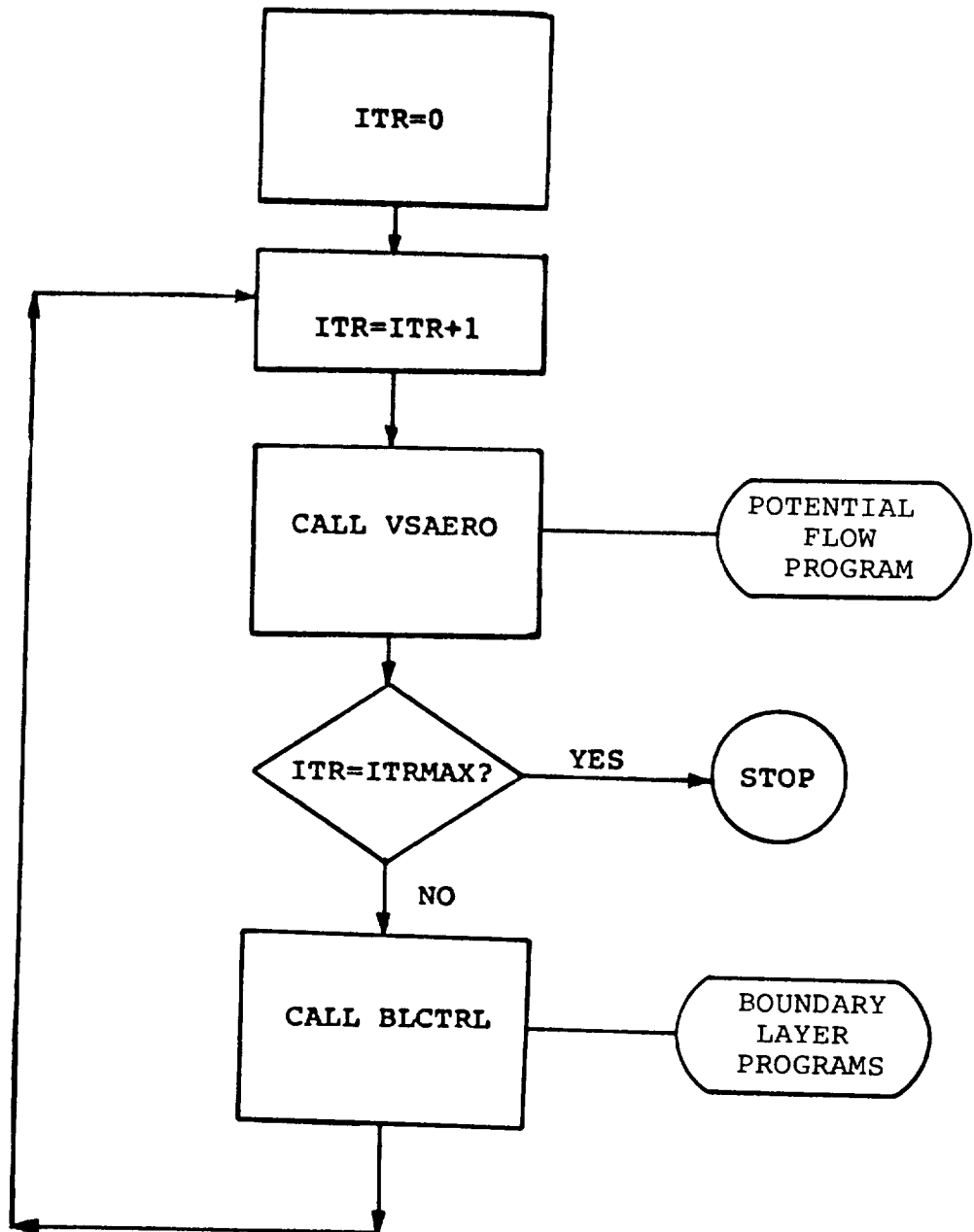


Figure A-1. Flow Chart of Main Program (Deck MVP);
The Viscous/Potential Iteration Loop.

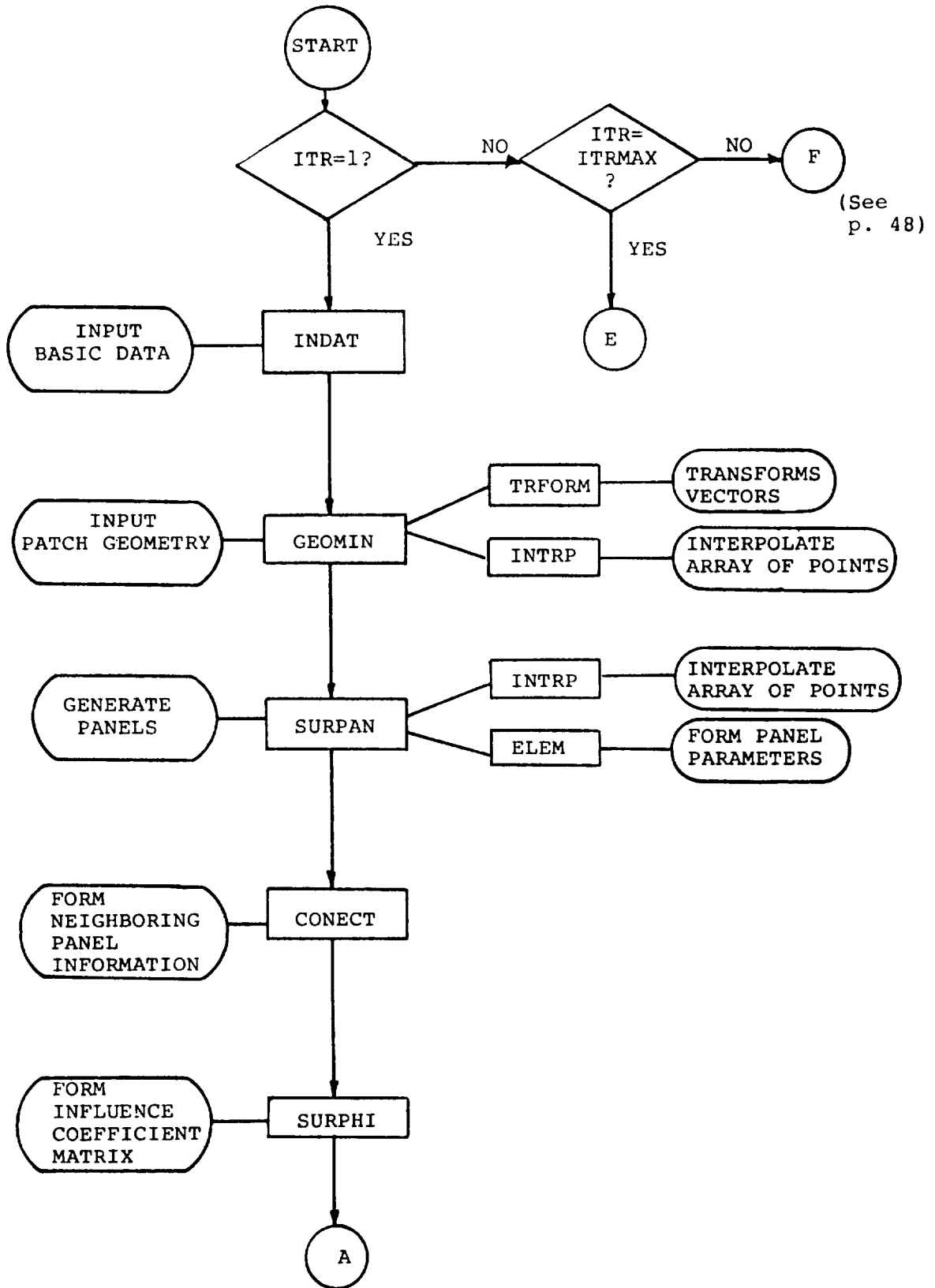


Figure A-2. Flow Chart of Subroutine VSAERO in Potential Flow.

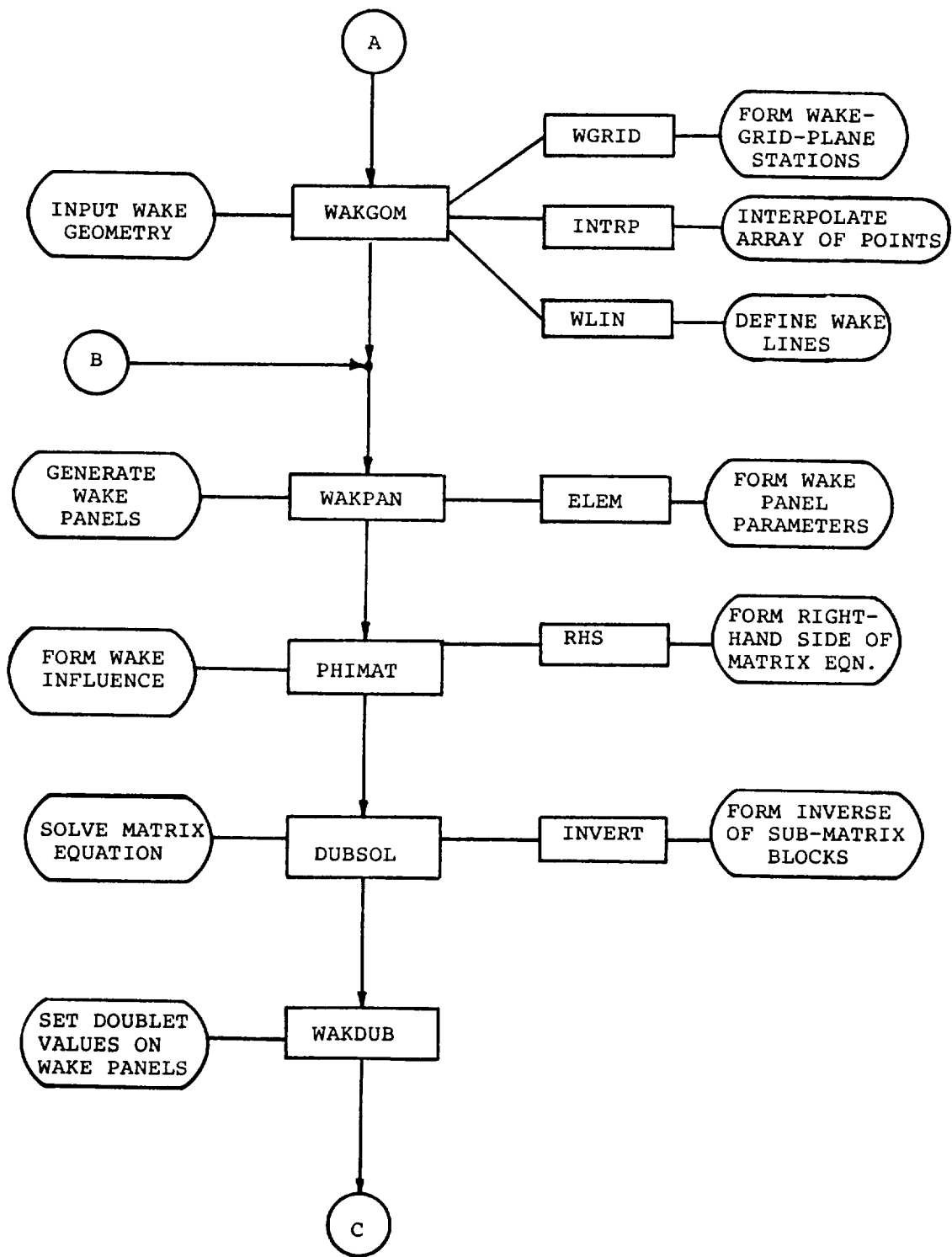


Figure A-2. Continued.

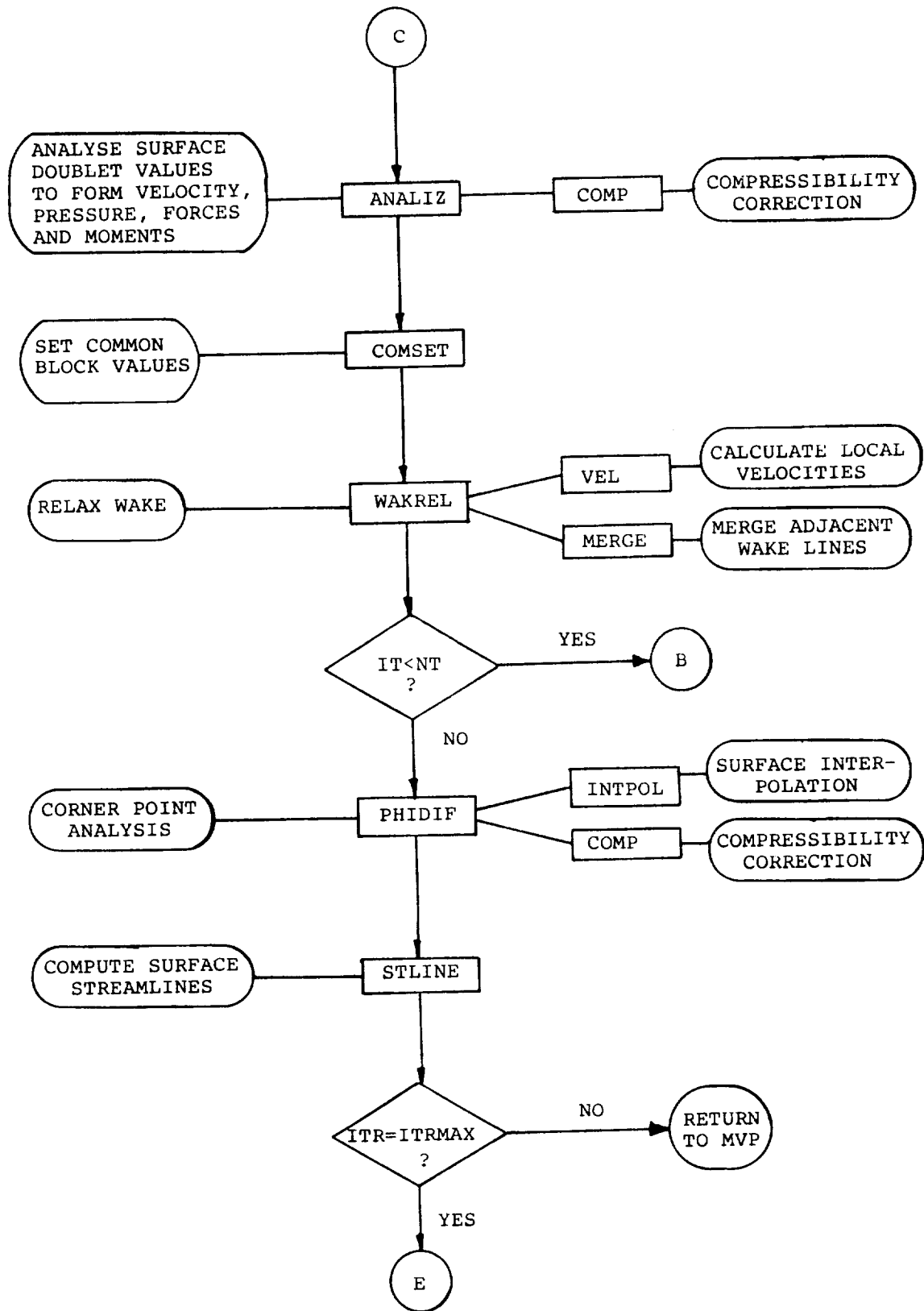


Figure A-2. Continued.

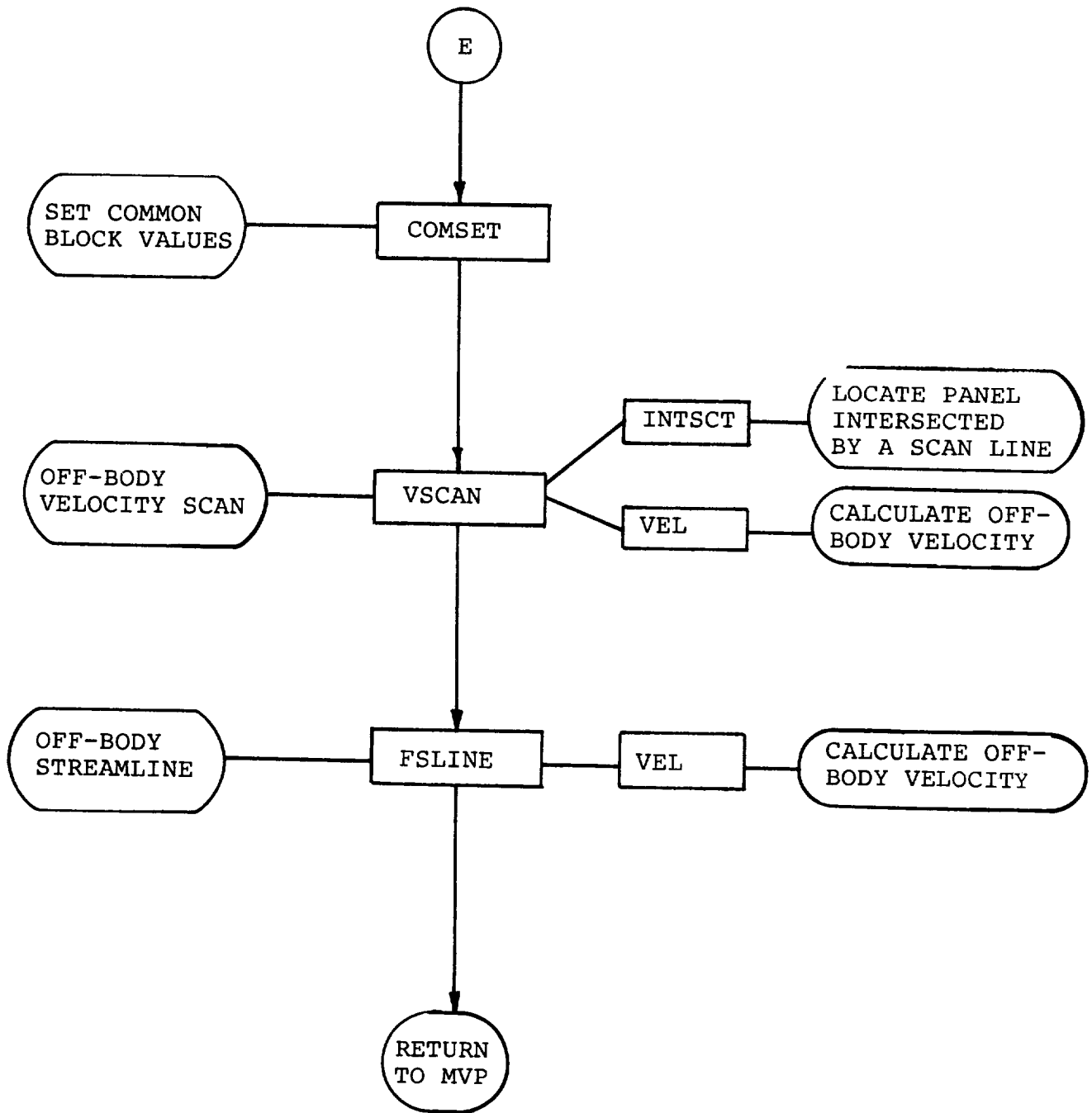


Figure A-2. Continued.

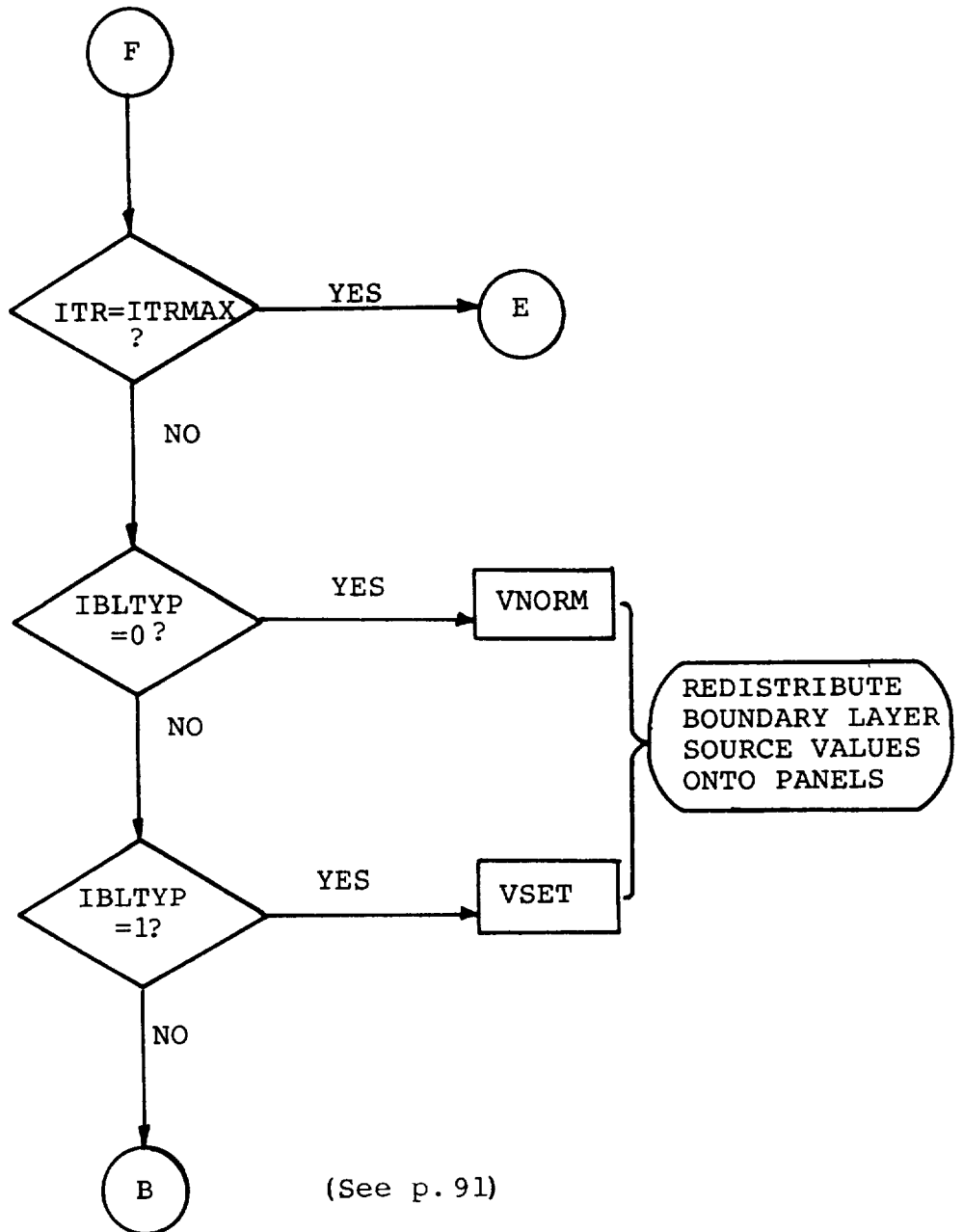


Figure A-2. Concluded.

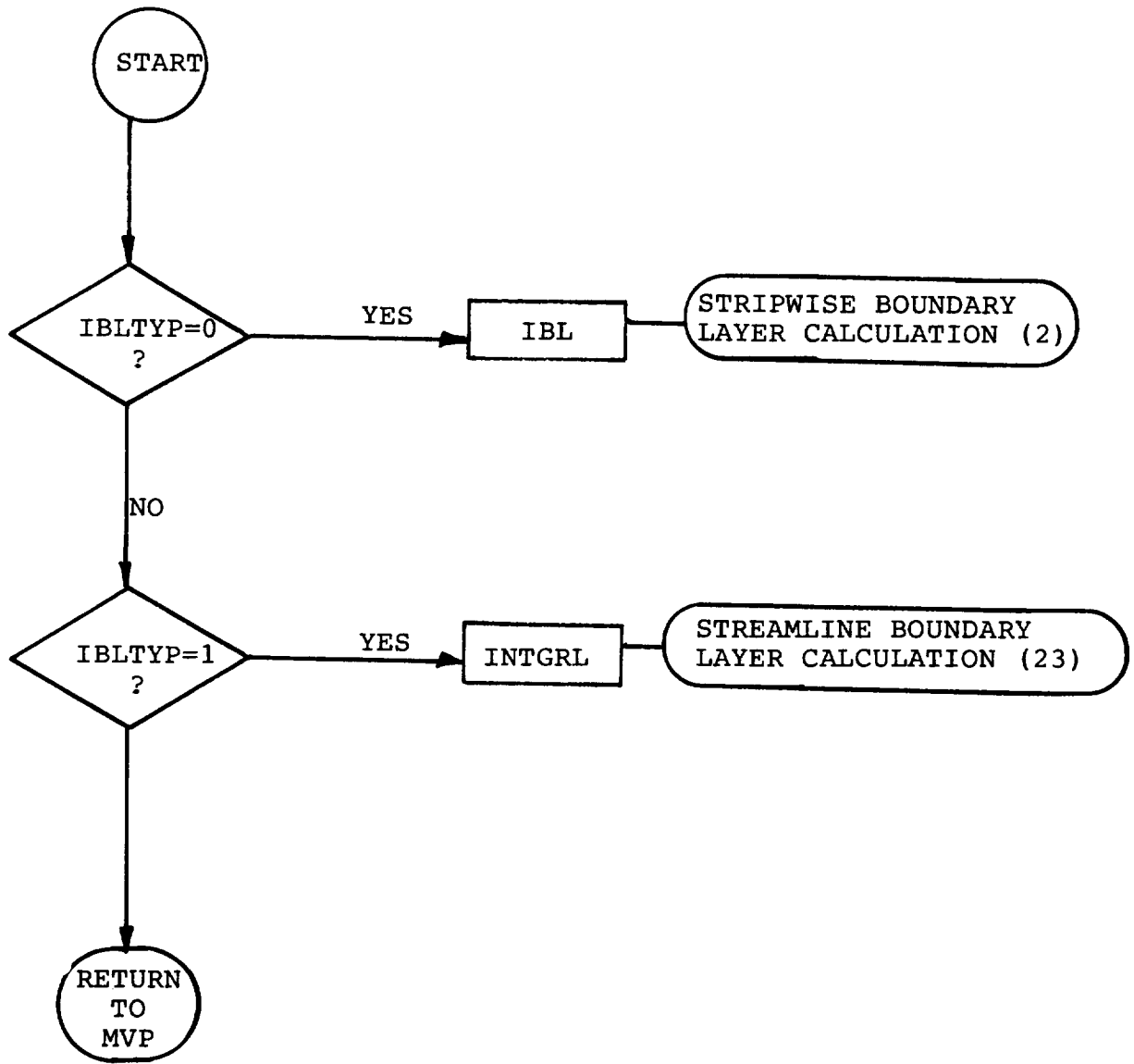


Figure A-3. Flow Chart for Major Subroutines in the Boundary Layer Analysis (Subroutine BLCTRL).

APPENDIX B

BIQUADRATIC INTERPOLATION

The biquadratic interpolation scheme described below is applied in a number of routines in the VSAERO code. Its simple multiplier form is very convenient to use and yet it is a "constrained" cubic; i.e., it cannot oscillate wildly. Experience with the routine over a number of years in the code has shown it to be a reliable method.

Given a set of position vectors, P_n , $n=1,2 \dots, N$, defining a smooth space curve, additional values are interpolated in, say, the interval between P_n and P_{n+1} , Figure B-1. The integrated contour length, s_n , to each point from the beginning of the curve, i.e., from P_1 , is generated first. For convenience the straight segment length is used across each interval; i.e., $s_n = |P_{n+1} - P_n|$, but arc lengths could easily be substituted.

Next, two quadratic curves, $q_1(\alpha, \alpha_{1_n})$ passing through points P_{n-1} , P_n , P_{n+1} , and $q_2(\alpha, \alpha_{2_n})$ passing through points P_n , P_{n+1} , and P_{n+2} , are formed, Figure B-1.

The normalized interpolation parameter, α , ranges from 0 to 1 in the n^{th} interval, and has value

$$\alpha_{1_n} \text{ at } P_{n-1} \quad \text{and} \quad \alpha_{2_n} \text{ at } P_{n+2},$$

where

$$\alpha_{1_n} = (s_{n-1} - s_n) / (s_{n+1} - s_n); \text{ and}$$

$$\alpha_{2_n} = (s_{n+2} - s_n) / (s_{n+1} - s_n).$$

In the n^{th} interval, a linear combination of q_1 and q_2 defines the biquadratic interpolation curve.

$$P(\alpha) = \alpha q_2(\alpha, \alpha_{2_n}) + (1 - \alpha) q_1(\alpha, \alpha_{1_n})$$

The biquadratic is, therefore, a cubic, but it is constrained to lie between the two quadratic curves. Clearly, the value of α for a point distance, s , from the start of the curve (but located in the n^{th} interval) is

$$\alpha = s / (s_{n+1} - s_n)$$

The form of the interpolation curve can be expressed in terms of biquadratic multipliers, G1, G2, applied to the four local position vectors:

$$\begin{aligned} P(\alpha) = & P_{n-1} G1(\alpha, \alpha_{1_n}) + P_n G2(\alpha, \alpha_{1_n}, \alpha_{2_n}) \\ & + P_{n+1} G2(1 - \alpha, 1 - \alpha_{2_n}, 1 - \alpha_{1_n}) \\ & + P_{n+2} G1(1 - \alpha, 1 - \alpha_{2_n}). \end{aligned}$$

The forms of G1, G2 are:

$$\begin{aligned} G1(a,b) &= a(1 - a)^2 / \{b(1 - b)\} \\ G2(a,b,c) &= (1 - a)\{1 - a(1 - a)/b - a^2/c\} \end{aligned}$$

These multipliers, based on the linear combination of two quadratics, give continuous slope and a piecewise linear--but not necessarily continuous--variation of second derivative across each interval.

The G multipliers can be differentiated to give the tangent vector:

$$\begin{aligned} t(\alpha) = & P_{n-1} H1(\alpha, \alpha_{1_n}) + P_n H2(\alpha, \alpha_{1_n}, \alpha_{2_n}) \\ & - P_{n+1} H2(1 - \alpha, 1 - \alpha_{2_n}, 1 - \alpha_{1_n}) \\ & - P_{n+2} H1(1 - \alpha, 1 - \alpha_{2_n}) \end{aligned}$$

where the tangent multipliers are:

$$\begin{aligned} H1(a,b) &= (1 - 4a + 3a^2) / \{b(1 - b)\} \\ H2(a,b,c) &= (4a - 3a^2 - 1)/b + (3a^2 - 2a)/c - 1 \end{aligned}$$

Note: this is not a unit vector: $|t(\alpha)| = \frac{ds}{d\alpha}$.

The G multipliers can also be integrated to give the area under the curve between the n^{th} and the $(n+1)^{\text{th}}$ points:

$$A_n = P_{n-1} F1(\alpha_{1_n}) + P_n F2(\alpha_{1_n}, \alpha_{2_n}) \\ + P_{n+1} F2(1 - \alpha_{2_n}, 1 - \alpha_{2_n}) + P_{n+2} F1(1 - \alpha_{2_n}) \frac{ds}{d\alpha}$$

where the integral multipliers are:

$$F1(b) = 1/\{12b(1 - b)\}$$

$$F2(b,c) = \{1 - (1/b + 1/c)/6\}/2$$

This assumes that the value of $\frac{ds}{d\alpha}$ is constant over the interval.

In this case, therefore, it would be an advantage to use the arc length intervals rather than straight line intervals when calculating surface distances.

The F multipliers are for possible future use in the integration of surface pressures to obtain forces and moments.

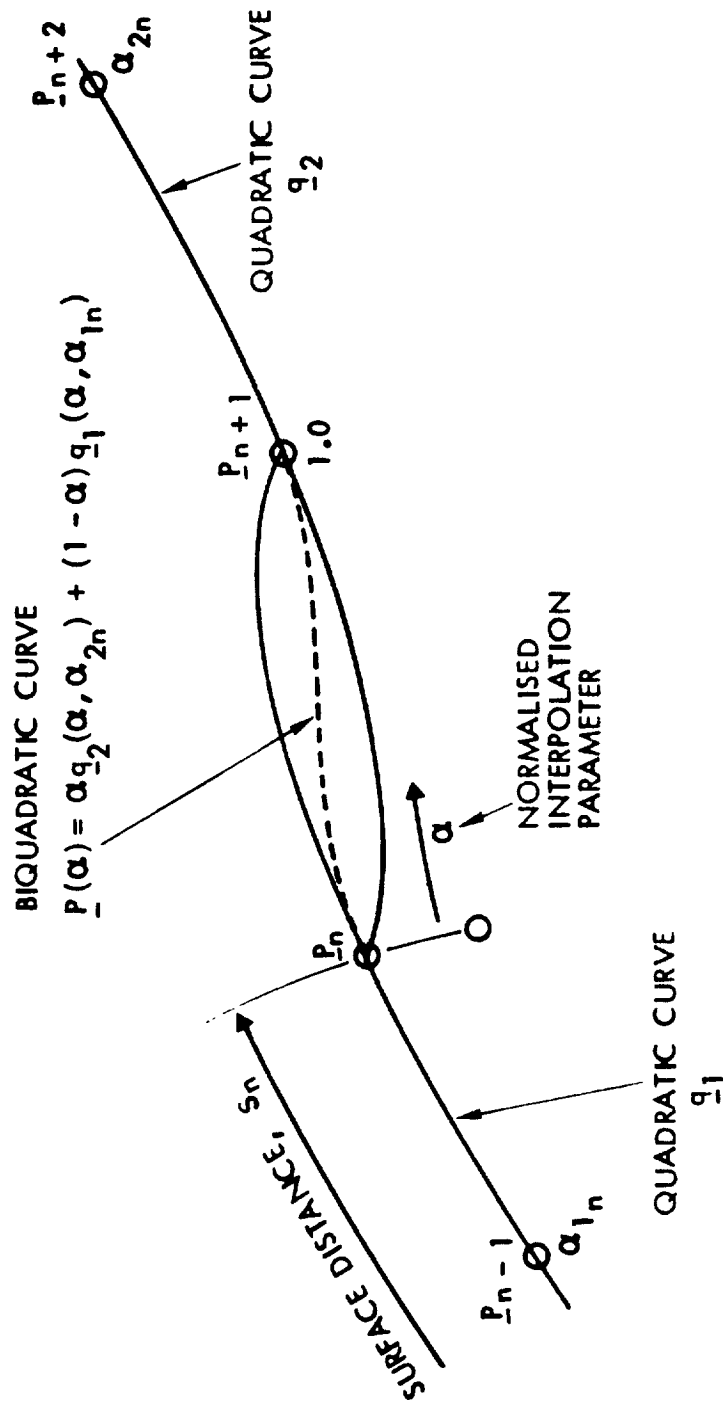


Figure B-2. Biquadratic Interpolation.



1. Report No. NASA CR-4023		2. Government Accession No.		3. Recipient's Catalog No.	
4. Title and Subtitle PROGRAM VSAERO THEORY DOCUMENT A Computer Program for Calculating Nonlinear Aerodynamic Characteristics of Arbitrary Configurations				5. Report Date September 1987	
				6. Performing Organization Code	
7. Author(s) Brian Maskew				8. Performing Organization Report No. AMI Report 8416	
9. Performing Organization Name and Address ANALYTICAL METHODS, INC. 2133 - 152nd Avenue N.E. Redmond, Washington 98052				10. Work Unit No.	
				11. Contract or Grant No. NAS2-11945	
12. Sponsoring Agency Name and Address NASA Ames Research Center Moffett Field, California 94035				13. Type of Report and Period Covered Final Report July 1984 - May 1987	
				14. Sponsoring Agency Code	
15. Supplementary Notes Point of Contact: Brian Smith (415) 694-5039 M.S. 247-1 FTS 464-5039 NASA Ames Research Center Moffett Field, CA 94035					
16. Abstract The VSAERO low-order panel method formulation is described for the calculation of subsonic aerodynamic characteristics of general configurations. The method is based on piecewise constant doublet and source singularities. Two forms of the internal Dirichlet boundary condition are discussed and the source distribution is determined by the external Neumann boundary condition. A number of basic test cases are examined. Calculations are compared with higher-order solutions for a number of cases. It is demonstrated that for comparable density of control points where the boundary conditions are satisfied, the low-order method gives comparable accuracy to the higher-order solutions. It is also shown that problems associated with some earlier low-order panel methods, e.g., leakage in internal flows and junctions and also poor trailing-edge solutions, do not appear for the present method. Further, the application of the Kutta conditions is extremely simple; no extra equation or trailing-edge velocity point is required. The method has very low computing costs and this has made it practical for application to nonlinear problems requiring iterative solutions for wake shape and surface boundary layer effects.					
17. Key Words (Suggested by Author(s)) Subsonic Panel Method; Arbitrary Configuration; Viscous Flow/Potential Flow Coupling; Relaxed Wake Iteration			18. Distribution Statement Subject Category 02		
19. Security Classif. (of this report) Unclassified		20. Security Classif. (of this page) Unclassified		21. No. of pages 100	22. Price